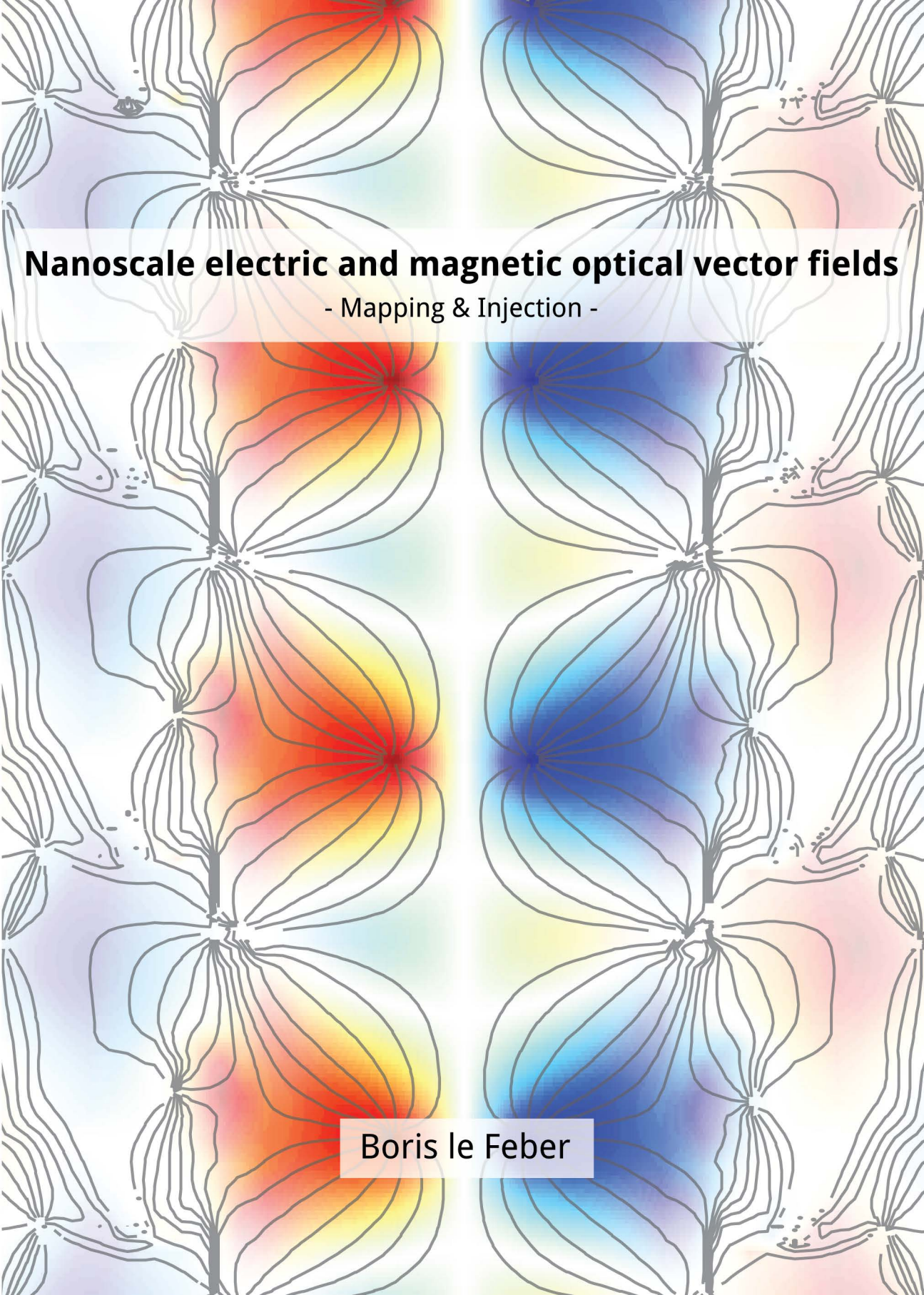

Nanoscale electric and magnetic optical vector fields

- Mapping & Injection -

Boris le Feber

Nanoscale electric and magnetic optical vector fields

- mapping & injection -

Samenstelling van de promotiecommissie:

prof. dr. L. Kuipers (promotor)	Universiteit Twente
prof. dr. N. F. van Hulst	Institut de Ciències Fotòniques, España
prof. dr. A. Fiore	Technische Universiteit Eindhoven
prof. dr. J. L. Herek	Universiteit Twente
prof. dr. S. G. Lemay	Universiteit Twente
prof. dr. V. Subramaniam	Universiteit Twente

This research is part of the research program of the
"Stichting Fundamenteel Onderzoek der Materie" (FOM),
which is financially supported by the
"Nederlandse Organisatie voor Wetenschappelijk Onderzoek" (NWO).

This work was carried out at:
NanoOptics Group,
FOM-Institute for Atomic and Molecular Physics (AMOLF)
Science Park 104, 1098 XG Amsterdam, The Netherlands,
where a limited number of copies of this thesis is available.

Cover: Color maps of the experimentally obtained ellipticity of the polarization ellipse of the in-plane magnetic (front cover) and electric fields (back cover) 20 nm above a photonic crystal waveguide. The maps are shown on a white background and their transparency is defined by the directional emission efficiency of the waveguide. The ellipticity maps are overlayed with gray lines along which the angle of the polarization ellipse is constant.

ISBN: 978-94-6259-491-3

Nanoscale electric and magnetic optical vector fields

- mapping & injection -

PROEFSCHRIFT

ter verkrijging van
de graad van doctor aan de Universiteit Twente,
op gezag van de rector magnificus,
prof. dr. H. Brinksma,
volgens besluit van het College voor Promoties
in het openbaar te verdedigen
op vrijdag 30 januari 2015 om 14:45 uur

door

Boris le Feber

geboren op 16 augustus 1987
te Amsterdam, Nederland

Dit proefschrift is goedgekeurd door:
prof. dr. L. (Kobus) Kuipers

Contents

List of acronyms

AOM	Acousto-optic modulator
BB	Bethe-Bouwkamp
C-point	Polarization singularity
EM	Electromagnetic
FEM	Finite element method
L-line	Line of linear polarization
LC	Liquid crystal
LCP	Left-handed circularly polarized
LDOS	Local density of states
LED	Light-emitting diode
LI	Lock-in amplifier
MCD	Magnetic circular dichroism
NSOM	Near-field scanning optical microscope
OAM	Orbital angular momentum
PEC	Perfect electrical conductor
PhCW	Photonic crystal waveguide
PMMA	Polymethylmethacrylate
QD	Quantum dot
RCP	Right-handed circularly polarized
SAM	Spin angular momentum
SEM	Scanning electron microscope
SI	International system of units
SPP	Surface plasmon polariton
SRP	Split-ring probe
TE	Transverse electric
TIR	Total internal reflection

1

Introduction

The control over light drives a broad range of recent technological advances that improve our daily lives. For example, guided light in optical fibers enables the transportation of large amounts of data across the globe [1], the energy of light harvested in solar panels accounts for an increasingly large fraction of the global energy consumption [2] and efficient solid-state light sources are becoming increasingly common [3].

Over the last two decades nanophotonic structures have been developed that advance or promise to advance nearly all light-dependent technologies. For example, the placement of nanoparticles in solar cells allows a more efficient capturing of light [4], nanophotonic waveguiding circuitry promises to deliver fast (quantum) information processing [5, 6] and nanophotonic sensors can enhance the sensitivity to molecules by orders of magnitude [7].

The power of these nanophotonic devices lies in the unparalleled control over light that they enable. In turn, the extent to which their potential can be harnessed vitally depends on the understanding of the interactions between light and matter at the nanoscale. Importantly, these interactions can be inferred from the optical fields near nanophotonic structures.

This chapter starts with an introduction of the equations that describe the optical fields of light. We illustrate this behavior using some recent cal-

culations of the optical fields near nanophotonic structures and we highlight some important features of these fields. Next, we focus our attention on the optical properties of, and optical fields near, nanophotonic structures that can guide light. Subsequently, we discuss the control over nearby emitters offered by nanophotonic structures. Lastly, we conclude this chapter with an outline of this thesis.

1.1 Optical fields in homogeneous media

One of the fascinating aspects of light is that it manifests itself both as waves and as particles. The wave picture mostly allows for an accurate description of the flow of light near nanophotonic structures [8]. Therefore, in this thesis we adopt the wave picture. In this picture, light consists of oscillating electric and magnetic fields. Mathematically, these electromagnetic fields and their interaction with matter is described by Maxwell's equations [9]. In a macroscopic treatment and in absence of sources and currents, Maxwell's equations are

$$\nabla \times \mathbf{E}(\mathbf{r},t) = -\mu_0\mu_r(\mathbf{r})\frac{\partial \mathbf{H}(\mathbf{r},t)}{\partial t}, \tag{1.1a}$$

$$\nabla \times \mathbf{H}(\mathbf{r},t) = \epsilon_0\epsilon_r(\mathbf{r})\frac{\partial \mathbf{E}(\mathbf{r},t)}{\partial t}, \tag{1.1b}$$

$$\nabla \cdot (\epsilon_0\epsilon_r(\mathbf{r})\mathbf{E}(\mathbf{r},t)) = 0, \tag{1.1c}$$

$$\nabla \cdot \left(\frac{1}{\mu_0\mu_r(\mathbf{r})}\mathbf{H}(\mathbf{r},t)\right) = 0, \tag{1.1d}$$

where $\mathbf{r} = (x, y, z)$ is the position in a three dimensional space, $\epsilon_0(\mu_0)$ and $\epsilon_r(\mathbf{r})$ ($\mu_r(\mathbf{r})$) are the vacuum and relative electric permittivity (magnetic permeability), respectively, and $\mathbf{E}(\mathbf{r},t)$ and $\mathbf{H}(\mathbf{r},t)$ are complex vectors that represent the electric and magnetic optical field respectively. In the expression for the material properties $\epsilon_r(\mathbf{r})$ and $\mu_r(\mathbf{r})$ we have omitted any time dependence. That is, in this thesis we consider only the linear response of materials and ignore other (for example thermal [10, 11]) effects that could change the permittivity. Because of these simplifications time harmonic solutions to Maxwell's equations exist.

1.1.1 The diffraction limit and evanescent optical fields

The time-harmonic solutions to Maxwell's equations of the electric field can be expressed as a superposition of complex waves [8]

$$\mathbf{E}(\mathbf{r},t) = \int \mathbf{a}_{\mathbf{k}} e^{i(\mathbf{k}\cdot\mathbf{r}-\omega t)} d\mathbf{k}, \tag{1.2}$$

where the integral is over all $\mathbf{k}$, ω is the angular frequency of the light, $\mathbf{k}$ the wavevector and $\mathbf{a}_{\mathbf{k}}$ denotes the complex amplitude and field orientation associated with each $\mathbf{k}$. Throughout space $\mathbf{k} = (k_x, k_y, k_z)$ satisfies

$$n^2 k_0^2 = k_x^2 + k_y^2 + k_z^2, \tag{1.3}$$

where $n = n(\mathbf{r}) = \sqrt{\epsilon_r(\mathbf{r})\mu_r(\mathbf{r})}$ is the local refractive index, $k_0 = 2\pi/\lambda_0$ is the wavevector in free space and $\lambda_0 = 2\pi c/\omega$ the free-space wavelength, where c is the speed of light. In a purely dielectric medium with no losses, the refractive index is a real and positive quantity. In such a medium, optical waves can, according to their wavevector, be classified as plane and evanescent waves [8]. A wave can be considered evanescent if at least one component of $\mathbf{k}$ is imaginary [8]. For example, in air ($n = 1$) and for real k_x and k_y, a $\sqrt{k_x^2 + k_y^2} > k_0$ requires an imaginary k_z, which according to Eq. 1.2 corresponds to an exponentially decaying field in the z direction. Conversely, a plane wave requires all components of $\mathbf{k}$ to be real. For example, a real k_z in air requires the (real) k_x and k_y to satisfy $\sqrt{k_x^2 + k_y^2} \leq k_0$. Hence, when no evanescent waves are present, there is a limit to the magnitude of the possible wavevectors.

Conventional optics (such as microscope objectives and lenses) use a superposition of plane waves to create a focal region. The requirement for plane waves, causes a minimal size to which light waves can be focused in air. This limitation, which is commonly referred to as the diffraction limit, was first derived by Abbe in 1873 [12]. Through Fourier mathematics it can be shown that the diffraction limit can be approximated with [13]

$$\Delta x \approx \frac{2\pi}{\Delta k_x} = \frac{\lambda_0}{2}, \tag{1.4}$$

where Δx is the smallest spread in positions to which light can be focused in x and $\Delta k_x = 4\pi/\lambda_0$ is the maximal spread of available plane-wave wavevectors. Identical expressions can straightforwardly be derived for y

and z. The diffraction limit is a ubiquitous problem for microscopy techniques that aim to resolve features smaller than Δx and clever schemes to measure at higher resolutions whilst using propagating waves have been developed. For example, in structured illumination microscopy a sample can be illuminated with distinct grating orders to achieve 'super resolution' [14], and fluorescence microscopy methods typically use the knowledge that the detected light comes from fluorescent point sources to convert a diffraction limited image to a higher resolution image [15].

1.2 Optical fields near nanophotonic structures

Nanophotonic structures gain many of their unique properties because $\epsilon_r(\mathbf{r})$ varies on a (highly) subwavelength scale. In such an inhomogeneous environment electromagnetic fields adapt to the spatially varying permittivity, and consequently, unlike in homogeneous media, $\mathbf{E}(\mathbf{r}, t)$ and $\mathbf{H}(\mathbf{r}, t)$ vary on a highly subwavelength scale.

Associated with the subwavelength structure of the optical fields, are wavevectors larger than those allowed for plane waves (see Sec 1.1.1). These wavevectors necessarily belong to evanescent waves that decay away from the nanophotonic structure. The spatial region where evanescent waves make up a large fraction of the optical field is commonly referred to as the optical near field.

We illustrate the subwavelength structure of optical near fields with a calculation of the fields near a 'bow-tie' nanoantenna (see Fig. 1.1a shows the antenna geometry and Fig. 1.1b the field enhancement near the antenna) [16]. The field enhancement map in Fig. 1.1b, which was obtained with an illumination wavelength of 780 nm, reveals that the optical field near a nanophotonic structure can be confined to only a few tens of nanometers. Specifically, this calculation highlights that nanophotonic structures can control the optical field on length scales much smaller than the optical wavelength.

Many additional insights into the interaction between light and matter can be obtained by considering the orientation of the electric optical fields. For example, a full vectorial treatment of the electric fields is required to understand the interaction of light with non-symmetric particles (such as many molecules, QDs or nanoantennas), whose optical response depends

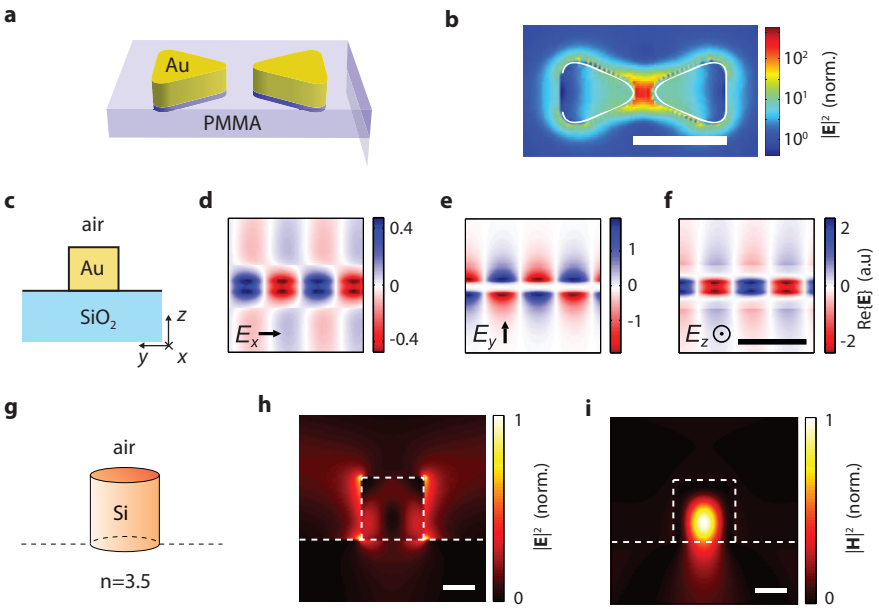

Figure 1.1: Simulated optical fields near prototypical nanophotonic structures. **a** Sketch of a gold (Au) bow-tie nanoantenna on a PMMA (n=1.5) substrate. **b** Calculated intensity enhancement near a bow tie antenna illuminated with light with a free space wavelength of 780 nm. White contours indicate the bow tie geometry. The scale bar indicates 100 nm. **c** Sketch of a cross-cut through a gold nanowire on a glass (SiO_2) substrate. The nanowire extends in the x- direction. **d**-**f** show the real part of the calculated x, y and z-component of the electric field 20 nm above the sample respectively. The frequency of the mode corresponds to a free space wavelength of 1550 nm. The scale bar in **f** indicates 1 μm. **g** Sketch of a silicon (Si) cylindrical nanoparticle on a (n = 3.5) substrate. **h** (**i**) cross-cut of the calculated electric (magnetic) intensity near the nanoparticle. The particle is illuminated with light with a free space wavelength of 500 nm. Scale bar indicates 50 nm. **a**,**b** are adapted from [16], **d**-**f** are adapted from [17] and **g**-**i** are adapted from [18].

strongly on the local electric field orientation. Near nanophotonic structures this field orientation can vary on a nanometer scale. The nanoscale variation of the optical field orientations is intimately linked to the boundary imposed by Maxwell's equations. For example, from these equations it follows that the electric field parallel to an interface has to be continuous across that interface; satisfying this requirement in a nanophotonic environment, where typically many orientations of interfaces occur in a given volume of λ_0^3, typically requires all components of the optical electric field to be present.

As an example of the 3 dimensional nature of the electric field vector we consider the propagation of light in a metallic nanowire. These nanowires are candidates for the transport of information in optical circuit components (in this case along x in Fig. 1.1c). In Fig. 1.1d-f we show calculations of the vectorial electric field distribution near this nanowire waveguide [17]. These calculations demonstrate both that all electric field components are present and that near the nanowire the spatial dependence of these field components can be drastically different.

A control over the local vectorial electric field distribution is useful in many applications. For example, in optical tweezing intricately structured far fields are used to control the spin or orbit of particles. Furthermore, these local vector fields can carry quantum mechanical properties such as spin and orbital angular momentum, and knowledge of the local vector fields is required to understand the transfer of these properties between the fields and matter.

In the interaction of light with matter, the optical magnetic field is typically ignored, because its interactions with matter are usually much weaker than those of the electric field [8]. However, recently, magnetic light matter interactions have attracted considerable interest. For example, metamaterials that interact strongly with the magnetic field of light were developed [19, 20], and magnetic dipole transitions have attracted considerable attention [21, 22, 23]. Interestingly, because $\mathbf{E}$ and $\mathbf{H}$ are related through their curl (see Eq. 1.1), an electric field, whose orientation and amplitude varies in all three dimensions in a volume of λ_0^3, typically has a different spatial distribution than the magnetic field.

This effect can even be observed in prototypical dielectric scattering objects, such as Si nanoparticles (sketched in Fig. 1.1g), which are used in for example nanophotonic solar cells [24]. In Fig. 1.1h and i we illustrate

the different distribution of the nanoscale electric and magnetic fields, with a recently published calculation of the electric and magnetic fields near such a Si nanoparticle [18]. These calculations demonstrate a maximal magnetic field in the center of the particle, whereas the electric field primarily located at the outside and the corners of the particle. Hence, even in such a simple nanophotonic structure, $|\mathbf{E}|$ and $|\mathbf{H}|$ can be distributed very differently, and an understanding of the light matter interactions in such a structure requires the knowledge of both.

In this thesis, we refer to the subwavelength variations of the vectorial electric and magnetic optical fields, which we discussed in this section, as the structure of optical fields.

1.3 Optical fields in waveguiding structures

Nanophotonic waveguides both guide light waves on nanophotonic chips and structure the optical field at the nanoscale. Much like the wires in current electronic circuits, these optical waveguides can form an important part of optical circuit components and hybrid electro-optical circuits. Furthermore, by cleverly structuring the waveguides, they can enable an extensive (active) control over light. Examples of this control are the slow-down of light [25, 26], (optical) switching [27, 28] and enhanced nonlinear effects [29, 30]. In this section we discuss two basic phenomena that enable the guiding of light in nanophotonic waveguides. Specifically, we show how total internal reflection enables slab and rib waveguides, and how the creation of a photonic bandgap enables photonic crystal waveguides. We illustrate this explanation with a general description of how the optical fields evolve in and near these waveguides.

1.3.1 Total internal reflection

Total internal reflection (TIR) is fundamental to many waveguiding structures. In Fig. 1.2a we sketch a plane wave in the yz-plane that undergoes TIR when it encounters a lower index medium along constant z. Because the medium is homogeneous along x and y, the wavevector in these directions is conserved. From Eq. 1.3 it follows that in the low index material $k_z = \sqrt{n^2k_0^2 - (k_x^2 + k_y^2)}$. A wave incident under oblique angles, has a purely imaginary k_z, when $k_x^2 + k_y^2 > n_{low}^2 k_0^2$. The field such an imaginary

k_z decays evanescently into the lower index medium (right part of Fig. 1.2a, see Sec. 1.1.1). Because light with an imaginary wavevector cannot transport energy [8], the incident light is totally reflected at the $z = 0$ interface. This phenomenon, TIR, is intensively used to guide light in nanophotonic waveguiding structures.

1.3.2 Slab waveguides

One of the simplest waveguide geometries is a slab waveguide. A slab waveguide is formed by sandwiching a high index slab between two lower index slabs (see Fig. 1.2b). These structures can confine light to the higher index slab by means of TIR. In thin slabs (with a thickness of the order of or smaller than the wavelength of light in the slab) only discrete solutions to Maxwell's equations exist for the propagation of light in the waveguide. These solutions to Maxwell's equations (in the absence of sources) are commonly referred to as the (eigen) modes of a structure [31]. In a slab waveguide, each eigenmode is associated with a wavevector that quantifies its wavelength ($\lambda_{slab} = k_0\lambda_0/k_{slab}$) along the propagation direction in the slab. This wavevector can be tuned by the geometry of the waveguide. That is, it can be analytically shown that the thinner the slab, the lower k_{slab} of the lowest order mode [32] (see also Sec. 1.3.3).

Rib waveguides

The different effective refractive indices for different thickness slabs enable so-called rib waveguides (sketched in Fig. 1.2c) that confine light in two dimensions and guide it in the third. A rib waveguide essentially consists of three adjacent slab waveguides, of which the middle slab has an increased thickness. Importantly, the wavevector of the mode in the thinner slabs is lower than in the thicker middle slab and TIR can occur at the interfaces between adjacent slabs. For some slab geometries this allows rib waveguides to confine light to the middle slab.

1.3.3 Photonic crystal waveguides

In addition to guiding light by means of TIR, photonic crystal waveguides use a periodic structuring of matter to guide light. This periodic structuring gives rise to a region of frequencies at which light cannot propagate in the crystal (a photonic bandgap).

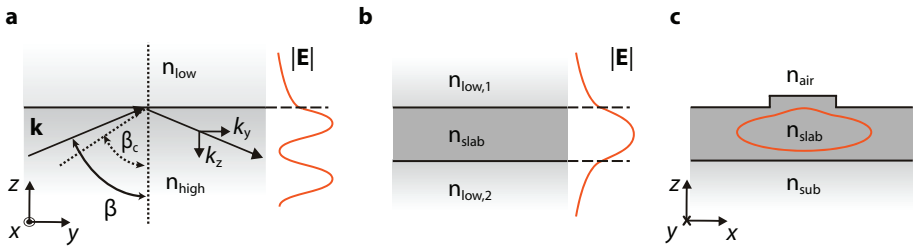

Figure 1.2: Guiding light by means of TIR. a Left: schematic representation of a light ray (with wavevector $\mathbf{k}$) undergoing TIR. The angle β_c is defined by $k_x^2 + k_y^2 = n_{low}^2 k_0^2$, for values of $k_x^2 + k_y^2$, $\beta > \beta_c$ and the light is totally reflected from the interface. Right: cross-cut along z of the amplitude of the electric field associated with a plane wave undergoing TIR. The standing wave in n_{high} is caused by interference between the incident and the reflected wave. The exponential decay indicates the evanescent field in n_{low}. **b** Left: Schematic representation of light ray confined in a dielectric slab. Right: cross-cut along z of the amplitude of the electric field of the lowest order mode in the slab. The wave exponentially decays into the two low n media. The coordinate system of **a** and **b** is shown in the bottom left corner of **a**. **c** Sketch of a rib waveguide. The orange line outlines a typical iso-amplitude line of the mode.

Much of the physics that gives rise to a photonic bandgap, can be understood from the propagation of light in a Bragg stack (see Fig. 1.3a), which is in essence a one dimensional (1D) photonic crystal. The optical waves in this structure have to follow the periodicity imposed by the lattice along y. That is, according to Bloch's theorem $\mathbf{E}_k(y) = e^{ik_y y}\mathbf{u}_k(y)$, where $\mathbf{u}_k(y) = \mathbf{u}_k(y+a)$ is a periodic function with the same periodicity as the crystal. The time harmonic electric field of the Bloch mode at a frequency ω_l can be written as a superposition of plane waves (Bloch harmonics) [33]

$$\mathbf{E}_k^l(y) = \sum_m \mathbf{a}_m^l(k) e^{i\left(k_y + m\frac{2\pi}{a}\right)y}, \text{ where } m \in \mathbb{Z}, l \in \mathbb{N} \tag{1.5}$$

where $\mathbf{a}_m^l$ indicates the amplitude and orientation of the m^{th} Bloch harmonic in the l^{th} energy band. For each value of k, l the optical Bloch mode is made up out of an infinite number of Bloch harmonics. Because each Bloch mode has Bloch harmonics in each Brillouin zone, all distinct Bloch waves occur for k-values within the first irreducible Brillouin zone ($-\pi/a < k_y \leq \pi/a$) [34]. Furthermore, for almost all photonic crystals $\omega_l(k) = \omega_l(-k)$ [33] and all distinct Bloch waves occur between $k_y = 0$ and $k_y = \pi/a$. The frequencies of each mode constitute the dispersion relation of the crystal, from which many of the crystal's optical properties can be inferred.

In the case of a Bragg stack, formed by two alternating layers of different refractive index, an exact expression for this dispersion relation exists [35]. In Fig. 1.3b we show the calculated dispersion relation of a Bragg stack formed by adjacent layers of 180 nm Si ($n_1 = 3.5$) and 240 nm air ($n_2 = 1$). Here, the dashed black line illustrates that a Bloch wave (mode) is composed of Bloch harmonics (black dots) in all Brillouin zones.

At the edges of the Brillouin zones ($k_y = (2m+1)\pi/a$) the wavelength of the Bloch harmonics is $(2m+1)$ times the lattice periodicity. If we consider the fundamental Bloch harmonic, there are two ways of positioning the nodes of its field on the lattice: on the high (blue dots, Fig. 1.3b) and on the low refractive index (red dots, Fig. 1.3b). This straightforwardly extends to higher harmonics that have an odd number of nodes in one of the indices. Because the field of the Bloch modes indicated by the red and blue dots is distributed differently over the two refractive indices in the Bragg stack, these modes cannot have the same energy ($U(\mathbf{r}) \propto \sqrt{n}\,|\mathbf{E}(\mathbf{r})|^2$, where $U(\mathbf{r})$ is the energy of the mode and n is real [33]). Associated with

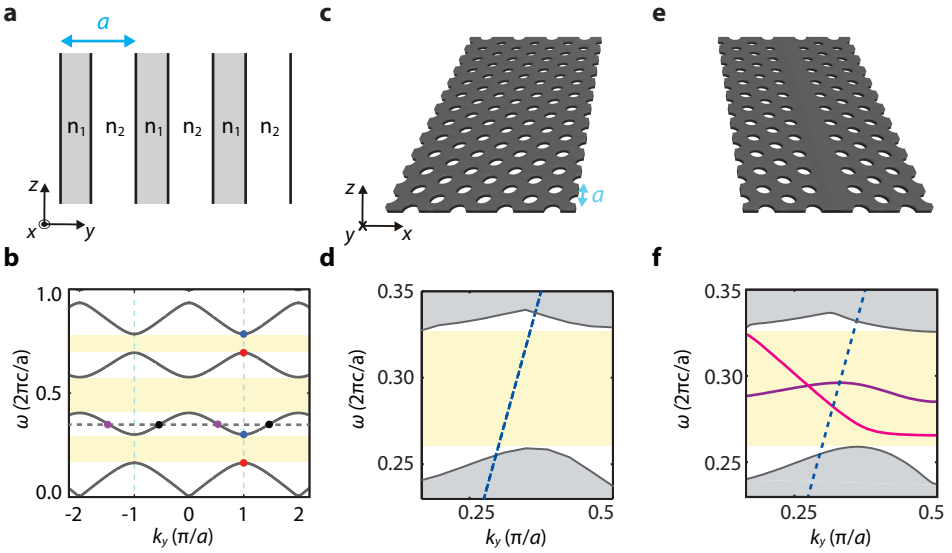

Figure 1.3: Photonic crystal geometries and dispersion relations. a Sketch of a 1D photonic crystal that is formed by layers of alternating index n_1 and n_2 with a lattice periodicity a. **b** Calculated dispersion relation of a 1D photonic crystal (crystal geometry is outlined in the text). Black (and purple) dots show the forwards (and backwards) propagating Bloch harmonics of a Bloch wave at a frequency indicated by the gray dashed line. The yellow shaded region indicates the photonic bandgap. The high (and low) energy modes on opposite sides of the bandgap are indicated by blue (and red) dots, respectively. Light blue dashed lines show the edges of the Brillouin zones. **c** (and **e**) Sketch of a 2D photonic crystal (and a PhCW) geometry, respectively. The axis orientation of **c** and **e** is shown in the bottom left of **c**. **d** (and **f**) Calculated dispersion relation of a 2D photonic crystal (and a PhCW formed by a missing row of holes). The crystal geometries are outlined in the text. The yellow region indicates the photonic bandgap. The gray region shows the continuum of available modes. The blue dashed line shows the light line. The pink (and purple) lines in **f** show the waveguide modes.

this energy difference is the existence of a photonic stop-gap (yellow regions, Fig. 1.3b), where no optical modes are supported by the crystal.

Although one-dimensional photonic crystals were already theorized in 1887 [36], it was not until 1987 that Yablonovitch theorized two- (2D) and three-dimensional (3D) photonic crystals showing a complete photonic bandgap in all directions in the crystal [37]. A 'two-dimensional photonic crystal' can be made by perforating a thin Si slab with a hexagonal pattern of holes (see Fig. 1.3c). In Fig. 1.3d we show the calculated dispersion relation of a 2D photonic crystal, with a lattice periodicity $a = 420$ nm, formed by air holes with a diameter of 240 nm in a 220 nm thin Si slab [38]. Along y, this dispersion relation contains a continuum of modes above and below the bandgap (gray shaded regions in Fig. 1.3d). Importantly, a bandgap across all wavevectors in the plane of the photonic crystal slab is present (yellow shaded region in Fig. 1.3d). In this thesis we only study transverse electric (TE) modes, which in the center of the slab have no magnetic field along the slab, however our photonic crystal also shows a complete bandgap for transverse magnetic modes, which in the center of the slab have no electric field along the slab.

By leaving out one row of holes from the lattice of the 2D photonic crystal a line defect can be formed, which can act as a nanophotonic waveguide (as sketched in Fig. 1.3e). Fig. 1.3f depicts the calculated dispersion relation for a photonic crystal waveguide (PhCW), which is formed by leaving out one row of holes from the previously used 2D photonic crystal. In this dispersion relation, we can identify two waveguide modes (pink and purple lines). These modes are confined to the slab by means of TIR and cannot propagate into the slab due to the photonic bandgap. In this thesis, we will focus on the lowest frequency mode (pink) line, which is intensively studied for the shape of its dispersion relation. The speed with which light propagates in the waveguide (v_g) is inversely proportional to the gradient of the dispersion relation, that is

$$v_g = \frac{c}{n_g} = \frac{d\omega}{dk}, \tag{1.6}$$

where c is the speed of light in vacuum and n_g is the group index that quantifies the slow down of light relative to propagation in air. Hence, a positive (and negative) slope of the dispersion relation corresponds to a

forward (and backward) propagating wave. For example, in the dispersion relation of the 1D Bragg stack, we can associate the gray (and black) dots with the Bloch harmonics that make up the forward (and backward) propagating Bloch mode.

Strikingly, the gradient of the dispersion relation of a PhCW completely flattens out at $k = \pi/a$ (see Fig. 1.3d), indicating that light can be slowed down enormously. This fascinating property of PhCWs has attracted huge interest [6, 39, 40, 41, 30, 28, 25]. When light propagates so slowly through the waveguide, photonic crystal waveguides increase the interaction between light and matter. This control over the flow of light allows for spectacular applications such as ultrafast switches [28], an all optical delay line [6], and efficient harmonic generation [30].

The evanescent field of a Bloch wave

The structuring of matter in PhCWs is associated with intricately structured optical fields. As an example Fig. 1.4a, presents a calculation of $|\mathbf{E}|^2$ at various heights near the PhCW used in the previous section. Like the fields near the nanophotonic structures described in Sec. 1.2 the fields closest to the structure vary on a nanometer scale. Moving away from the surface, we observe that these spatial variations appear to blur, and that the mode extends over a large area.

The spatial frequency content of the Bloch wave at increasing heights above the PhCW can provide much insight into the evolution of the field structure [42]. In Fig. 1.4b we show a calculation of the dispersion relation of the first few Bloch harmonics. The horizontal dashed line in Fig. 1.4b intersects the dispersion relation both when it has a positive and a negative slope. From Eq. 1.6 it follows that these intersections are associated with the harmonics of the forwards (indicated with colored circles) and the backwards propagating Bloch modes. For symmetry reasons these modes show identical intensity distributions and we consider only the forward propagating mode. According to Eq. 1.3 the wavevector along the propagation direction of each Bloch harmonic is associated which a unique out of plane wavevector. Hence, each harmonic decays at a different rate in the out of plane direction away from the structure. We illustrate the different decay of the Bloch harmonics with the calculations shown in Fig. 1.4c. This figure shows that the normalized energy in the $m = -2$ and $m = +1$ Bloch

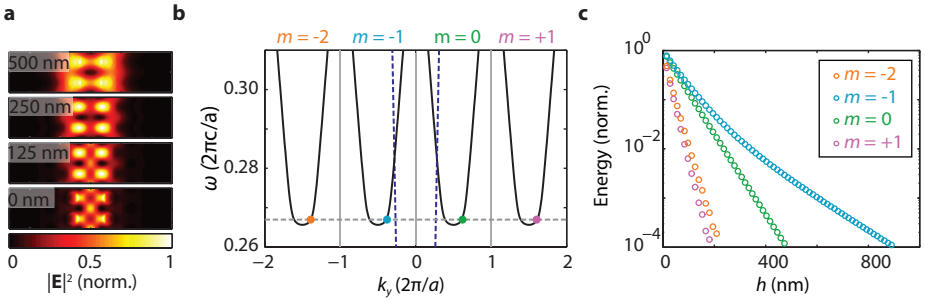

Figure 1.4: Evanescent structure of a Bloch wave. **a** Maps of $|\mathbf{E}|^2$ above the PhCW, at heights h indicated in the top left of each panel. When $h = 0$, the distance to the PhCW surface is 20 nm. The intensity in each panel is normalized to the maximal intensity at that height. All panels are 8 µm wide and 2µm high. **b** Dispersion relation of the first few Bloch harmonics. The horizontal dashed line indicates the optical frequency of $\omega = 0.27 \cdot (2\pi c/a)$Hz corresponding to a wavelength of 1576 nm. Vertical dashed lines indicate the Brillouin zone edges. **c** Energy in the $m = -2, -1, 0, 1$ Bloch harmonics at increasing h. The energy in each harmonics is normalized to its energy at $h = 0$ above the PhCW

harmonics is reduced by over 4 orders of magnitude only 250 nm above the surface.

At these heights, the optical field is made up out of a different combination of wavevectors than at the surface and the field profile above the waveguide drastically changes. The evolution of the optical field with increasing distance emphasizes the intricate structure of the fields close to nanophotonic structures.

Interestingly, the magnetic field, which can be found via the curl of the electric field that reshapes with height (see Sec. 1.2), can show a spatially different evolution for increasing height. We study the structure of electric and magnetic vector fields above a PhCW in more depth in chapters 4 and 6.

1.4 Emission modification by nanoscale optical fields

Nanophotonic structures can also influence the emission characteristics of nearby emitters [43, 8, 37, 44]. Typically, these emitters are two level systems, such as fluorescent atoms, molecules, QDs or nitrogen-vacancy

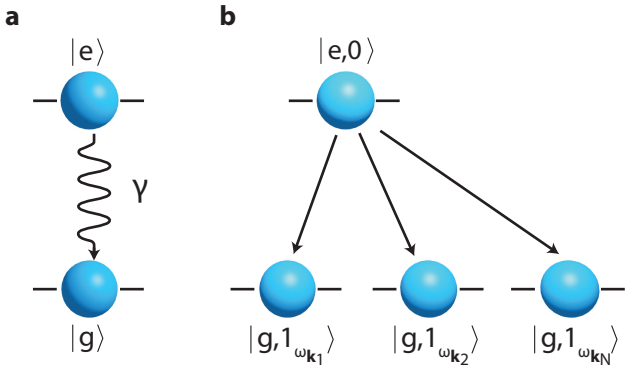

Figure 1.5: Emission of a two-level system. **a** Schematic of an emitter that can relax from its initial ($|e\rangle$) to its final state ($|g\rangle$) by the emission of a photon, with a decay rate γ. **b** An emitter in its excited state, which is associated with zero photons, can emit a photon at frequency ω to either one of the ground states $k_1$to k_N.

centers, that emit a single photon upon relaxation. The redistribution of charges in the emitter that gives rise to the emission of a photon is typically described by a transition dipole [45]. The probability per unit time that a two level systems relaxes from its initial excited ($|e\rangle$) to its final ground state ($|g\rangle$) is called the decay rate γ (see Fig. 1.5a). The decay rate is determined by a combination of factors intrinsic to the emitter (such as the overlap of its excited and ground state wave functions) *and* the amount of available modes to which a photon can be emitted Fig. 1.5b.

Mathematically, the number of available states and the emitter's intrinsic properties are combined via Fermi's Golden Rule. If the emission of a photon is mediated by a dipolar interaction that can emit into a continuum of states, Fermi's Golden Rule can be written as

$$\gamma = \frac{\pi\omega}{3\hbar\epsilon_0}|\mu|^2\rho(\omega, \mathbf{r}, \hat{\mathbf{d}}), \tag{1.7}$$

where μ quantifies the intrinsic coupling between the excited and ground states and $\rho(\omega, \mathbf{r}, \hat{\mathbf{d}})$ the density of optical states available to a transition dipole oriented along $\hat{\mathbf{d}}$.

Nanophotonic structures, by virtue of their structuring of the available photonic modes, offer a great control over $\rho(\omega, \mathbf{r}, \hat{\mathbf{d}})$. Specifically, as was first realized by Sprik *et al.* [46], whereas in bulk optics one can

typically simply count the number of modes to find a 'density of states', in nanophotonic structures these modes vary on a subwavelength scale and consequently one needs to account for the 'local density of optical states' (LDOS). The spatial dependence of the LDOS in Eq. 1.7 is included by its dependence on $\mathbf{r}$. The LDOS can be computed via $\rho(\omega, \mathbf{r}_0, \hat{\mathbf{d}}) = Im\langle\hat{\mathbf{d}}|\overleftrightarrow{G}(\omega, \mathbf{r}_0, \mathbf{r}_0)|\hat{\mathbf{d}}\rangle$. Here $\overleftrightarrow{\mathbf{G}}(\omega, \mathbf{r}, \mathbf{r}_0)$ is the environment's Green's dyadic [8], which in the case of an electric dipole ($\mathbf{p}(\mathbf{r}_0)$) is a three by three tensor that projects the dipole onto its radiated field ($\mathbf{E}(\omega, \mathbf{r}) \propto \overleftrightarrow{\mathbf{G}}(\omega, \mathbf{r}, \mathbf{r}_0)\cdot\mathbf{p}(\mathbf{r}_0)$). This projection of $\mathbf{p}(\mathbf{r}_0)$ onto $\mathbf{E}(\omega, \mathbf{r}_0)$ with $\overleftrightarrow{\mathbf{G}}(\mathbf{r}_0, \mathbf{r}_0)$ describes how an environment affects an emitter's ability to radiate.

The emission enhancement or reduction of an emitter near a nanophotonic structure relative to free space has attracted considerable interest. Because the prefactor $(\pi\omega\left|\mu\right|^2/(3\hbar\epsilon_0))$ in Eq. 1.7 remains constant upon placement near such a structure, we need only consider the change in LDOS. Consequently the emission enhancement can be calculated via

$$F(\omega, \mathbf{r}_0, \hat{\mathbf{d}}) = \frac{Im\langle\hat{\mathbf{d}}|\overleftrightarrow{\mathbf{G}}(\omega, \mathbf{r}_0, \mathbf{r}_0)|\hat{\mathbf{d}}\rangle}{Im\langle\hat{\mathbf{d}}|\overleftrightarrow{\mathbf{G}}_{vac}(\omega, \mathbf{r}_0, \mathbf{r}_0)|\hat{\mathbf{d}}\rangle}. \tag{1.8}$$

In cavity type structures F is commonly referred to as the Purcell factor [44], while in waveguiding it is called the emission enhancement factor [47]. Importantly, $\overleftrightarrow{G}_{vac}(\omega, \mathbf{r}_0, \mathbf{r}_0)$ does not depend on the orientation and position of the dipolar source and can be found analytically to be $G_{vac}(\omega) = \omega^3\sqrt{\epsilon_d}/\left(6\pi c^3\right)$.

Over the last two decades, photonic crystal waveguides [47, 48] and bulk photonic crystals [46, 49, 37] have been intensively investigated because they can greatly speed up or almost completely inhibit the emission of nearby emitters. In these applications typically linear electric dipoles are considered. Conversely, in chapter 7, we investigate nanophotonic emission control of circular electric and magnetic dipoles by nanophotonic structures. Circular dipoles are of particular interest because, as we describe in chapter 7, they are associated with orbital angular momentum changing transitions.

1.5 Outline of this thesis

In this thesis, we experimentally and numerically study the distribution of optical electric and magnetic vector fields near nanophotonic structures,

and we study how these structures affect the emission of electric and magnetic circular dipoles.

In chapter 2, we introduce aperture type near-field scanning optical microscopy as a tool for studying nanoscale optical vector fields. We introduce how this type of microscope can be used to map the phase and amplitude of two orthogonally polarized signals. Central to this thesis is the question how we could use these two channels to map all six (three electric and three magnetic) components of the optical vector fields and how these fields affect nearby emitters. Evidently, such a mapping requires both an increase of the number of simultaneously detected channels and it requires the ability to relate the signal in these channel to optical near-field components.

In chapter 3, we firstly investigate how the mirror symmetries of nanoscale optical fields can be used to open up an additional detection channel and to reduce the noise in near-field measurements. Then, we study if we can use this channel to map an additional components of the optical near field.

In chapter 4, we present a detailed experimental study of the relation between the optical electric and magnetic near fields and the signal in the two orthogonally polarized channels. Furthermore, we investigate how this sensitivity to **E** and **H** is affected by the geometry of the probe of our near-field microscope.

In chapter 5, we underpin the experimental detection of **E** and **H** with calculations of the signal of a near-field scanning optical microscope. We use the optical reciprocity theorem to both simplify these calculations and to provide insight in the process of image formation. As an outlook, we present a method, based on the optical reciprocity theorem, that could be used to separate the signal from the electric and magnetic near fields.

In chapter 6, we use the work of the previous chapters to investigate the properties of optical electric and magnetic near fields near a PhCW. We investigate the presence of the phase- and polari-zation-singularities that are linked to the orbit and spin of nearby particles, respectively. Furthermore, we investigate how these fields evolve with height above the PhCW.

In chapter 7, we use our near-field microscope to investigate the control over the emission direction of circular dipoles offered by PhCW. The helicity of circular dipoles is associated to the spin-states of solid-state emitters. Hence, we study the possibility of a deterministic coupling between dipole helicity to photon path, which would implicate the possibility

of an nanophotonic interface between coupling between the spin state of a solid-state emitter and the path of the photon it emits.

In chapter 8, we study the control over helicity-to-path coupling in PhCW in more depth. We map the coupling between both electric and magnetic dipole helicity to photonic path and we investigate how this coupling is affected by tuning the wavelength.

Finally in chapter 9, we discuss how the knowledge of vectorial near fields could be used to create a highly efficient sensor for magnetic circular dichroism.

2

Measurement of nanoscale optical fields

An ideal measurement of the optical properties of nanophotonic structures requires a technique that detects nanoscale electric and magnetic optical fields in a phase- and polarization-resolved manner. In this chapter we introduce the near-field scanning optical microscope (NSOM) that we use in this thesis to probe the optical fields near nanophotonic structures. We start by explaining how an aperture type NSOM maps the intensity of the optical field near nanophotonic structures. Afterward, we explain how such an aperture type NSOM can be set up to provide access to the phase and orientation of the optical near field. Lastly, we use our NSOM to study the scattering of a subwavelength hole in a metal film and we relate the scattering by this hole to sensitivity of our NSOM probe.

2.1 Measurement of the optical intensity

A technique that can measure optical fields at resolutions beyond the diffraction limit is extremely useful for the investigation of the optical properties of nanophotonic structures. The first idea for an experimental setup that would enable measurements with a highly subwavelength resolution

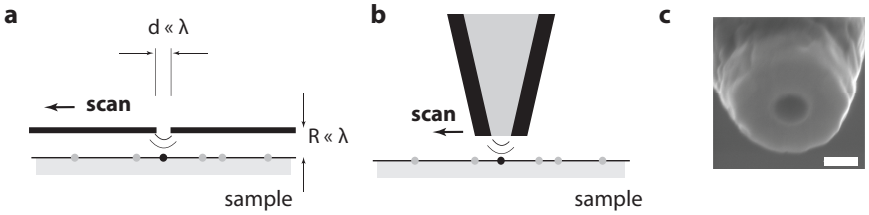

Figure 2.1: Aperture based near-field scanning optical microscopy. a The original concept proposed by Synge. An optically thick metal film (black line) with a subwavelength aperture, whose diameter (d) is much smaller than the wavelength (λ), is scanned over a sample on a distance $R \ll \lambda$. **b** Schematic of an aperture probe. This probe consists of a dielectric core (gray), that is coated with an optically thick metallic cladding (black). **c** Scanning electron microscope (SEM) image of a real aperture probe that consists of a glass core coated with aluminum. Scale bar indicates 200 nm. Figures **a** and **b** were adapted from [51].

dates back to 1928 [50]. In that early work, Synge suggested to illuminate a subwavelength hole in an opaque film to create a subwavelength light source (see Fig. 2.1a). Raster scanning this source (using a piezoelectric crystal) over predefined positions, nanometers away from a sample, and recording the transmitted signal, would create a subwavelength mapping of the sample's optical response.

The fundamental mechanism behind Synge's idea is that the highly spatially confined and therefore evanescent waves (see Sec. 1.1.1) associated with the subwavelength structure of the hole can couple to the sample and thereby provide subwavelength information about its optical properties. Because the evanescent fields decay rapidly away from the hole, the distance of the hole to the sample needs to be kept in the nanometer range, which requires a sophisticated mechanism [52].

Due to extreme technical difficulties, such as probe sample distance control and the low throughput of aperture type near-field probes (order 10^{-3} to 10^{-7}) [53, 8], it was not until 1984 that the first near-field image was recorded [54], with an aperture near-field probe (as shown in Fig. 2.1b and c). This breakthrough and the work by Betzig [55], sparked a flurry of near-field microscopy activity at laboratories across the globe.

Early NSOMs were typically used to locally illuminate a sample (illumination mode), and offered an, at the time, unique ability to couple to single

molecule emitters [56]. A big advancement of the possible applications of near-field scanning optical microscopy was made, when the emission of the probe itself was shown to mimic that of a dipolar source, thereby allowing NSOMs to probe the LDOS [57, 58]. Furthermore, not long after its initial development, the NSOM was first used in collection mode experiments [59], where light was collected from the evanescent optical fields near a sample.

Nowadays, additional near-field scanning optical microscopy schemes such as scattering-type [60] and transmission-based near-field scanning optical microscopy [61] coexist with the traditional aperture type NSOM. Of these schemes the scattering type NSOM has proven particularly useful for the study of nanoantennas [62, 63, 64]. This type of NSOM, which couples light out of a sample by placing a highly subwavelength scatterer in the sample's evanescent field, can map the optical fields near a sample with spatial resolution of a few nanometers over a broad range of wavelengths.

In this thesis, we will use an aperture type NSOM. As an example of a collection mode experiment using an aperture probe, Fig. 2.2 depicts an intensity map above a prism in which two counter-propagating waves undergo TIR [65]. Although theoretically such counter-propagating waves are well understood, this measurement from 1994 is one of the first experimental visualizations of the distribution of the optical intensity near such a simple system. Furthermore, this measurement underpins both the nanoscale confinement of evanescent optical fields and the high resolution that can be obtained by means of aperture type near-field scanning optical microscopy.

2.2 Vectorial measurement of nanoscale optical fields

The flow of light at the nanoscale is characterized not only by the optical intensity, but rather by the complete electromagnetic vector (see Sec. 1.2). In this section we introduce two experimental techniques that allow us to extract information on the phase and the orientation of the optical field near a sample.

2.2.1 Phase-resolved detection

Access to the optical phase can be gained by incorporating the NSOM in an interferometric detection scheme (as sketched in Fig. 2.3). Specifically, we use a heterodyne detection scheme, in which the light from the probe

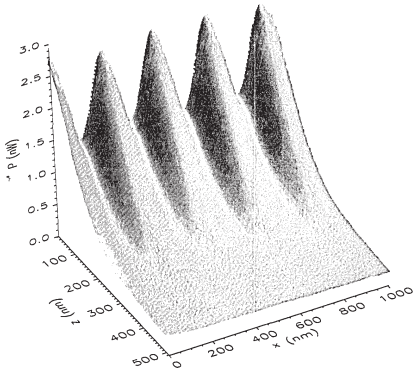

Figure 2.2: Early near-field intensity measurement. Near-field scanning optical microscopy measurement of the evanescently decaying power in two totally internally reflected and counterpropagating plane waves above a prism. The axes show the position of the probe along the prism (x), away from the prism plane (z) and the power of the signal measured on each position. Figure adapted from [65]

interferes with the frequency shifted reference radiation from the reference branch (see Fig. 2.3).

The frequency of the reference branch is shifted by 40 kHz using two acousto-optic modulators (AOMs) (see Fig. 2.3). AOMs frequency shift an incident beam using a 'moving' acoustically generated grating. We select the first (+1) diffracted order of the first AOM, which is shifted up in frequency by 80.04 MHz. Of the second AOM we use the -1 order, which is shifted down in frequency by 80.00 MHz. Hence, the angular frequency difference between the two interferometer branches becomes $\Delta\omega = 2\pi \cdot 40\text{kHz}$.

On the photodetectors we measure the intensity of the superposition of the fields in the signal and the reference branch (see Fig. 2.3). That is, ignoring the effect of signal and reference branch polarization, the voltage measured from the photodetectors, V^D, is given by

$$V^D = \eta^D \left[|E^R|^2 + |E^S|^2 + 2|E^R||E^S| \cos(\Delta\omega t + \Delta\phi) \right], \qquad (2.1)$$

where η^D is the detector efficiency, E^R (E^S) are the electric field of the reference (signal) branch on the photodiode, respectively, and $\Delta\phi = \phi^R - \phi^S$ is the phase difference between the reference and signal branches.

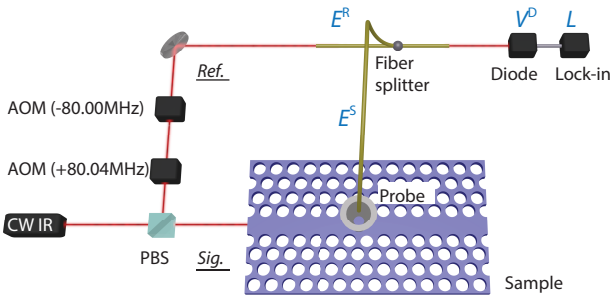

Figure 2.3: A phase-sensitive NSOM. Light from a continuous wave infrared laser (CW IR) is split up into a signal (Sig.) and a reference (Ref.) branch. The reference branch is frequency shifted using two AOMs before it is coupled to a fiber (yellow tube). The signal branch is coupled to a sample, from where light is collected by a near-field probe. Light from the probe propagates through the fiber, where it joins the reference branch. The two signals are converted to a free-space beam and the combined signal is detected on a photodiode, whose signal is analyzed by a lock-in detector. The blue annotations in the figure correspond to the notation used in the text for the fields and signals in the reference and signal branch, the photodiode and the lock-in detector.

We analyze this signal with a lock-in detector that selects only the signal that oscillates around the beating frequency (the right most term in Eq. 2.1). Because only frequencies in a narrow window (25 - 80 Hz) around the beating frequency are kept by the lock-in detector, noise, and in particular $1/f$ noise, is efficiently suppressed. The output voltages of the lock-in detector can be straightforwardly combined to the complex signal L [66]

$$L = \eta^D |E^R||E^S| e^{i(\phi^R - \phi^S + \phi^{LI})}, \tag{2.2}$$

where ϕ^{LI} is a phase offset set by the lock-in. From this expression we can note that the amplitude of L, which is $\eta^D|E^R||E^S|$, is a factor $\gamma = |E^R|/|E^S|$ larger than the signal from the signal branch on the photodiode alone ($|E^S|^2$). By choosing $E^R \gg E^S$, amplification of the signal from E^S (heterodyne gain) by factors of over three orders of magnitude is achieved. This is useful for near-field microscopy that typically deals with the challenge of detecting extremely weak signals (see Sec. 2.1).

Importantly, the phase of the complex exponential in Eq. 2.2 is directly

related to the phase in the optical near field. That is, because ϕ^{LI} and ϕ^{R} are kept constant, all variations in the phase of L are caused by ϕ^{S}. Hence, from L we can learn how the optical phase evolves in and near the sample.

2.2.2 Polarization-resolved detection

In addition to the optical phase, a NSOM ideally enables measurements of the orientation of the electric and magnetic fields near a sample. To this end, a NSOM can be set up to measure the polarization of the light emerging from the detector fiber. To resolve this polarization, we use a second polarizing beamsplitter (marked by PBS in Fig. 2.4a), which ensures that light polarized along x and y contributes to the signals L_x and L_y, respectively. An important part of polarization-resolved near-field scanning optical microscopy is the relation between these polarization directions at the beamsplitter and the optical field components near the sample. An obstacle that has to be overcome to, for example, be able to relate light from electric fields along x and y near the sample (indicated in 2.4) to x- and y-polarized light (now in the lab frame) at the detectors, respectively, is that the light experiences birefringence in the fibers after the probe.

As is the case with (almost) every fiber, the fibers in the signal and reference branch of our NSOM are slightly birefringent because of, for example, stress due to bending and twisting of the fiber. Consequently, linear x- or y-polarized radiation from the probe will typically become elliptically polarized upon transmission through the fiber. To project these elliptical polarizations back onto the x- and y-orientations above the sample, we employ the quarter- and half-wave plate sketched in Fig. 2.4a. Specifically, after the fiber we use the quarter-wave plate ($\lambda/4$) to project the elliptically polarized light back onto linear polarized light (as sketched in Fig. 2.4b). Then, the second half-wave plate ($\lambda/2_{(2)}$) rotates the light such that x- and y-polarized radiation from the probe contributes to L_x and L_y, respectively.

To ensure that the heterodyne gain affects the sensitivity of both detection channels equally, the intensity in the reference branch needs to be balanced over both detectors. However, the $\lambda/2_{(2)}$ and $\lambda/4$ rotate the signal from the reference branch that also passes through a different stretch of fiber than the signal branch (see Fig. 2.4). Consequently, we need to tune the polarization of the reference branch without affecting the signal branch polarization state. Hence, to ensure that both detectors receive an equal

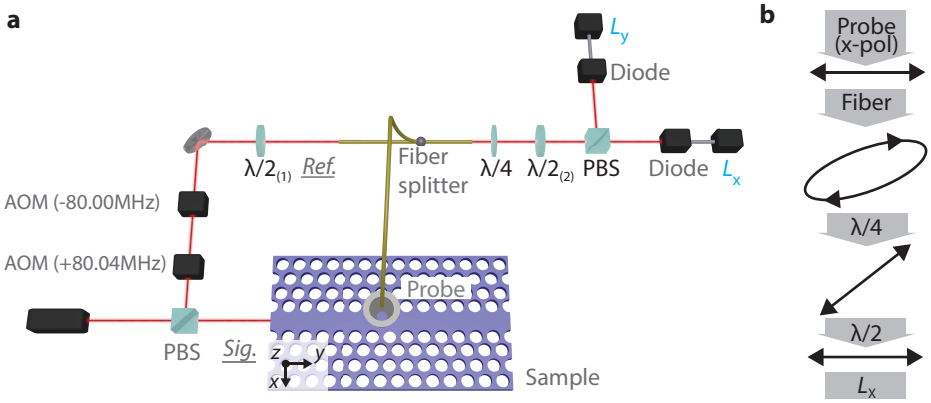

Figure 2.4: A polarization-sensitive NSOM. a This setup is an extension of the setup presented in Fig. 2.3. This extension adds polarization sensitivity by means of the elements marked with black letters. The elements that were present also in the phase-sensitive NSOM are marked in gray. In blue we indicate the two signals L_x and L_y. **b** Sketch of the evolution of the polarization state of light that is horizontally polarized in the sample plane. Upon propagation through the tip the light will in general become elliptically polarized, after which $\lambda/4$ projects the light back onto a linearly polarized state, and finally $\lambda/2_{(2)}$ projects the light back onto the desired basis. If the wave plates project light radiated with a horizontal polarization by the probe back onto a horizontal polarization before the detectors, light from a vertical polarization is also projected back onto its initial state.

heterodyne gain, we use $\lambda/2_{(1)}$ to balance the intensity of the reference branch over the detectors.

2.2.3 Fourier filtering of phase- and polarization-resolved data

In Fig. 2.5a we present an example of a phase- and polarization-resolved measurement. We observe that the spatial dependence of the amplitude of L_x and L_y is drastically different. For example, the amplitude of L_x, shows a maximum along the center of the waveguide (along $x = 0$), whereas along this line the amplitude of L_y is minimal. Furthermore, the phase maps reveal that the fields above the PhCW, which contribute to L_x and L_y, have a distinctly different symmetry. That is, the phase of L_y shows that the minimum along $x = 0$ is accompanied by a π phase jump across $x = 0$. Such a phase jump is indicative of the measurement of an odd-symmetric

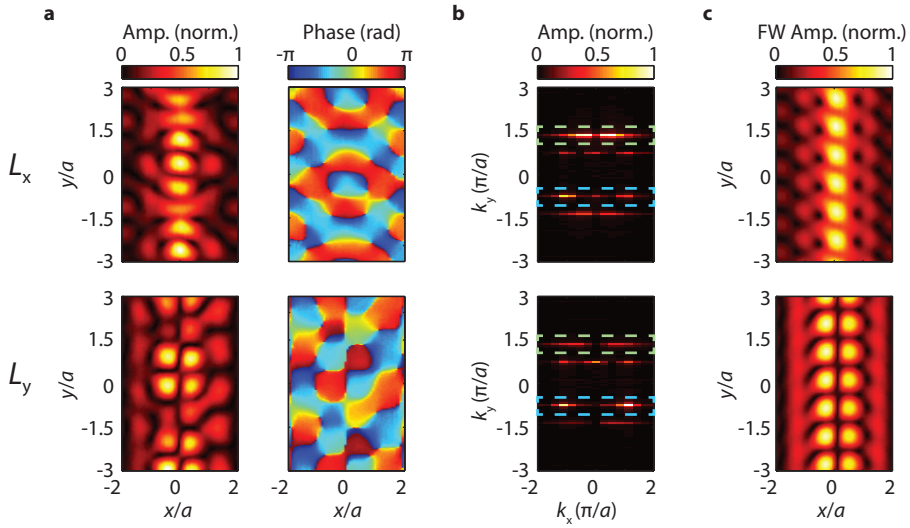

Figure 2.5: Fourier filtering a phase- and polarization-resolved measurement. **a** Fields maps show the amplitude and phase of L_x and L_y. **b** Spatial Fourier transforms of L_x and L_y. The Fourier transform amplitude is normalized. Blue and green dashed boxes are drawn around the $m = -1$ and $m = 0$ harmonics of the forwards propagating Bloch mode, respectively. The color coding of the dashed boxes matches that used in Fig. 1.4. **c** Fourier filtered amplitude of the forwards (FW) propagating Bloch mode. The top (and bottom) row of panels in **a**, **b** and **c** show L_x (and L_y). Measurements were performed near the same crystal as that used in chapters 4 and 5.

field above the PhCW. Conversely, the phase of L_x is even-symmetric across the waveguide center. In chapter 3 and 6 we use these symmetry properties to unravel our near-field measurements (ultimately separating the signals from two field components measured on one lock-in detector in chapter 3).

Another interesting feature of the field maps presented in Fig. 2.5a, b is that, although Bloch's theorem dictates that the amplitude of the PhCW mode should follow the crystal's lattice periodicity, the amplitude maps exhibit larger features. To gain more insight into the origin of this spatial modulation, we present result of the Fourier transformation of the signal from both detectors in Fig. 2.5b. This Fourier transform contains four distinct peaks, which correspond to the $m = -1$ and $m = 0$ Bloch harmonics of a forwards (towards increasing y, and dashed lines in Fig. 2.5b)

and a backwards propagating Bloch mode, which is commonly accepted to arise due to reflections of the PhCW end facet [67]. Furthermore, a closer inspection of the Fourier transforms reveals that, as is required for a Bloch wave, the peaks of the $m = -1$ and $m = 0$ Bloch harmonics are separated by $2\pi/a$.

Please note that, these measurements also show that the lateral spatial frequency content along x differs between the Bloch harmonics. This behavior of the Fourier transforms was also reported by Gersen *et al.* [68], and is associated with the real-space structure of the Bloch wave along x.

To obtain the spatial maps of the forwards traveling mode, we filter the Fourier transform of the signal, keeping the forwards traveling harmonics. By transforming back to real space we obtain the maps shown in Fig. 2.5c [67]. Importantly, these maps, which exhibit the same mirror symmetry properties as those in Fig. 2.5a, now obey the periodicity imposed by Eq. 1.5. In this section, we have not related L_x and L_y to specific field components. In chapters 4 and 5 we investigate this relation between the signal and the optical near fields, and in chapter 6 we investigate the properties of the vector fields that contribute to L_x and L_y in more detail.

2.3 Scattering properties of a subwavelength hole

Ideally, the signal measured with a NSOM can be related to specific optical field components near a nanophotonic structure. Due to the similarity between a subwavelength hole and the aperture of an aperture probe apex, subwavelength holes are widely used to model the optical response of a near-field probe [69, 70, 71, 72]. Theoretical investigations such as [69, 71], advanced our understanding of which field components are measured with a NSOM probe, and provided insight into how much light a NSOM is likely to transmit. Importantly, the fields emitted by a probe have been shown experimentally to resemble those calculated below a hole [72]. This similarity suggests that a subwavelength hole could be used as a model system to predict which field components are converted to radiation by an aperture probe. In this section we therefore investigate the scattering of light by a subwavelength hole that we illuminate with surface plasmon polaritons (SPPs).

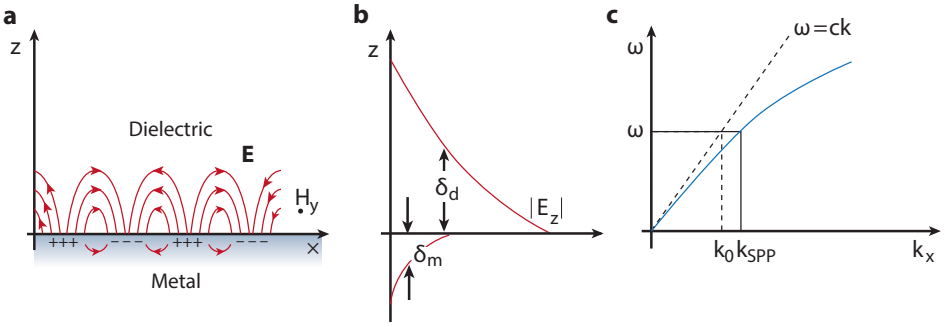

Figure 2.6: Surface plasmon polaritons. a Sketch of the charges density oscillations and the electromagnetic fields associated with a SPP. Charge density oscillations are indicated by the plus and minus signs in the metal. The electric field orientation is indicated with red lines and arrows, and orientation of the transverse magnetic field is indicated with a black dot. **b** Decay of the out of plane electric field amplitude of a SPP into the dielectric and into the metal. Typically the decay length into the dielectric (δ_d) is of the order of half a wavelength, whereas the decay length into the metal (δ_m) is typically of the order of a few tens of nanometers. **c** SPP dispersion relation (blue continuous line). At all wavelengths the SPP modes require a larger momentum than is available in air (dashed black line). Images **a**-**c** are taken from [73].

2.3.1 Surface plasmon polaritons

SPPs are guided optical waves on a metal dielectric interface that have a combined electromagnetic and surface charge character (see Fig. 2.6a). SPPs decay both into and away from the dielectric metal interface. That is, because of screening in the metal, the field intensity of a SPP decays evanescently into the metal (see Fig. 2.6b), and due to the guided character of the wave it decays into the dielectric.

Along its propagation direction, the wavevector of a SPP is given by [73]

$$k_{SPP} = \frac{\omega}{c}\sqrt{\frac{\epsilon_d \epsilon_m}{\epsilon_d + \epsilon_m}}. \tag{2.3}$$

The wavevector of a SPP has two important characteristics. Firstly, because the permittivity of metal has a large negative imaginary part, k_{SPP} has a large imaginary part and SPPs decay along their propagation direction. Secondly, because $|\mathrm{Re}\{\epsilon_m\}| > 1$, $\mathrm{Re}\{k_{SPP}\}$ is greater than the

maximal wavevector of light in the dielectric (see Fig. 2.6c). Therefore, without a mechanism that provides additional momentum, light from free space cannot couple to a SPP mode.

2.3.2 Electric and magnetic polarizability of a subwavelength hole

To study the interaction between SPPs and a subwavelength hole, we use a gold film in which we fabricate a hole by focused ion beam milling. We use a unidirectional grating coupler [74], to provide the required momentum discussed in the previous subsection, and launch a SPP beam towards the hole (see Fig. 2.7a). Using our NSOM we form an image of the fields above the sample, which are detected with x- (see Fig. 2.7b) and y-polarization (see Fig. 2.7c). In both images we observe a beamlike feature centered about $y = 0$. Interestingly, in Fig. 2.7b the beam appears as a single, bright strip, and in Fig. 2.7c it becomes a double strip. Additionally, in both images we see parabolic fringes whose periodicity suggests that they arise due to interference between the incident SPP beam and SPP scattered of the hole.

In fact, the features that we observe in these images can be understood in terms of the incident and scattered waves associated with the hole-SPP interaction. We relate the beamlike feature observed in both images to the incident SPPs. That is, the relatively large signal polarized along the SPP propagation direction (see Fig. 2.7b) can be straightforwardly understood due to the longitudinal nature of (plane) SPP waves. However, because the incident beam has a Gaussian distribution, and is not a plane wave, we also observe a beamlike feature with transverse fields, albeit with a smaller amplitude (see Fig. 2.7c). Notably, this transversely oriented part of the beam changes sign at the beam center, thus producing the observed double strip structure. The fringes can be understood to arise from the interference of the incident SPP wave and the wave scattered by the hole.

Intuitively, the scattering of SPPs from subwavelength holes can be understood as a three-step process: (1) An incident SPP beam propagates towards a hole. (2) The incident SPP wave interacts with the hole. (3) SPP waves are radiated from the hole by the dipoles induced by the interaction. The second step is of particular interest, since it encapsulates the interaction of the electromagnetic field with the nanoscopic structure, our hole. Because of the small dimensions of the hole, the radiation of this scattering event can be described by (electric and magnetic) dipoles,

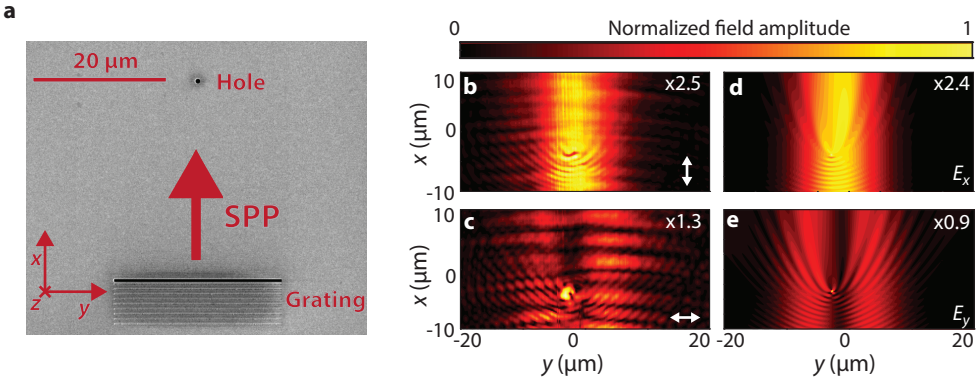

Figure 2.7: Surface plasmon scattering by a sub-wavelength hole. **a** Scanning electron microscope image of the golf film with a grating and a hole etched in it. A SPP beam is launched from the grating coupler to the hole. Axis orientation is shown in the bottom left, scale bar in the top left. **b** (and **c**) measured fields polarized along x(and y) respectively. **d** (and **e**) fitted electric fields along x (and y) respectively.

which couple to the available SPP mode on the gold film [75]. As we show below, to quantify this interaction we must first accurately model both the incident ($\mathbf{E}_{in}$, $\mathbf{H}_{in}$) and scattered ($\mathbf{E}_s$, $\mathbf{H}_s$) fields that correspond to steps (1) and (3).

The three components of the incident Gaussian SPP beam above the film can be written as a Fourier sum of plane waves

$$E_x^{in}(\mathbf{r}) = -C\frac{w_{SPP}}{k_0 k_{SPP}} e^{iw_{SPP}z} \sum_{k_x,k_y} k_x e^{-(\alpha^{2/2})} e^{i(k_x x + k_y y)}, \tag{2.4a}$$

$$E_y^{in}(\mathbf{r}) = -C\frac{w_{SPP}}{k_0 k_{SPP}} e^{iw_{SPP}z} \sum_{k_x,k_y} k_x e^{-(\alpha^{2/2})} e^{i(k_x x + k_y y)}, \tag{2.4b}$$

$$E_z^{in}(\mathbf{r}) = C\frac{k_{spp}}{k_0} e^{iw_{SPP}z} \sum_{k_x,k_y} e^{-(\alpha^{2/2})} e^{i(k_x x + k_y y)}, \tag{2.4c}$$

where the limits of summation, which reflect the explicit separation of the in-plane wave vector into its components, are $k_y \in [-k_0, k_0]$ and $k_{SPP}^2 = k_x^2 + k_y^2$. In these equations $w_{SPP} = -k_0/\sqrt{\epsilon_{gold}+1}$ is the out-of-plane SPP wavevector. We take the complex dielectric permittivity of gold at 1550 nm to be $\epsilon_{gold} = -115 + 11i$. [76]. Lastly, in Eqs. 2.4a-2.4c C and α determine

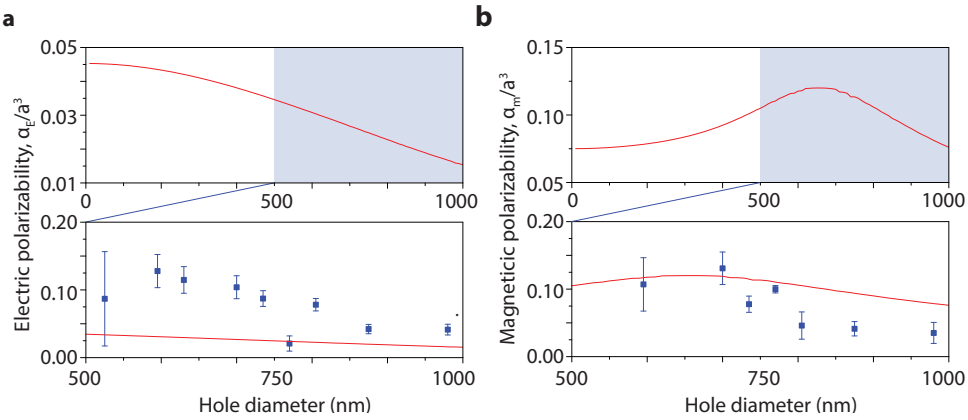

Figure 2.8: Single hole electric and magnetic polarizability. Electric (**a**) and magnetic (**b**) polarizabilities of a single hole as a function of hole diameter. The top panels of **a** and **b** show the calculated polarizabilities, the bottom panels show both calculated (curve) and measured (points) values.

the amplitude and width of the incident SPP beam. The corresponding magnetic field $\mathbf{H}_{in}$ can be calculated from Eq. 2.4a-2.4c using Faraday's law (Eq. 1.1a).

We can write an analytic expression for the SPPs radiated by the hole dipoles [75]. As shown in earlier work [75], for plasmonic scattering this radiation is dominated by an out-of-plane electric dipole p_z and an in-plane magnetic dipole m_y, and hence it can be written as

$$\mathbf{E}^s = -2\pi i \rho^O e^{iw_{SPP}z}\left[k_0^2 k_{SPP} H_1^{(1)}(k_{SPP}r)\cos\phi m_y + ik_0 k_{SPP}^2 H_0^{(1)}(k_{SPP}r)\right] p_z\left(\hat{\mathbf{r}} - \frac{k_{SPP}}{w_{SPP}}\hat{\mathbf{z}}\right), \tag{2.5}$$

where $\rho_O = \epsilon/\left((1+\epsilon)^{1.5}(1-\epsilon)\right)$. In this equation, $H_m^{(1)}$ are Hankel functions, $r = (x-x_0)^2 + (y-y_0)^2$ is the displacement from the hole position at (x_0, y_0) and $\hat{\mathbf{r}} = (\cos\phi\hat{\mathbf{x}}, \sin\phi\hat{\mathbf{y}})$. The total field of the scattering event, which includes both the incident and scattered SPPs, can then be written as $\mathbf{E}_{in} + \mathbf{E}_S$ [75].

Using Eqs. 2.4a-2.5, with $C, \alpha_E, \alpha_M, (x_0, y_0)$, and the dipole strengths $\alpha_E = p_z/E_{z,0}^{in}$ and $\alpha_M = m_y/H_{y,0}^{in}$ as fitting parameters, produces the

results shown in Fig. 2.7b-e. Importantly, α_E and α_M describe the strength of the response of the hole to the incident light. In Fig. 2.8a and b we show a comparison of the experimentally determined α_E and α_M with theoretical values as a function of the hole diameter, where both quantities have been normalized to the cube of the hole radius, a. The uncertainty in the fitting of the exact hole position both limits our ability to determine the exact phase of the polarizabilities and introduces the main source of error in our analysis. The error bars in Fig. 2.8a and b represent the standard deviation in the spread of polarizabilities that we obtain by varying the hole position in a 300 nm diameter circle around (x_0, y_0), while keeping the total scattered energy the same as for the original fit. We observe good qualitative agreement between the calculated and measured α_E and α_M, and very good quantitative agreement for the latter.

2.3.3 Conclusions

In summary, we used a combination of phase- and polarization-sensitive near-field microscopy and electromagnetic theory to unravel the electric and magnetic polarizabilities of single subwavelength holes in optically thick gold films. This allowed us to quantify the dipolar electromagnetic response of holes to surface waves, and in particular to demonstrate that the magnetic contribution should not be neglected, even for nanoscale geometries where the magnetic permeability of each constituent is always near unity. In fact, we show that for holes the magnetic response is often stronger than the electric.

The similarity between the geometries of a subwavelength hole in a metal film and the apex of an aperture type NSOM probe, suggests that a conventional NSOM aperture probe may also have both an electric and a magnetic response. Note that only in-plane oriented dipoles can radiate from the tip apex to the fiber that leads to the detectors [71]. Modeling aperture probe sensitivity requires an excellent understanding of its signal. In chapter 4 we perform the measurements required for such an understanding, which we underpin in chapter 5 with a model based on the optical reciprocity theorem.

3

Modal symmetries at the nanoscale: toward a complete vectorial mapping

In this chapter we use the symmetry properties of electric and magnetic nanoscale optical vector fields to understand and unravel near-field measurements. We ultimately show that we can spatially map three distinct fields using only two detectors. As an example, we create two-dimensional field maps of the out-of-plane magnetic field and two in-plane fields for a silicon nitride ridge waveguide. Furthermore, we are able to identify and remove polarization mixing of less than $1/30$ *of our experimental signals. Since symmetries are ubiquitous in nanophotonic structures and their near fields, our method can impact many future near-field measurements.*

3.1 Introduction

Most structures, be they naturally occurring crystals or artificial nanophotonic objects, possess some degree of symmetry. In fact, we often rely on these symmetries to predict the flow of light about these structures. For example, structural symmetries are essential to the elegance of Mie scattering

theory [77], or to the existence of photonic bandgaps [78] (and Sec. 1.3.3). Surprisingly, with few notable exceptions [63, 79], the prevalent symmetries of nanophotonic structures have not been exploited in the analysis of near-field optical measurements.

Due to the tight confinement of light in nanophotonic structures, in the vicinity of these structures typically all six components of the optical near field - the three electric and the three magnetic - are nonzero (see chapter 1). However, polarization-resolved near-field scanning optical microscopy, be it in collection [70, 67, 80] or scattering [64, 81, 62, 82] mode, allows for the simultaneous detection of only two orthogonally polarized channels (see chapter 2). Based on our investigation of the scattering of a subwavelength hole (see Sec. 2.3.2), each of those two channels could measure a signal from both the electric and magnetic optical near field. Specifically, as we demonstrate in chapters 4 and 5, the two channels could be used to detect four field components, with each channel detecting signal from both an in-plane electric and an in-plane magnetic field component. Although in this optimal case only two electromagnetic (EM) fields would be missing, the separation of the signals into maps of the individual EM components is far from trivial. In fact, to date such a separation has not been demonstrated.

As is often the case, the underlying symmetry of the photonic structures constrains their near fields, and can therefore help unravel near-field measurements. For example, on planes of symmetry, such as the center of a waveguide or nanoantenna, certain near-field components are identically zero. For the nanoantenna, a careful measurement of two nonzero field components was sufficient to create full EM field maps on the symmetry plane [63]. Likewise, measuring along the center of a ridge waveguide allowed for direct observations of the out-of-plane magnetic field using a split-ring probe (SRP) [79]. These examples, however, are limited to a single plane, whereas the constraints imposed by symmetry apply over all space.

In this chapter we demonstrate how knowledge of the symmetry of the structure and its associated fields can be used to unravel aperture NSOM measurements and create comprehensive two-dimensional near-field maps. We begin by showing how, for a benchmark photonic structure such as a ridge waveguide, we can use symmetry considerations to identify and correct for polarization mixing as small as 1/30 of our signals. Furthermore, we show that when we use a SRP to measure on this structure, we can unravel

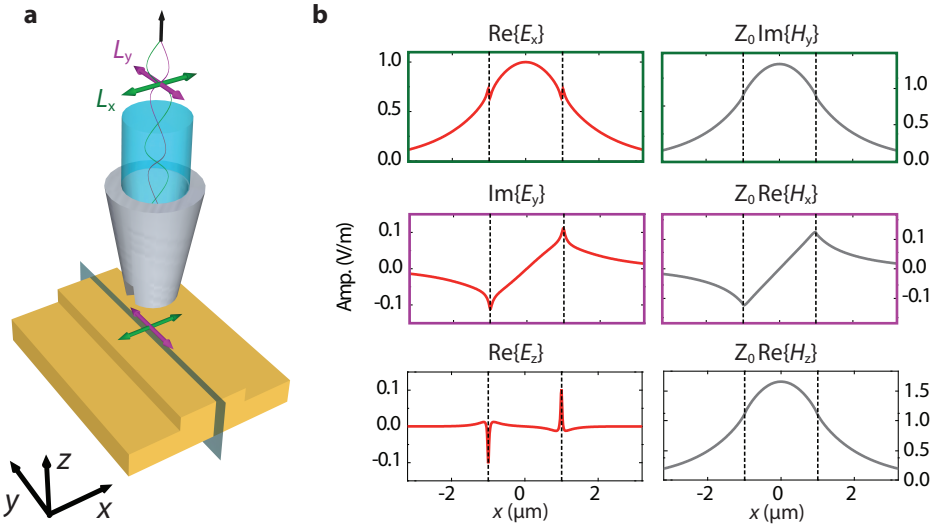

Figure 3.1: Experimental setup. **a** A sketch of the sample and the tip of the SRP used in this work. The fiber forms the core of the tip. The green and purple arrows near the sample indicate electric fields along x and y, respectively. The probe converts these fields to radiation polarized along x and y, indicated by the top purple and green arrows. The polarization-resolved detection of this radiation results in the signals L_x and L_y. The semi-transparent black plane denotes the mirror symmetry of the waveguide (yz-plane). **b** Calculated field profiles 20 nm above the structure. To indicate to which detection channel the far-field radiation from these fields contributes, the borders of the plot windows are color coded to match the colors of field orientations shown in **a**. The magnetic fields are multiplied by the free space impedance Z_0 and the amplitude of all fields is normalized to the maximum of E_x. The dashed black lines indicate the edges of the ridge.

our measurements and create two-dimensional maps of three contributions to the signals on two detectors.

3.2 Sample and experimental setup

To test our methodology we measure on a benchmark photonic structure. Specifically, we use a 20 nm high, 2 µm wide Si_4N_4 ridge waveguide that is mirror symmetric about the yz-plane (see Fig. 3.1a). Using a commer-

cial full wave solver (COMSOL), we find that at a free space wavelength of 1550 nm this structure supports a single TE mode ($n_{\text{eff}} = 1.65$). In Fig. 3.1b we show a snapshot in time of the calculated electric and magnetic components of the fields associated with the TE mode. We choose the point in time where E_x is completely real. At this instant all components are either completely real or completely imaginary. Around the center of the waveguide, E_x, H_y and H_z have an even symmetry, whereas E_y, H_x and E_z have an odd symmetry [33]. Note that the field profiles of both the even E_x and H_y and the odd E_y and H_x are very similar. The similarity between the in-plane electric and magnetic fields is further underlined by the observation that the ratio of the amplitude of E_x to E_y is close to the ratio of H_y to H_x.

These near fields can be converted to far-field radiation with a near-field probe that is in close proximity of the sample. We ensure x- and y- oriented electric near fields radiate to electric far fields polarized along x and y (inset to Fig. 3.1a) [79], resulting in the signals L_x and L_y, respectively. However, the conventional aperture probe converts both the in-plane electric *and*, as we will later show in chapter 4, the in-plane magnetic near fields to far-field radiation. This radiation from H_y (H_x) has its electric field along x (y) and will be detected on the same detector as E_x (E_y).

3.3 Polarization mixing removal

Before turning to the SRP, we apply the field symmetry constraints to unravel the data collected with a conventional aperture probe (see Fig. 2.1). An example of such a measurement is shown in Fig. 3.2, where in the top panels of part a and b we present the 2D maps corresponding to the real part of the complex signals L_x and L_y, respectively. For the situation depicted in this figure we can write

$$L_x = \alpha_x E_x + \beta_x Z_0 H_y \approx \alpha'_x E_x, \tag{3.1a}$$

$$L_y = \alpha_y E_y + \beta_y Z_0 H_x \approx \alpha'_y E_y, \tag{3.1b}$$

where the complex parameters α and β quantify the sensitivity to experimental electric and magnetic fields. We multiply the magnetic fields by the free space impedance Z_0, because we detect the electric field associated with this magnetic field. Further, because both the amplitude and profile of the calculated E_x (E_y) and H_y (H_x) are very similar (see Fig. 3.1b) and

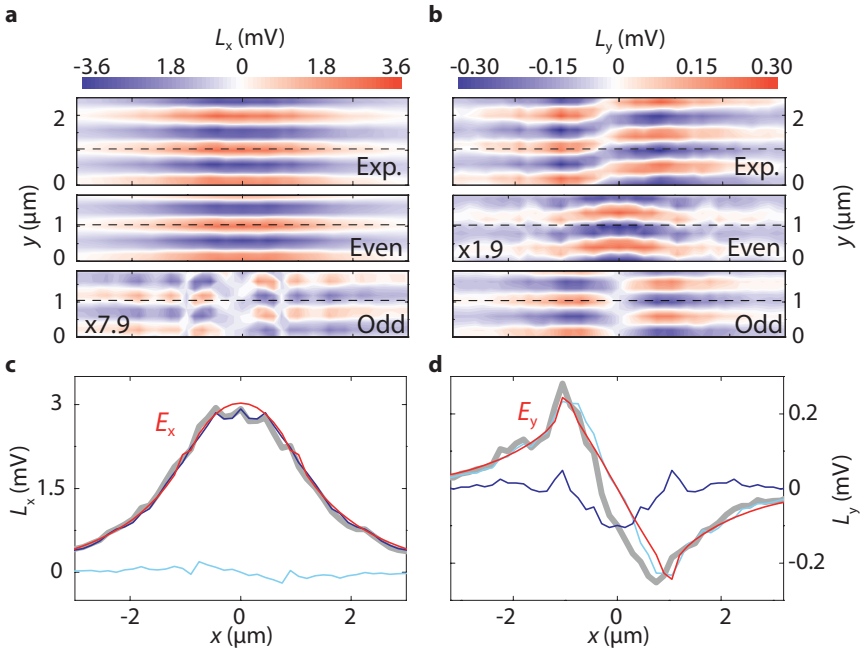

Figure 3.2: Symmetric aperture probe measurements. **a** and **b** (Top panels) 2D maps of the real part of L_x and L_y, respectively. (Middle and Bottom panels) 2D maps of the real part of the signals in L_x and L_y with even (Middle) and odd (Bottom) symmetry, respectively. In **a** and **b** the dashed black lines indicate the position of the line traces shown in **c** and **d**, the multiplication factors refer to scaling of the color map. **c** and **d** Line traces of the signal in L_x, **c**, and L_y, **d**, together with the even (dark blue lines) and odd (light blue lines) symmetry components, and together with the fitted calculated in plane electric fields (red lines).

their ratio is constant in the measurement plane. That is, $Z_0 H_{y,x}/E_{x,y} = p$ and in Eq. 3.1b we use $\alpha'_{x,y} = \alpha_{x,y} + p\beta_{x,y}$ to express the signals in terms of $E_{x,y}$ alone.

The experimental field maps shown in the top panels of Fig. 3.2a and b suggest that indeed an aperture probe largely collects the signals predicted by Eq. 3.1b. Not only does L_x appear to have an even symmetry, and L_y odd, but the amplitude of the measured L_x is also an order of magnitude larger than L_y, as is predicted by the calculations (see Fig. 3.1b). However, a closer inspection of L_y (top panel of Fig. 3.2b) reveals an unexpected

oddity: the line of minimal amplitude of this signal is shifted by 0.3 µm from the center of the waveguide. This suggests that L_y not only contains a component with odd, but also a component with even symmetry. We therefore separate the signals according to their symmetries, by computing the signals with even symmetry $L_{\mathrm{even}}(x, y)$, and odd symmetry, $L_{\mathrm{odd}}(x, y)$, as follows:

$$L_{\mathrm{even}}(x, y) = \frac{L(x, y) + L_{\mathrm{mir}}(x, y)}{2}, \tag{3.2a}$$

$$L_{\mathrm{odd}}(x, y) = \frac{L(x, y) - L_{\mathrm{mir}}(x, y)}{2}, \tag{3.2b}$$

where $L_{\mathrm{mir}}(x, y) = L(x_c - x, y)$ indicates the signal mirrored around the center x_c of the waveguide. We find x_c to within 250 nm by fitting a cosine to the central region of L_x. This number is governed both the low confinement of the model waveguide used and the quality of the data. With increasing confinement this number will decrease. This separation approach is justified because $|E_x| >> |E_y|$. Hence, any appreciable shift of L_x due to mixing between the two channels would result in L_y being dominated by a component with even symmetry, which is clearly not the case.

In the bottom panels of Fig. 3.2a and b we show the field maps with even and odd symmetry constructed with Eq. 3.2b. We find that as expected in L_x, the even-symmetric component is much larger than its odd-symmetric component. Furthermore, we observe that the minimum of the odd-symmetric signal in L_y is now on the center of the waveguide, and the field distribution shape seems to match E_y (see Fig. 3.1b). However, the even component of L_y that has a comparable distribution to E_x and H_y(see Fig. 3.1b), suggests the presence of some signal of those field components.

To gain more insight in our measurements, we inspect line traces (at a constant y) along the maxima of the signals with even and odd symmetry. As the 2D maps suggested, the L_x is mainly even, with a negligible odd component. We attribute the signal with even symmetry in L_y to contributions of E_x and H_y to the signal in this channel. The presence of signal due to H_y or E_x in L_y, could be caused by mixing of the polarizations in the probe, the fiber or the detection path. We can place an upper bound on the amount of mixing by comparing the amplitude of the signal with even symmetry in L_x to that in L_y. From this comparison, we estimate that we detect $\sim 1/30$ of the signal from E_x and H_y in L_y (1/900 in intensity). Strikingly even such a small amount of mixing can distort L_y and, importantly, using Eq. 3.2b we can filter out this mixing.

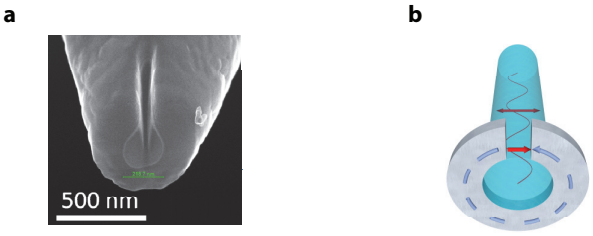

Figure 3.3: Split ring near-field probe geometry and physics. **a** Scanning electron microscope images of the split ring probe used in this work. The diameter split ring probe is 218 nm. The slit of the split ring probe is around 62 nm wide and 335 nm high. **b** Sketch of the physics through which a SRP converts H_z into radiation. The blue dashed and the red arrow on the split ring depicts the current along the split ring and the direction of electric field associated with the charge build up. The out of plane magnetic field is converted into radiation into the fiber with a polarization along the red arrow.

Having shown how we can use symmetry considerations to identify the polarization mixing in our measurements, we now quantify the sensitivities of our system. In specific we use $\alpha'_{x,y}$ (Eq. 3.1b) to fit the calculated in-plane electric fields to our measurements. From these fits we find that the relative sensitivity to the in-plane electric fields $|\alpha'_x|/|\alpha'_y| = 1.1 \pm 0.2 \pm 0.1$. Here, the first error indicates the range over which $\alpha'_{x,y}$ can vary before the sum of squares of the residual of the fit increases by a factor 2, and the second error follows from the 250 nm uncertainty in x_c. A comparison of the measurements to the magnetic field instead results in the same sensitivity ratio ($|\beta'_y|/|\beta'_x| = 1.2 \pm 0.2 \pm 0.3$). The difference in sensitivities could be explained by, for example, a slightly ovally shaped probe, a more sensitive detector in the x branch, or a slender tilt of the probe with respect to the sample.

3.4 Separation of detected field components

Because the signal with even symmetry in L_y is smaller than the other signals and we understand its origin, we can use this channel to map an additional component of the near field. Hence, we now turn to the SRP measurements, where in addition to the in-plane electromagnetic components we also expect to detect signal from the out-of-plane component of

the magnetic field. We sketch the physics through which a SRP converts H_z into radiation towards the detectors in Fig. 3.3b. In analogue to a split-ring resonator [20, 83] the gap in the SRP stops the currents induced by H_z from flowing around the ring. This process can be interpreted as the creation of an electrical dipole oriented across the gap. This dipole can radiate to the detectors, with a polarization that is oriented across the gap. In this section, we orient the SRP such that the slit is parallel to x (as sketched in Fig. 3.1a) and light from H_z will therefore contribute to L_y [79].

We confirm the detection of H_z by analyzing the amplitude of the standing wave pattern that results from a reflection of the end facet of the structure (inset of Fig. 3.4c). Because E_x and H_y do not experience a phase flip upon reflection, whereas H_z does, the standing wave of H_z is offset by a quarter wavelength compared to the standing wave of E_x and H_y. In our measurements (inset of Fig. 3.4c) we observe this shift, and accordingly detect H_z with L_y [79].

Having confirmed the detection of H_z, we now write the signals we expect to measure with the SRP as follows:

$$L_x \approx \alpha'_x E_x, \tag{3.3a}$$

$$L_y \approx \alpha'_y E_y + \gamma_y Z_0 H_z, \tag{3.3b}$$

where we use γ_y to quantify the sensitivity to the out-of-plane magnetic field.

We present the field maps measured with the SRP in the top panels of Fig. 3.4a and b. It is immediately evident that these 2D maps differ greatly from those measured with an aperture probe (see Fig. 3.2). Where with the aperture probe L_y largely had an odd symmetry, we now mainly observe an even symmetry L_y. Because we expect that the in-plane fields with odd symmetry still contribute to L_y, we again separate fields with even and odd symmetry in the signal from the two detectors. We show the resulting 2D maps in the middle and bottom panels of Fig. 3.4a and b. In contrast to the measurements with an aperture probe (see Fig. 3.2), these maps show that the dominant component of both L_x and L_y now has an even symmetry. At the same time, and in agreement with the measurements shown in Fig. 3.2, we only find a clear odd symmetry signal in L_y. That is, the symmetries of our measured near fields allow us to resolve three signals using only two detectors.

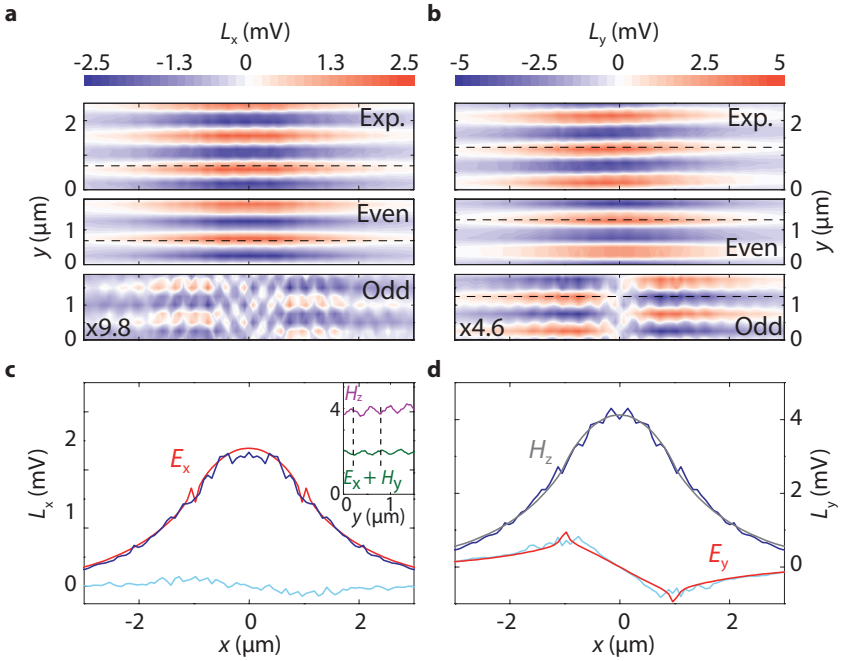

Figure 3.4: Split probe measurements. **a** and **b** 2D maps of the the real part of L_x and L_y (Top panels). (Middle and Bottom panels) 2D maps of the real part of the signals in L_x and L_y with even (Middle) and odd (Bottom) symmetry. The scaling of the bottom maps in **a** and **b** is indicated in the figures. **c** and **d** Line traces of the even (dark blue lines) and odd symmetry (light blue lines) components of L_x and L_y, together with the fitted calculated in-plane electric fields (red lines). In **c** the inset shows line traces of the amplitude of L_x (green) and L_y (purple) along $x = 0$. In **d** the dark gray line indicates H_z fitted to the signal in L_y with even symmetry.

These findings are confirmed by the line traces of the separated signals that are depicted in Fig. 3.4c and d. In these figure panels we observe that the even symmetry component of L_x and both the even- and odd-symmetric components of L_y are in good agreement with the calculated distributions for E_x, H_z and E_y, respectively. By fitting these fields to the measurements, we find for the SRP that $|\alpha'_x|/|\alpha'_y| = 0.23 \pm 0.08 \pm 0.07$ and $|\alpha'_x|/|\gamma'_y| = 0.94 \pm 0.50 \pm 0.05$. That is, the sensitivity to H_z is roughly equal to that of the superposition of E_x and H_y. Furthermore, the SRP is also relatively more sensitive to E_y than the aperture probe. We explain

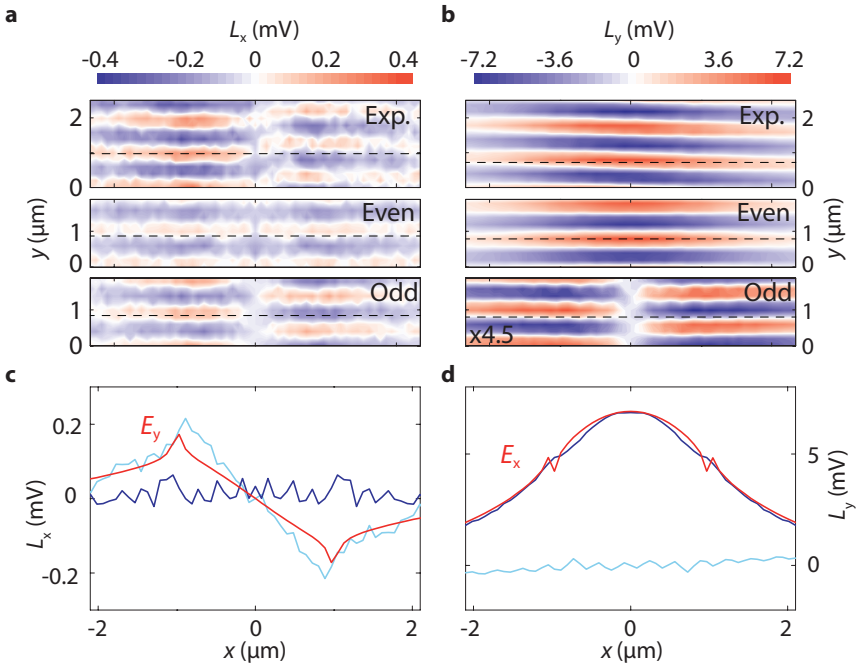

Figure 3.5: Measurements with a SRP on the vertical section of the waveguide. **a** and **b** 2D maps of the real part of L_x and L_y (Top panels). (Middle and Bottom panels) 2D maps of the real part of the signals in L_x and L_y with even (Middle) and odd (Bottom) symmetry. The scaling of the bottom map in **b** is indicated in the figures. **c** and **d** Line traces of the even- (dark blue lines) and odd-symmetric (light blue lines) components of L_x and L_y, together with the fitted calculated in-plane electric fields (red lines).

the increased sensitivity by the slit that forms the gap in the SRP, because for y-polarized illumination there may exist an available mode in the slit, whereas for x-polarized illumination there is no available mode [84].

To ensure that we have correctly identified the components measured with a SRP, we now change the orientation of the slit with respect to the waveguide. The waveguide that we use has both a horizontal- (on which we measured the data shown in Fig. 3.2 and 3.4) and a vertical section, connected by a gentle 90° bend. By measuring with the SRP above the vertical section of the waveguide, while keeping the orientation of the probe fixed, we can effectively rotate the slit 90° to the previous measurements.

On the center of the vertical section of the waveguide, where the slit is parallel to the waveguide, we expect that L_x contains signal from E_y and H_x, and that L_y contains a superposition of the signal from E_x, H_y and H_z.

In the top panels of Fig. 3.5a and b we present the 2D field maps measured with slit in the SRP oriented parallel to the waveguide. These field maps greatly differ from those measured with the slit oriented perpendicular to the waveguide (see Fig. 3.4). We find that L_y is dominated by an even-symmetric component, and that L_x clearly contains signal from a odd-symmetric field. These measurements suggest that we write the signals we expect to measure with the slit in the SRP oriented parallel to the waveguide as follows:

$$L_x \approx r\alpha'_x E_y, \tag{3.4a}$$

$$L_y \approx r(\alpha'_y E_x + \gamma_y Z_0 H_z) \approx c\alpha''_y E_x, \tag{3.4b}$$

where r quantifies the change of the field amplitude in the waveguide with respect to those reported in Eq. 3.3b. The fields E_x, E_y and H_z indicate the fields shown in Fig. 3.1, and the parameters α'_y and α'_x correspond to those used in Eq. 3.3b. Furthermore, because $Z_0 H_z/E_x \approx p_1$ (see Fig. 3.1), we use $\alpha''_y = \alpha'_y + p_1\gamma_y$, to express L_y in terms of E_x alone.

To compare the signals predicted in Eq. 3.4b to the measurements, we again separate the components with even and odd symmetry (middle and bottom panels of Fig. 3.5a and b). The profile of the odd-symmetric component in L_x suggests that it contains signal from E_y and H_x, and, the large even-symmetric component in L_y further confirms the detection of E_x, H_y and H_z. Furthermore, because there is little correspondence between the profile of E_x and the even-symmetric component of L_y, we expect that there is very little mixing. Specifically, we find that the amplitude of the even-symmetric component in L_y is 61 times larger amplitude than that of the even-symmetric component in L_x that does not follow the same profile. This means that the mixing in the system is smaller than 1/60, hence it is even smaller than for the normal probe. The presence of the small odd-symmetric component in L_y could be explained by a not perfectly 90° angle of the vertical section of the waveguide with respect to the orientation of the horizontal section.

3.5 Conclusions

In this chapter we showed how symmetry can be used to identify and separate different electromagnetic field components in NSOM signals. By separating these fields, we opened up a new detection channel that allowed us to measure three near-field signals on only two detectors. That is, we mapped the out-of-plane magnetic field and two signals of the in-plane fields in two dimensions. In the future, we aim to extend this method, so that it can be used to measure all six components of the electromagnetic field. Because field component that we do not use to explain our signal is E_z, which in our study has odd symmetry, we aim to design a probe that in addition converts this last component to radiation on L_x. Such a probe, combined with the approach demonstrated in this chapter, would make the detection of complete nanoscale vector fields feasible. Lastly, the symmetries of the ridge waveguide are generally present in nanophotonic structures. Since measurement of the phase of the near-field signal is the only requirement enable the use symmetry for separating fields, we believe that our method will benefit different NSOM schemes, and experiments for a wide range of nanophotonic structures.

4

Simultaneous measurement of nanoscale electric and magnetic optical fields

In this chapter we demonstrate the simultaneous detection of both electric and magnetic fields with a nanoscale resolution. Specifically, we demonstrate a direct mapping of all in-plane electromagnetic near fields with a conventional, symmetric aperture probe, which had traditionally been assumed to detect either the electric fields or only the in-plane magnetic field. Exploiting the 3D evolution of the evanescent Bloch harmonics above a photonic crystal waveguide, we show that the ratio of the efficiencies with which the magnetic field and the electric field are collected is between 0.3 and 2.5.

4.1 Introduction

For over 20 years near-field scanning optical microscopy has improved our understanding of the flow and behavior of light in and around nanophotonic structures [56]. Although the interaction of light with nanoscopic structures typically involves all six components of the electromagnetic near field, maps of two components of the local optical electric fields have been sufficient

to clarify and uncover exciting phenomena such as control of surface plasmon polaritons [74, 85], field enhancements near nano-antennas [62, 81], and polarization singularities [67]. The recent advent of metamaterials has sparked research of nanophotonic structures that couple strongly to the magnetic field of light [86, 87, 88], with the potential to cloak objects [89], show giant nonlinear optical activity [90] or exhibit a negative refractive index [91]. In response to these developments, techniques have been developed to measure the nanoscale magnetic field [70, 92, 93, 94]. However, metamaterials interacts with both not only with the magnetic but also the electric field of light. Consequently, a measurement of the complete nanoscale electromagnetic field vector is a powerful way to drive advances in the field of metamaterials further, and to elucidate the interplay between optical behavior and geometry that underpins these phenomena.

An ideal measurement would allow for the simultaneous mapping of both electric and magnetic fields in and around nanophotonic structures. In principle, using Maxwell's equations it is possible to derive the full electromagnetic field vector if 3 of its components are known (in both amplitude and phase) in a 3D space with sufficient accuracy for the derivatives to be taken. However, while such an approach is at the heart of many numerical simulations, the experimental equivalent has not been demonstrated at the nanoscale where typically all components are present. That is, to date, no more than two-field components have been simultaneously measured [62, 63, 81, 67]. Consequently Maxwell's equations can only be exploited on certain planes of symmetry [63] and not in general.

Here, we demonstrate a direct mapping of all in-plane electromagnetic near fields with a conventional, symmetric aperture probe (see Fig. 4.1a), which had traditionally been assumed to detect either the electric fields [67] or only the in-plane magnetic field [70, 69]. Specifically, we show that the ratio of the efficiencies with which the magnetic field and the electric field are collected is between 0.3 and 2.5.

4.2 Experimental

We image the evanescent fields above a PhCW using a homebuilt-, polarization-sensitive NSOM (see chapter 2). This is an ideal structure for studying near-field detection, as the electromagnetic field distribution of its modes is well understood, while not being trivial [33]. In this chapter we use a

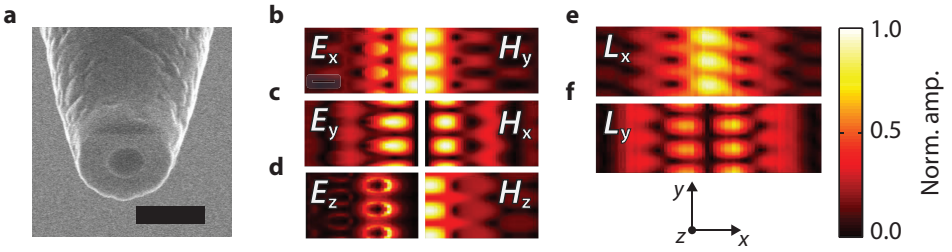

Figure 4.1: Near-field measurements of a PhCW. a, SEM image of the apex of the 218 nm aperture probe used in this work. The black scale bar indicates 500 nm. **b-d**, Calculations of the transverse fields. Left: the electric field along x, y and z, respectively. Right: the magnetic fields along y, x and z, respectively. **e**, **f**, Measurements taken 20 nm above the sample on L_x (**e**) and L_y (**f**). Panels **b-f** all show amplitudes, and are scaled to their respective maxima. Axis orientation is show below **f**. All panels are 3 by 3 unit cells, and for clarity they are stretched in the x-direction (by a factor 1.7).

PhCW, formed by perforating a 220 nm thin silicon slab with a hexagonal lattice of 120 nm radius holes. One row of missing holes acts as a waveguide for the 1570 nm TE polarized light. A 2D field map is created by raster scanning an aperture probe in the xy-plane above the nanophotonic structure (see chapter 2). We ensure that all light resulting from an x-oriented electric field above the PhCW, E_x, is collected by detector L_x, and likewise E_y is detected by L_y. Any light that might arise from an x-oriented magnetic field, H_x, would be detected by L_y, and that H_y would be picked up by L_x (see chapter 2 and 3).

4.3 Aperture probe sensitivity to $\mathbf{E}_{\parallel}$ and $\mathbf{H}_{\parallel}$

The 3D structure of the PhCW allows us to use measurements at increasing heights above the crystal, h, to differentiate between $\mathbf{E}_{\parallel}$ and $\mathbf{H}_{\parallel}$. In the xy-plane of symmetry, inside the silicon membrane, only TE components (E_x, E_y, H_z) of the electromagnetic field are non-zero. However, away from this symmetry plane all six components can be found [38]. Further, these profiles have an intricate subwavelength structure, as reflected by our calculations of the fields 20 nm above the waveguide (Figs. 4.1b-d), which assists in the identification of the different field components. The corresponding

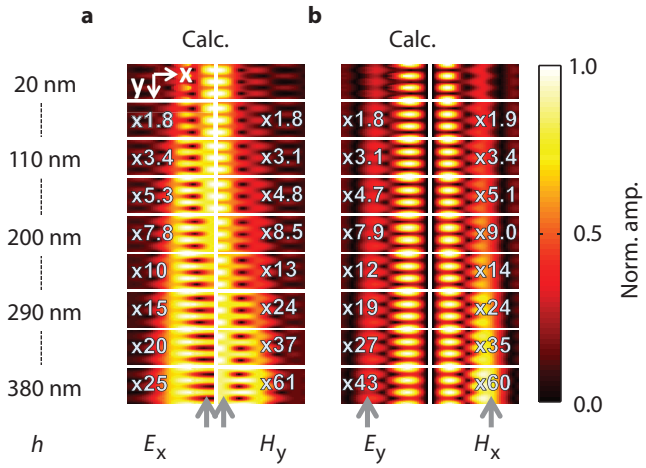

Figure 4.2: Calculations of the in-plane fields in the xy-plane at height *h* above the surface. **a**, **b**, Calculations of the evanescent field above the crystal. In **a** the left column of panels shows E_x left of symmetry plane and the right column shows H_y right of symmetry plane. In **b** the left and right columns show in-plane field profiles of E_y and H_x respectively. All plots show amplitudes of the calculated or measured signals. The color in all plots is scaled to the maximum, the scaling relative to the ground plane is indicated by the multiplication factors. All panels are 3 by 3 unit cells, and for clarity they are stretched in the x-direction (by a factor 1.7); the axis orientation is show in the top E_x panel.

measurements (Figs. 4.1e-f) for L_x and L_y, are in excellent agreement with the calculated, in-plane components of the mode[a] (Figs. 4.1c-d). This data not only shows the good polarization separation of our system, but it also highlights that the fields mapped at the surface of the PhCW could equally be E_x and E_y [67] or H_y and H_x.

However, as h increases, not only do the relative amplitudes of the electric and magnetic fields change, but so do their spatial profiles. This divergence of the different field profiles occurs because a given mode is composed of a superposition of many Bloch harmonics, each of which decays differently in z (see Sec. 1.3.2) [42]. And, because **E** and **H** are related through their spatial derivatives (see Eq. 1.1), each field profile shows a

[a]We show half the field profile of each mode, because the symmetry of the waveguide enforces mirror symmetry in x of the field amplitude of the mode.

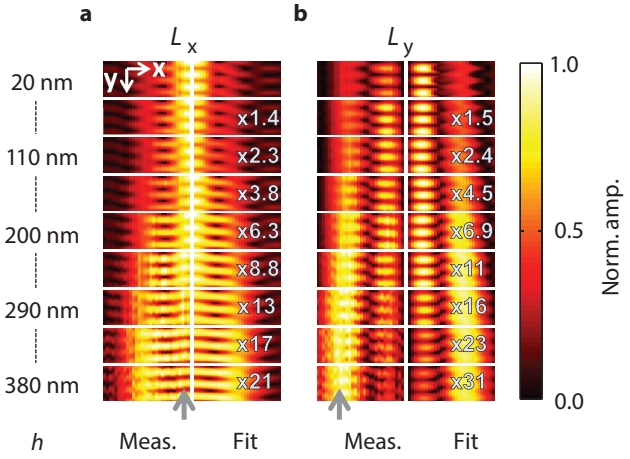

Figure 4.3: Measurements and fitted calculations in the xy-plane at height *h* above the surface. **a**, Left: fields measured on L_x. Right: fitted calculations. **b**, Left: fields measured on L_y. Right: fitted calculations. All plots show amplitudes of the calculated or measured signals. The color in all plots is scaled to the maximum, the scaling relative to the ground plane is indicated by the multiplication factors. All panels are 3 by 3 unit cells, and for clarity they are stretched in the x-direction (by a factor 1.7); the axis orientation is show in the top L_x panel.

different height dependence. This is reflected by Fig. 4.2a and b that depict the calculated amplitudes of E_x (and H_y) and E_y (and H_x), respectively, for different values of h. Notably, for $h > 250$ nm E_x has minima along the center of the waveguide, where H_y has maxima (arrows, Fig. 4.2a). In addition, at these large heights, the amplitude at the side of the waveguide of H_x is clearly larger than that of E_y (arrows, Fig. 4.2b).

When scanning our NSOM probe at heights $h > 20$ nm, we can no longer use our force feedback system to control the probe sample distance. Thus, we switch to a quadrant-cell based height feedback loop. In this mode of operation we compare the position of the probe as measured with the quadrant cell, when it scans the surface of the sample. Because we now no longer feedback on the probe-sample distance directly, these measurements could be affected by drift between the probe and the sample. We correct for this possible drift by matching the decay of the field above the photonic crystal to the decay of calculated fields, by scaling the height at which we

compute the data. We find less than 10 nm/hr drift for the measurements presented in this chapter, corresponding to a maximal total drift of typically 5% and maximally 15% of the total height above the surface.

The left panels of Fig. 4.3a and b depict how the measured field patterns evolve with height. Surprisingly, we observe that as the height increases the measurements correspond to neither the calculated $\mathbf{E}_\parallel$ nor $\mathbf{H}_\parallel$ profiles. For L_x we observe a minimum along the center of the waveguide that is reminiscent of E_x (arrow, Fig. 4.3a). In contrast, for L_y we observe the enhanced side lobes expected for H_x. Yet the response at the center of the waveguide appears suppressed (arrow, Fig. 4.3b). These observations suggest that we measure a superposition of $\mathbf{E}_\parallel$ and $\mathbf{H}_\parallel$. By fitting the amplitude of the superposition of the two calculated complex fields to our data

$$L_x(\mathbf{r}) = \alpha_x E_x(\mathbf{r}) + \beta_x H_y(\mathbf{r}), \tag{4.1a}$$

$$L_y(\mathbf{r}) = \alpha_y E_y(\mathbf{r}) + \beta_y H_x(\mathbf{r}), \tag{4.1b}$$

where $\mathbf{r} = (x, y)$ represents the position at which we measure the fields, we find $\alpha_{x,y}$ and $\beta_{x,y}$ that are complex scalars that quantify the sensitivity of our system to the electric and magnetic in-plane fields, respectively. To minimize the number of fitting parameters, we avoid fitting the phase of the Bloch wave, by fitting the amplitude of the calculations to the amplitude of the measurements. We choose our unit system such that the electric and magnetic fields are in the same units, and hence if $|\alpha| = |\beta|$, the probe is equally sensitive to the electric and the magnetic fields.

4.4 Effect of probe diameter on sensitivity to $\mathbf{E}_\parallel$ and $\mathbf{H}_\parallel$

The right panels of Figs. 4.3a and b depict fits to measurements obtained at different heights for each detector. For all heights we find that the fit of the in-plane fields excellently reproduces all the features in the data. Importantly, we use only the four complex fit parameters, $\alpha_{x,y}$ and $\beta_{x,y}$, to fit all 9 heights ranging from 20 to 380 nm simultaneously. For this particular probe, with a 218 nm diameter, we find that $|\beta_x|/|\alpha_x| = 0.5(2)$ and that $|\beta_y|/|\alpha_y| = 0.9(3)$, our results for the relative phase the signal from the electric and magnetic fields were at this point inconclusive. These values of $|\beta|/|\alpha|$indicate that we detect roughly equal amounts of the electric and magnetic near fields. In stark contrast to previous work that assumed that

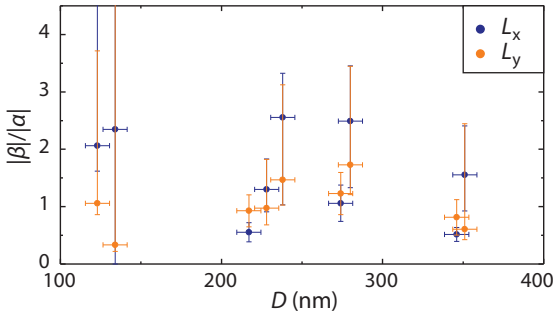

Figure 4.4: Probe size dependent sensitivities. For probe diameters D from 120 nm to 350 nm we present $|\beta|/|\alpha|$ for both detectors.

either the electric [67] or the magnetic [70, 95] fields are detected, we show that we simultaneously detect nanoscale electric and the magnetic fields.

Therefore we investigate the sensitivity to $\mathbf{E}_{\parallel}$ and $\mathbf{H}_{\parallel}$ of probes with different diameters. Figure 4.4 depicts a plot of the relative sensitivity ($|\beta|/|\alpha|$) for the two detectors L_x and L_y. We identify the height drift (10% of the height), the uncertainty of the xy-position (30 nm in each direction) and our exact location on the calculated dispersion relation of the photonic crystal waveguide as sources of error in our estimation of $|\beta_{x,y}|/|\alpha_{x,y}|$, for each probe. We then sweep through this 4 parameter space, and for each permutation use the fitting procedure outlined in Sec. 4.3 to find a value for α and β. In this manner we obtain a spread of $|\beta_{x,y}|/|\alpha_{x,y}|$ values whose standard deviation is shown as the (vertical) error bars for these ratios (see Fig. 4.4). Possible errors in our estimation of the probe diameter, tilt in probe orientation and fabrication imperfections, effectively change the diameter of the probe. This uncertainty is reflected in the (horizontal) error bars for D (see Fig. 4.4). This figure shows that probes of all diameters detect both $\mathbf{E}_{\parallel}$ and $\mathbf{H}_{\parallel}$. Strikingly, we find that to within error bars all probes detect roughly equal amounts of signal from the electric and magnetic fields.

4.5 Conclusions

In conclusion, we have demonstrated the simultaneous detection of the electric and magnetic optical fields at the nanoscale. We show that a symmetric aperture probe measures all 4 in-plane components of the electromagnetic

field at once. The superposition of electric and magnetic fields that we detect can be extended to a full vectorial map using Maxwell's relations in combination with additional constraints; these can be provided by the symmetry properties of the sample, or, alternatively, by measurements with different probes. These auxiliary measurements could be performed with a split-ring probe that is known to measure H_z (see chapter 3), or a scattering type NSOM that detects E_z [81]. Concurrently, this work paves the way for studies of fundamental processes such as, for example, of a molecule undergoing a magnetic dipole transition [92].

5

Predicting aperture probe sensitivity to $\mathbf{E}_{\|}$ and $\mathbf{H}_{\|}$

We demonstrate that the optical reciprocity theorem can be used to excellently predict the field maps measured with an aperture probe above a photonic crystal waveguide (shown in chapter 4 and 6). We show that the ratios of the signal from the electric and magnetic fields in these predicted measurements matches the experimentally observed ratios for a wide range of probe diameters. As an outlook, we present a method, based on the optical reciprocity theorem, that could be used to separate the signal from the electric and magnetic near fields.

5.1 Introduction

Challenging calculations of the optical properties of nanophotonic structures can often be aided by exploiting the boundary conditions on a system. In this context, the optical reciprocity theorem is a particularly powerful tool for solving diffraction problems [96]. These problems typically require knowledge of the fields of a source on a detector ($\mathbf{P}$) in the presence of a scattering object, for example an aperture (S) in an opaque film (S_1),

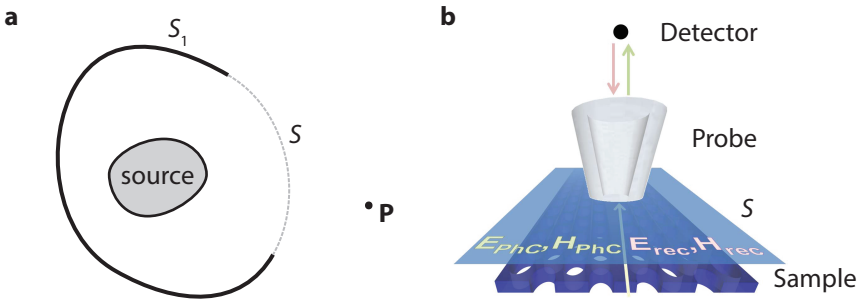

Figure 5.1: Schematic of the fields involved in the optical reciprocity theorem. The dark blue drawings represent the PhCW, with the probe above it sketched in gray. The red arrow and red text indicate the reciprocal fields that arise from a dipole ($\mathbf{j}_{rec}$) placed at the detectors. Green (and red) arrows and text indicate the experimental (and reciprocal) fields, respectively. $\mathbf{E}_{PhC,rec}$ and $\mathbf{H}_{PhC,rec}$ represent the fields on the surface S (sketched in transparent blue) between the crystal and the probe.

as sketched in Fig. 5.1a. A direct analytic expression for the fields of the source on $\mathbf{P}$ can only be obtained in specific cases. However, the fields of the source on S can usually be deduced more straightforwardly. Furthermore, in the reciprocal situation (formed by interchanging source and detector), the fields on S from a source at $\mathbf{P}$ can typically also be calculated with relative ease [96, 97]. In essence, this last step removes the difference between the source and the detector, and the quantity of interest becomes the coupling between these two points. Their mutual impedance (coupling strength) can be found via an overlap integral over the fields on S in both situations (reciprocal and 'experimental') [96, 98, 97]. In this chapter we describe how the optical reciprocity theorem can be applied to the process of image formation with a NSOM. We show that without any assumptions the reciprocity theorem provides a means of describing the measured field in terms of the in-plane fields alone. Furthermore, by approximating our probe as a subwavelength hole, we show how we use the reciprocity theorem to predict the signal measured with an aperture type NSOM. We compare this signal to the experimental signal. Furthermore, we decompose the signal into its electric and magnetic contributions, in this manner we extract a theoretical electric to magnetic sensitivity ratios, which we can compare to those reported in chapter 4.

5.2 Reciprocity theorem applied to near-field microscopy

The possibility of using the optical reciprocity theorem to explain near-field data was first suggested in [98]. Figure 5.1b shows a schematic of the fields and sources that affect the signal measured by the system. In this figure $\mathbf{E}_{PhC}$ and $\mathbf{H}_{PhC}$ are the calculated electromagnetic fields associated with light propagating in the PhCW. The interaction of these fields with the probe sets up the fields that we measure at the detector ($\mathbf{E}_{det}$). The reciprocal situation is formed by placing a dipole source ($\mathbf{j}_{rec}$) at the detector. This dipole emits the fields $\mathbf{E}_{rec}$ and $\mathbf{H}_{rec}$ (see Fig. 5.1b). In this framework the sensitivity of the system is given by how well $\mathbf{E}_{PhC}$ and $\mathbf{H}_{PhC}$ can induce fields ($\mathbf{E}_{det}$) that drive a dipole placed at the detector ($\mathbf{j}_{rec}$). This sensitivity is commonly referred to as the mutual impedance ($\mathbf{E}_{det} \cdot \mathbf{j}_{rec}$). The mutual impedance is determined by the overlap integral between the experimental and reciprocal fields on a plane (S) between the sample and the detector [97].

Mathematically the mutual impedance of our system can be expressed as [97]:

$$\begin{aligned} \mathbf{E}_{det}(\mathbf{r}_{tip}) \cdot \mathbf{j}_{rec} = \int_S & \left(\mathbf{E}_{PhC}(\mathbf{r}, \mathbf{r}_{tip}) \times \mathbf{H}_{rec}(\mathbf{r}, \mathbf{r}_{tip}) - \right. \\ & \left. \mathbf{E}_{rec}(\mathbf{r}, \mathbf{r}_{tip}) \times \mathbf{H}_{PhC}(\mathbf{r}, \mathbf{r}_{tip})\right) \cdot \mathbf{dS}, \end{aligned} \tag{5.1}$$

where $\mathbf{r}$ is the position on the surface S, $\mathbf{r}_{tip}$ is the position of the probe and $\mathbf{dS}$ is the normal vector of S. As long as the interaction between the probe and the sample is sufficiently weak, we can neglect the effect of the tip on the fields above the photonic crystal. This allows us to omit $\mathbf{r}_{tip}$ in $\mathbf{E}_{PhC,r_{tip}}$ and $\mathbf{H}_{PhC,r_{tip}}$ on the right hand side of Eq. 5.1.

Interestingly, from Eq. 5.1, we immediately see that the reciprocal magnetic fields give an idea of the sensitivity to the experimental electric fields and vice versa. A natural choice of S is the xy-plane at a height between the tip and the PhCW. Hence, due to the dot product with $\mathbf{dS}$, which is oriented along $\hat{\mathbf{z}}$, and the cross products in the integral, only the in-plane of the reciprocal and photonic crystal fields contribute to the mutual impedance. Because near nanophotonic structures typically all components of the optical field are present (see Sec. 1.2), this observation suggests that we indeed measure the in-plane components of $\mathbf{E}$ and $\mathbf{H}$.

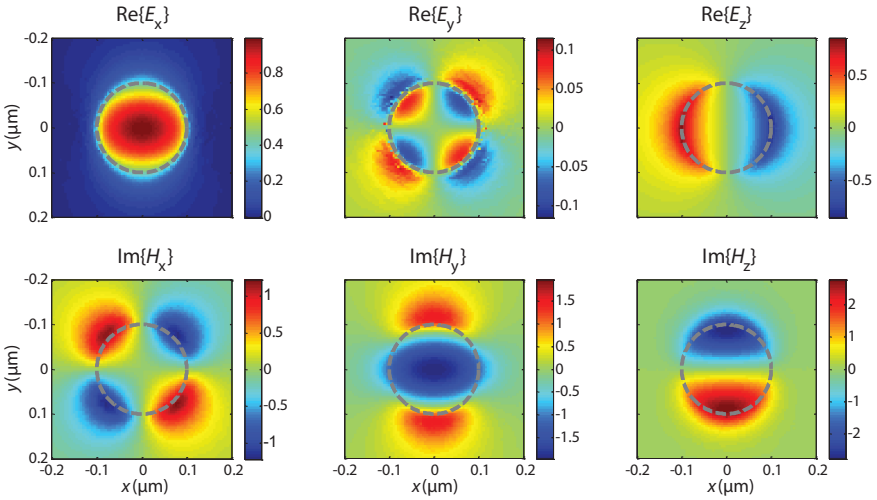

Figure 5.2: Simulated optical fields below to a subwavelength aperture. All components of the electromagnetic field 10 nm below a glass hole (D = 200 nm) in a 300 nm thick Al film. The gray dashed lines indicate a cross-section of the probe aperture.

It is worth noting that Eq. 5.1 can be rewritten solely in terms of either $\mathbf{E}_{rec}$ or $\mathbf{H}_{rec}$, although in these cases one must use the derivatives of these fields [97]. While this might seem contradictory - how could only $\mathbf{E}$ or only $\mathbf{H}$ be measured at the same time by the same probe? - it is actually expected. After all, Maxwell's equations tell us that $\mathbf{H}$ can be expressed in terms of the derivatives of $\mathbf{E}$, and vice versa. Consequently, we are free to choose the form of the reciprocity theorem that yields the most physical insight concerning our experiments. Hence, we use the form that allows us to determine the fields and not their derivatives.

To better understand the experimentally obtained signals from the fields above the crystal, we calculate the reciprocal fields on the surface S. Specifically, we consider the fields below an aperture probe with a varying diameter, computed with the commercially available FEM package COMSOL. We simplify the calculations by exploiting the similarity of the near fields below a hole in a metal film to the fields below the probe [72]. To find the sensitivity of $L_x(= \mathbf{E}_{det} \cdot \mathbf{j}_x)$, we simulate the fields below a glass hole in a 300 nm thick aluminum film that is illuminated by the fields radiated by an x-oriented electric dipole that is placed at a distance of 3 μm directly

above the hole. To find the sensitivity of $L_y(= \mathbf{E}_{det} \cdot \mathbf{j}_y)$, we use a y-oriented dipole. We choose the surface S 10 nm below the probe, which is approximately in the middle between the probe and the sample when scanning the surface of the PhCW.

In Fig. 5.2 we depict the real part of the fields below a hole with a radius of 100 nm, resulting from the illumination with a $\mathbf{j}_x$ dipole oscillating at a frequency $\omega = 2\pi c/1570$ nm. These fields determine the sensitivity of L_x. Based on Eq. 5.1, we expect that the magnetic contribution to the signal on L_x will be dominated by $H_{y,PhC}$, because the amplitude of $E_{x,rec}$ is much larger than that of $E_{y,rec}$. Further, the mapping of $H_{y,phc}$ to L_x will be slightly blurred because of the Gaussian profile of $E_{x,rec}$.

The detection of the in-plane electric field is less straightforward to understand, because the in-plane reciprocal magnetic fields have both comparable amplitudes and not Gaussian distributions. However, because the size of our probe is sub-wavelength, we can to first order interpret the sensitivity in terms of a sum over the fields. Based on these sums we expect to measure a blurred image of $E_{x,PhC}$ as well, because we find that the sum over center lobe of $H_{y,rec}$ is stronger than the sum over the side lobes. Conversely, because the sum over $H_{x,rec}$ is negligible, we expect not to detect $E_{y,PhC}$ on L_x. Similarly, we now qualitatively understand that L_y detects $E_{y,PhC}$ and $H_{x,PhC}$.

The prediction of the measured fields requires the numerical evaluation of Eq. 5.1. In combination with the calculated reciprocal fields, inserting the fields near a sample into Eq. 5.1, allows us to compute a predicted signal. Here, we use the calculated fields [38] above the same PhCW as in chapters 4 and 6. We calculate $\mathbf{E}_{det}(\mathbf{r}_{tip}) \cdot \mathbf{j}_{rec}$ for an x and a y oriented dipole over the same range of positions as used in these chapters.

Strikingly, Figs. 5.3a and b reveal that the predicted signals, without using any fitting parameters, closely match the experimental signals 300 nm above the PhCW (note that we use the same fields as chapter 4). Furthermore, at all heights, ranging from 20 - 400 nm (not shown), we find that the fields calculated via this approach neatly match the measured field patterns.

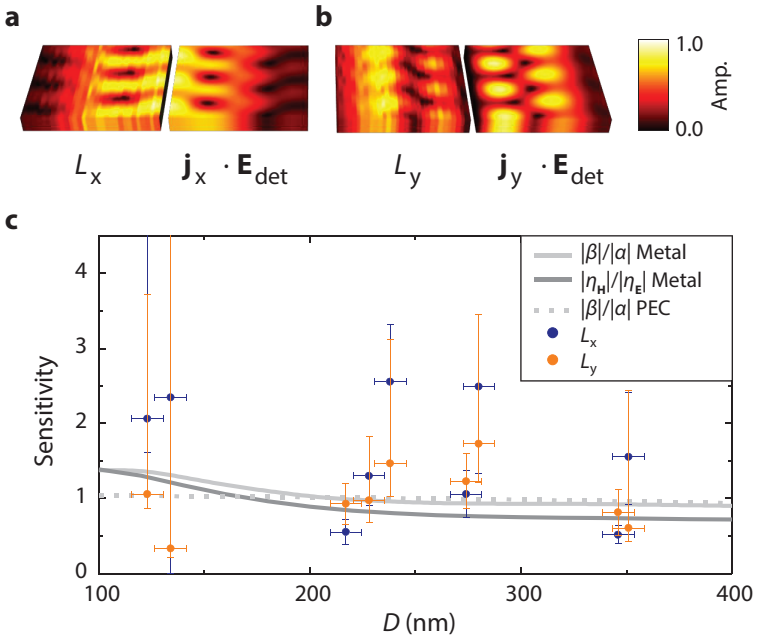

Figure 5.3: Sensitivity to electric and magnetic fields versus probe diameter. **a, b** The right panels of **a** and **b** show the predictions, and the left panels show the measured fields 300 nm above the PhCW on L_x and L_y, respectively. **c** The light gray line and dots show the $|\beta|/|\alpha|$ ratio from the numerically calculated fields and analytical BB fields, respectively. The dark gray line shows the corresponding electric to magnetic sensitivity calculated using the numerically calculated fields. The blue and orange dots show the magnetic to electric ratio obtained from the fits on L_x and L_y, respectively, as reported in chapter 4.

5.3 Relative sensitivity to $\mathbf{E}_{\|}$ and $\mathbf{H}_{\|}$

The knowledge of these predicted signals enables the extraction of a theoretical value of $|\beta|/|\alpha|$. To this end, we compare the amplitude of the signal from the $\mathbf{E}_{\|}$ and $\mathbf{H}_{\|}$ that we expect to measure above the PhCW used in this work. We express the sensitivity to $\mathbf{E}_{\|}$ and $\mathbf{H}_{\|}$ in terms of all components involved in the mutual impedance:

$$\begin{aligned}\eta_{\mathbf{E}}(h) &= \sum_{i=x,y} \int \frac{1}{A_{\mathbf{E}}} \Big| \int_S \big(H^i_{x,rec}(\mathbf{r}_{tip}, \mathbf{r}, R) E^i_{y,PhC}(\mathbf{r}, h) - \\ &\quad H^i_{y,rec}(\mathbf{r}_{tip}, \mathbf{r}, R) E^i_{x,PhC}(\mathbf{r}, h) \big)\, dS \Big|\, dU, \end{aligned} \tag{5.2}$$

and

$$\begin{aligned}\eta_{\mathbf{H}}(h) &= \sum_{i=x,y} \int \frac{1}{A_{\mathbf{H}}} \Big| \int_S \big(E^i_{x,rec}(\mathbf{r}_{tip}, \mathbf{r}, R) H^i_{y,PhC}(\mathbf{r}, h) - \\ &\quad E^i_{y,rec}(\mathbf{r}_{tip}, \mathbf{r}, R) H^i_{x,PhC}(\mathbf{r}, h) \big)\, dS \Big|\, dU, \end{aligned} \tag{5.3}$$

where $\eta_{\mathbf{H}}(h)$ and $\eta_{\mathbf{E}}(h)$ are the sensitivities to the magnetic and electric fields at heights h, respectively, $A_{\mathbf{E}}$ and $A_{\mathbf{H}}$ indicate the amplitudes of the in-plane fields, and U is the area defined by the intersection of a PhCW unit cell with the surface S. To find $\eta_E(h)$ we compute the expected signal from $\mathbf{E}_{PhC}$ normalized to the amplitude of $\mathbf{E}_{PhC}$, we integrate that signal over U, and lastly we average the sensitivity over the two detectors. We find $\eta_{\mathbf{E}}$ from $\eta_{\mathbf{E}}(h)$, by averaging over all heights. We apply an analogue procedure to find $\eta_{\mathbf{H}}(h)$, with the use of Eq. 5.3. We find that the ratio between $\eta_{\mathbf{H}}$and $\eta_{\mathbf{E}}$, which describes the relative sensitivity to the electric and magnetic fields, is close to one for a wide range of probe diameters (see Fig. 5.3c).

However, this sensitivity still contains the contribution of $E_{x,PhC}$ ($E_{y,PhC}$) and $H_{y,PhC}$ ($H_{x,PhC}$) to the sensitivity of L_y (L_x) respectively, which is not taken into account in the fitting algorithm used in chapter 4. Hence, we now compute the same integral, while ignoring these contributions, which is directly a calculation of $|\beta|/|\alpha|$. The results of this approach are shown in Fig. 5.3c in light gray. Despite the apparent simplification, the sensitivities that we find are very similar to those of the full calculation. Furthermore, the $|\beta|/|\alpha|$ that we have found in this manner agree very well with the

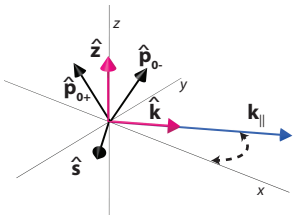

Figure 5.4: Sketch of the coordinate basis used. Black arrows indicate the unit vectors of the coordinate basis used in this section. Purple arrow indicate the unit vector used to construct this basis. The blue arrow indicates the in-plane wavevector of the light.

experimentally observed ratios that we reported in chapter 4 (indicated by the blue and orange dots in Fig. 5.3c).

We can further simplify our model by calculating the sensitivity of the probe using the analytic expressions for the fields below a Bethe-Bouwkamp (BB) aperture [99, 100, 101]. This type of aperture is a highly subwavelength hole in an infinitely thin, perfect electric conductor (PEC). Unlike a real metal, such as the aluminum that coats our probe, a PEC does not support surface modes such as SPPs. Remarkably, despite this further simplification, the sensitivities predicted by the BB aperture are in good agreement with both those calculated using an aperture in an aluminum film, as well as with the measurements (see Fig. 5.3c). This is a further validation of earlier near-field work, where the probe apex has been approximated by a BB aperture [69].

5.4 Outlook

In this section, we describe a method that could extend the application of the optical reciprocity theorem to near-field scanning optical microscopy, such that the signal from the simultaneously detected electric and magnetic fields could be separated. Specifically, this method could allow for the extraction of all optical field components from the near field mapping with a conventional aperture NSOM probe.

Because the two signals (L_x, L_y) that an aperture type NSOM probe measures contain a superposition of four experimental fields (E_x, E_y, H_x, H_y), a separation of these fields requires additional constraints. These constraints could be provided by Maxwell's equations, which relate the

electric and magnetic optical fields. Furthermore, the optical fields that we measure evanescently decay away from the sample under investigation, which must also hold for the separate field components, thereby providing an additional constraint.

To efficiently exploit that the experimental fields must follow Maxwell's equations and that these fields decay away from the nanophotonic structure, it is convenient to change coordinate basis and to work in reciprocal space. To straightforwardly relate the electric and magnetic optical fields, we move to the following coordinate basis, which is defined by the propagation direction of the light

$$\hat{\mathbf{s}} = \hat{\mathbf{k}}_{\parallel} \times \hat{\mathbf{z}}, \tag{5.4a}$$

$$\hat{\mathbf{p}}_{0\pm} = \frac{k_{\parallel}\hat{\mathbf{z}} \mp w_0 \hat{\mathbf{k}}_{\parallel}}{k_0}, \tag{5.4b}$$

$$w_0 = \sqrt{k_0^2 - k_{\parallel}^2}, \tag{5.4c}$$

where $\mathbf{k}_{\parallel}$ is the in-plane wavevector, the subscript 0 indicates quantities defined by the wavevector in air, and $\hat{\mathbf{p}}_{\mathbf{0}\pm}$, and $\hat{\mathbf{s}}$ are the orientations used, respectively, for the polarizations of s- and p-polarized light with respect to the xy-plane [8]. We illustrate the orientation of the vectors in these equation with the sketch presented in Fig. 5.4.

In this coordinate basis, the Fourier transform of the electric field above the PhCW is given by:

$$\begin{aligned}\mathbf{E}_{PhC}(\mathbf{k}_{\parallel}, z) = &\left(\hat{\mathbf{s}} E_{+}^{s}(\mathbf{k}_{\parallel}) + \hat{\mathbf{p}}_{0+} E_{+}^{p}(\mathbf{k}_{\parallel})\right) e^{iw_0 z} + \\ &\left(\hat{\mathbf{s}} E_{-}^{s}(\mathbf{k}_{\parallel}) + \hat{\mathbf{p}}_{0-} E_{-}^{p}(\mathbf{k}_{\parallel})\right) e^{-iw_0 z},\end{aligned} \tag{5.5}$$

Here, the superscripts s and p indicate the component of the electric field. Because the fields above the photonic crystal have to follow Maxwell's equations (Eq. 1.1), we can express the magnetic field in terms of the electric field (in SI-units)

$$\begin{aligned}\mathbf{H}_{PhC}(\mathbf{k}_{\parallel}, z) = &\left(\hat{\mathbf{s}} \frac{E_{+}^{p}(\mathbf{k}_{\parallel})}{Z_0} - \hat{\mathbf{p}}_{0+} \frac{E_{+}^{s}(\mathbf{k}_{\parallel})}{Z_0}\right) e^{iw_0 z} + \\ &\left(\hat{\mathbf{s}} \frac{E_{-}^{p}(\mathbf{k}_{\parallel})}{Z_0} - \hat{\mathbf{p}}_{0-} \frac{E_{-}^{s}(\mathbf{k}_{\parallel})}{Z_0}\right) e^{-iw_0 z}.\end{aligned} \tag{5.6}$$

This expression highlights the power of the coordinate basis used, as we have now expressed the magnetic field in terms of the electric field in a manner that does not require any derivatives. A second simplification in the expression of the electric and magnetic field can be made by realizing that w_0 is purely imaginary and positive, because in Eq. 5.4c both k_0 and $k_{\parallel}$ are purely real and we take the positive square root. Hence, in both Eq. 5.5 and 5.6 the two right terms grow with increasing z, and the two left terms decrease with increasing z. However, we know that we measure only evanescently decaying waves and we can omit the two right terms in Eqs. 5.5 and 5.6.

Turning back to the expression for the measured signal that we found in the main body of the chapter, we can express Eq. 5.1 as follows:

$$c\mu_0 \begin{bmatrix} L(\mathbf{k};x) \\ L(\mathbf{k};y) \end{bmatrix} = N_{\mathbf{k}}^{rec} \begin{bmatrix} \mathbf{E}_{+}^{s}(\mathbf{k},z) \\ \mathbf{E}_{+}^{p}(\mathbf{k},z) \end{bmatrix}, \tag{5.7}$$

where $N_{\mathbf{k}}^{rec}$ is a 2 x 2 matrix containing the reciprocal fields, and $L(\mathbf{k};x,y)$ are the Fourier transforms of the measured fields. Strikingly, this equation contains only two unknowns. Hence, by inverting $N_{\mathbf{k}}^{rec}$ a full vectorial mapping of the electric and magnetic fields above the PhCW can be constructed from our measurements. Obviously, for this approach to be viable, the solution needs to be unique, which is the case if the determinant is not equal to zero. Furthermore, we anticipate that factors such as experimental noise will need to be corrected for.

5.5 Conclusions

The excellent agreement of the magnetic to electric sensitivity ratios calculated using the optical reciprocity theorem and the experimentally observed ratios, which we found in chapter 4 to be close to one, confirms that aperture probes of all investigated radii are sensitive to both $\mathbf{E}_{\parallel}$ and $\mathbf{H}_{\parallel}$. Furthermore, the reciprocal framework not only explains our data, but can also be used for future probe designs that selectively detect certain electromagnetic field components. In this manner, this work provides a route to a full mapping of the electromagnetic fields at the nanoscale. Alternatively a route toward a complete mapping of optical near fields could be provided by the scheme that we proposed in the outlook section.

6

Tracing electric and magnetic optical singularities in 3D space

In this chapter we investigate the topological properties of the structured light fields above a PhCW. We simultaneously map the complex in-plane electric and magnetic fields at different heights above a photonic crystal waveguide. At each height we identify phase- and polarization-singularities. We show that the trajectory traced by each singularity through three dimensional space is distinct, highlighting the complex relationship between the electric and magnetic near fields

6.1 Introduction

By structuring optical far fields researchers have gained control over fundamental physical aspects of light propagation and the way in which light interacts with objects. Airy beams, for example, are non-diffracting, accelerating, and self-healing [102, 103], and can be used as robust optical tweezers to trap and control particles [104]. Structured light can also carry spin- (SAM) or orbital-angular momentum (OAM) [105, 106] and since

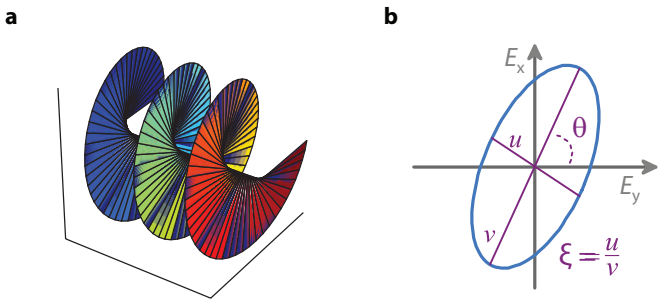

Figure 6.1: Illustration of phase- and polarization-singularities. a Calculated phase front of a vortex beam. The phase front evolves around the beam center, where the phase is undefined and a phase singularity occurs. **b** The polarization ellipse for the in-plane electric field, showing the ellipticity, $\xi = u/v$, and the angle of orientation θ. The blue line indicates the end point of the field vector. At any point in space the field vector traces out an ellipse over time. At a point where the angle of orientation is undefined, which is the case when $|u| = |v|$, light is circularly polarized and a polarization singularity occurs. Panel **a** is adapted from [110].

this momentum can be transferred to, or from, particles [107], such beams are of great interest for quantum optical [108] and biophysical detection applications [109].

In a typical vortex beam, which carries OAM, the optical phase evolves around the center of the beam (see Fig. 6.1a). Because the phase evolves around the beam center, no phase can be assigned to the field at the beam center, and this point is known as a phase singularity. Polarization singularities are points in space where a property that defines the polarization ellipse is undetermined (see Fig. 6.1b). Although the ellipse angle can be undefined on the entire surface created by the crosscut through a circularly polarized plane wave, polarization singularities (C-points), which carry SAM, can only be present when, on a crosscut through the optical field, the interference of multiple plane waves creates points of undefined ellipse angle [111]. Importantly, the effect of OAM or SAM carrying phase- and polarization-singularities on an object (i.e. spinning a particle or driving an angular momentum changing transition) is determined by the object's position relative to the singularity.

There are clear benefits in bringing the structure of light to the nanoscale,

particularly for applications [112], since quantum and biological objects are frequently of this size. Even better, the light can be structured at the nanoscale due to its interaction with nanophotonic structures such as photonic crystals or hole arrays. Not only does this nanophotonic approach open up new routes to electro-optical devices, but it also allows for control over the light fields by using a lithographically-determined geometry. For example, using nanopatterned launchers researchers have created Airy plasmons [102], while the near-field mappings of ridge waveguides and PhCWs have revealed phase- [113] and polarization singularities [67], respectively.

In the aforementioned experiments, however, the near fields were all imaged at the surface of the samples. Yet each of the many evanescent waves that combine to create the optical-field distribution near a nanophotonic structure has a different out-of-plane decay constant (see chapter 1). Consequently, the superposition of these waves results in markedly different light-field distributions at different heights, which can even differ between the electric **E** and magnetic **H** fields, as we demonstrated experimentally in chapter 4. This is in contrast with the far field where, for example, the position of a vortex within a beam does not change as it propagates through space. Conversely, in the near field, theoretical studies have predicted that lateral positions of features such as vortices can be strongly dependent on the height above the surface [114]. Knowledge of the 3D trajectories of specific structure in the near fields of nanophotonic objects is crucial if their light fields are to be used.

In this chapter we report on the 3D spatial evolution of optical singularities in the electromagnetic near fields of a PhCW. Specifically, we experimentally find phase- and polarization-singularities in both the in-plane electric and magnetic near fields, and we show that the singularities in the electric an magnetic fields follow different trajectories through space. Our observations are in excellent agreement with rigorous electromagnetic simulations.

A PhCW is an ideal structure for our investigation. First, this type of waveguide is routinely used to control the flow of light [33], and can be fabricated with extremely high quality and precision. Further, the near-field distributions of these crystals can be readily calculated [38], are finely structured, and are known to contain electric polarization singularities at the surface [67]. In essence, PhCWs support fields with nanoscopic structure, while inherently guiding photons to, and from, these features.

Furthermore, the evolution of the PhCW near fields through 3D space, and hence the fine structure that they contain, can be extremely complex. Consider that, at the plane of symmetry at the center of the silicon slab, and only there, the PhCW mode is purely TE, and only E_x, E_y, and H_z have a nonzero amplitude. Moreover, this mode is highly structured as it is consists of many different Bloch harmonics, each decaying at a different rate [42]; the larger the wavevector of a harmonic, the quicker it decays. So, far away from the surface we are left with a weak, unstructured light field. Conversely, in the near field, we find nonzero amplitudes in all 6 near-field components, and observe that their profiles can greatly vary. Such a metamorphosis of the field distributions cannot be found in far fields, and consequently it is reasonable to expect that the fine structure of these near fields might also evolve in a unique manner.

6.2 Separating $\mathbf{E}_{\parallel}$ and $\mathbf{H}_{\parallel}$

We image the in-plane components of the electromagnetic field near our PhCW using an aperture type home-built polarization- and phase-sensitive NSOM. The signal from our aperture probe contains both the in-plane electric and the magnetic near fields, and we are able to characterize the efficiency with which it picks up both (see chapter 4).

To separate the four in-plane components of $\mathbf{E}_{\parallel}$ and $\mathbf{H}_{\parallel}$, we have to essentially untangle our NSOM measurement that provides two signals both containing a superposition of one electric and one magnetic component. This is not a trivial problem since, as described by Eq. 4.1, we only detect 2 signals, which we label L_x and L_y (which are associated with fields that are, ideally, orthogonally polarized), but those two contain information from 4 fields: E_x, E_y, H_x and E_y. Since in Eq. 4.1 we have four unknowns and only two equations we clearly require another set of equations to find the separate distributions of $\mathbf{E}_{\parallel}$ and $\mathbf{H}_{\parallel}$.

Before we separate the different near-field components from our measurements, however, there are a couple of preliminary steps to our data processing that occur to eliminate unwanted signals (such as, for example, reflections in the waveguide). We begin by filtering our data in k-space to isolate the forwards-propagating mode (see chapter 2). Next, because of a slight polarization mixing in our NSOM, we measure a small part of the L_x signal in the L_y channel (see chapter 3). However, we can exploit

the symmetry of the different field components to separate the two contributions (see chapter 3). That is, we mirror the signal about the center of the PhCW and hence separate the field distributions with odd symmetry (E_x and H_y), from those that we want, which have even symmetry (for example, the presence of E_y and H_x introduced by polarization mixing in the fiber of the probe, or by asymmetries of the probe itself).

Having cleaned up the signal by removing reflections and field components from the other channel we now separate $\mathbf{E}_{\|}$ from $\mathbf{H}_{\|}$. As we noted above, we have four unknowns in Eq. 4.1 and consequently we need two more equations that relate $\mathbf{E}_{\|}$ to $\mathbf{H}_{\|}$ at each position in space. We can empirically recover such a relation from our calculations of the PhCW modes (shown in Fig. 6.2), which we write as

$$H_y(\mathbf{r}) = \gamma_x(\mathbf{r})\, E_x(\mathbf{r}), \tag{6.1a}$$

$$H_x(\mathbf{r}) = \gamma_y(\mathbf{r})\, E_y(\mathbf{r}). \tag{6.1b}$$

Substituting these equations into Eqs. 4.1, allows us to solve for the electric field

$$E_x(\mathbf{r}) = \frac{L_x(\mathbf{r})}{\alpha_x + \beta_x \gamma_x(\mathbf{r})}, \tag{6.2a}$$

$$E_y(\mathbf{r}) = \frac{L_y(\mathbf{r})}{\alpha_y + \beta_y \gamma_y(\mathbf{r})}, \tag{6.2b}$$

where $\alpha_{x,y}$ and $\beta_{x,y}$ are the experimentally determined parameters that characterize the efficiencies of our probe, and $\gamma_{x,y}(\mathbf{r})$ are found from numerical simulation of our structure. Once the electric fields are known, we can use Eqs. 6.1 to solve for the magnetic fields.

Figure 6.2 shows the calculated in-plane fields 110 nm above the surface of the PhCW, together with the fields extracted using Eqs. 6.2a and b. At this height, unlike just above the surface, the profiles of the electric and magnetic fields are noticeably different (see also chapter 4).

In each frame we depict either the amplitude $A(\mathbf{r})$ or the phase $\varphi(\mathbf{r})$ of the in-plane field components (E_x, E_y, H_x, and H_y), with the left half ($y < 0$) taken from fully vectorial 3D calculations (with no fitting parameters) [38] and the right half ($y > 0$) derived from the measurements. As expected due to the symmetry of the PhCW the amplitudes of all components are mirrored about the center of the waveguide ($y = 0$), while the phases of E_x and H_y show an odd symmetry, and those of E_y and H_x

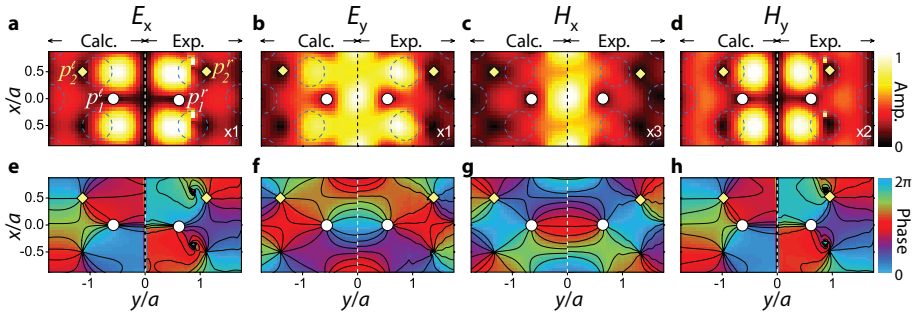

Figure 6.2: Amplitude and phase of the in-plane fields 110 nm above the PhCW. a-d Calculated and experimentally observed amplitude, with **e-h** corresponding phase distributions of the in-plane electromagnetic field components. The relative scaling of the amplitudes is shown in the bottom right corner of **a-d**, and the locations of the holes of the PhCW are indicated by the dashed blue curves. In **e-h** lines of constant phase are shown, and the phase singularities (denoted by solid symbols on all frames) occur where these lines intersect. In each frame we present the fields of 2 unit cells, marking the phase singularities in one of the unit cells. Calculations are shown on the left half of each frame, while the right half depicts the measurements.

show an even symmetry, about this axis. The excellent agreement between the measurements and the calculations nicely demonstrates the successful separation of the electric and magnetic near fields.

6.3 Identification of phase singularities

Within each unit cell, for every field component at this height, we find 2 pairs of phase singularities, which we label $p_1^{\ell,r}$ and $p_2^{\ell,r}$ (e.g. in Fig. 6.2a and e). In addition a line of undefined phase that necessarily occurs at $y = 0$ for the odd-symmetry components (E_x and H_y) where the amplitude is 0. The phase singularities are points of undefined phase , and they can be found in the phase distributions shown in Figs. 6.2e-h at locations where contours of constant phase intersect. We also show the position of the phase singularities in the field amplitude maps (see Figs. 6.2a-d), where they are necessarily found at points of 0 amplitude [112].

	E_x	E_y	H_x	H_y
p_1^ℓ	+1	-1	-1	+1
p_1^r	-1	+1	+1	-1
p_2^ℓ	-1	+1	+1	-1
p_2^r	+1	-1	-1	+1

Table 6.1: Topological charge of the phase singularities in the in-plane fields.

Each phase singularity carries a topological charge

$$s = \frac{1}{2\pi} \oint_C d\varphi, \tag{6.3}$$

where C is transversed in a counter-clockwise manner [112]. In the far filed, this charge denotes the number of units of OAM carried by the surrounding light fields. From the phase maps we calculate that for all phase singularities $s = \pm 1$ (see Tab. 6.1), and hence the total charge of each unit cell is zero[a].

Interestingly, we observe that the phase singularities are located at different position for the different field components. While in all cases p_1 and p_2 are separated by half a period in x, and indeed do not move in x as a function of height, they are found at differing y's. For example, p_1^ℓ of E_y is found at $x = 0$ and $y = (-0.56 \pm 0.07)\, a$, while for H_x it is at $x = 0$ and $y = (-0.66 \pm 0.07)\, a$. Here, the error is determined by the resolution of our measurements.

6.4 Height evolution of phase singularities

We follow the trajectories of the phase singularities, through 3D, space by repeating our measurements at heights ranging from 20 to 400 nm above the PhCW. In Fig. 6.3 we present these trajectories for all four phase singularities of the different in-plane fields, depicting both experimental (symbols) and calculated (curves) results.

Because the symmetry of the PhCW about $y = 0$ ensures that each phase singularity is also mirrored (e.g., p_1^ℓ and p_1^r are equidistant from the

[a] While the edge dislocations at the center of E_x and H_y have an undefined s, since there is no way to close a loop about them.

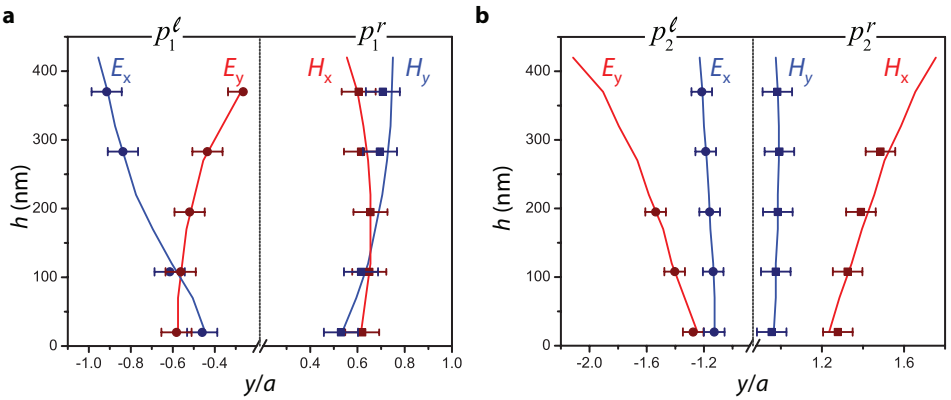

Figure 6.3: Trajectories of phase singularities. a Shows trajectories of p_1 and **b** of p_2 for all in-plane field components. In both panes the trajectory of the phase singularities determined from theoretical modeling is given by the solid curves, while the corresponding experimentally measured positions are shown by the symbols. The error bars represent the resolution of our measurements.

center of the waveguide), we only show the position of one phase singularity from each pair, for each component. For our waveguide, we find that the position of these phase singularities can vary from $y = \pm 190$ nm to $y = \pm 890$ nm over the 400 nm of height that we investigate. Interestingly, near our PhCW the trajectory that a phase singularity for a particular field component follows is distinct. This observation is in contrast to far fields, where typically a clear relationship between the positions of the phase singularities exists. Furthermore, in the near field of the photonic crystal, we can identify heights at which the phase singularities of two field components can be found at the same point (e.g., p_1^ℓ of E_x and E_y at a height of 100 nm, or of H_x and H_y at a height of 150 nm).At other heights the separation between the phase singularities can be greater than the 10's of nm's of a typical quantum structure, or even larger than the 100's of nm of classical objects like our near-field probe.

6.5 Identification of C-points

In the rich structure of the PhCW light fields, phase is not the only quantity that can be singular. As shown by Burresi *et al.* [67], we can also find

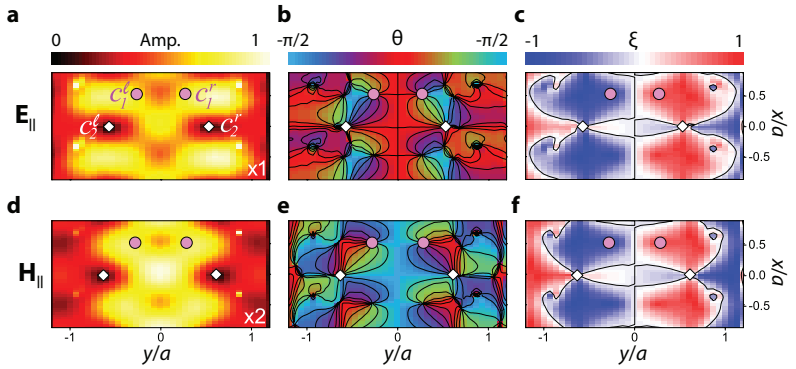

Figure 6.4: Amplitude, orientation and elipticity of the in-plane optical fields 110 nm above the PhCW. a-f The amplitude, angle of orientation and ellipticity of the in-plane electric fields (**a**-**c**) and in-plane magnetic fields (**d**-**f**), respectively. The scaling factors of the field amplitudes are shown in the bottom right corner of **b**, **e**. The polarization singularities, $c_1^{\ell,r}$ and $c_2^{\ell,r}$, are marked by symbols in **a**-**f**. Lines of constant ξ, which intersect at the polarization singularities, are shown in **c**, **e**, as are lines of linear polarization (L-lines) in **c**, **f**.

polarization singularities in these near fields. Unlike phase singularities, which can be found in individual vector components of the electric and magnetic fields, PhCW polarization singularities are properties of the total in-plane electric, or magnetic, field.

The end point of the field vector, at any point in space, traces out an ellipse over time (see Fig. 6.1b). This ellipse can be characterized by its ellipticity,

$$\xi(\mathbf{r}) = \tan\left\{\sin^{-1}\left[\sin\left(2\psi(\mathbf{r})\right)\sin\left(\delta(\mathbf{r})\right)\right]/2\right\}, \tag{6.4}$$

which denotes the ratio of the short to long axis, and which ranges from +1 (right-circular polarization) to -1 (left-circular polarization) and represents linear polarization when $\xi = 0$, and its orientation angle,

$$\theta(\mathbf{r}) = \left\{\tan^{-1}\left[\tan\left(2\psi(\mathbf{r})\right)\cos\left(\delta(\mathbf{r})\right)\right]\right\}/2, \tag{6.5}$$

which ranges from $+\pi/2$ to $-\pi/2$. In these equations $\psi(\mathbf{r}) = \tan^{-1}\left[A_x(\mathbf{r})/A_y(\mathbf{r})\right]$ and $\delta = \varphi_x(\mathbf{r}) - \varphi_y(\mathbf{r})$, and $A(\mathbf{r})$ and $\varphi(\mathbf{r})$ are the amplitude and phase, respectively, of either $\mathbf{E}$ or $\mathbf{H}$.

In Fig. 6.4 we present the amplitude, θ and ξ of the in-plane electric and magnetic fields, measured 110 nm above the surface of the PhCW, in which we look for polarization singularities. Polarization singularities are points where either the handedness (sign of ξ) or orientation (θ) of the polarization are undefined. The former occur where the polarization is linear ($\xi = 0$), which occur on lines. These lines are therefore known as L-lines. The latter, polarization singularities, are of particular interest, as in two dimensions they occur in points – so-called C-points– where the optical fields carry spin angular momentum. In analogy to phase singularities, polarization singularities are found where lines of constant θ intersect (see Fig. 6.4b, e), and where the polarization is circular ($\xi = \pm 1$ in Fig. 6.4c, f).

We find 4 C-points per unit cell, which we denote $c_1^{\ell,r}$ and $c_2^{\ell,r}$. As we see from the ξ maps in Fig. 6.4c, f, each pair of C-points contains polarization singularities of both handedness', as is required for C-points that are separated by an L-line (see Fig. 6.4c as an example). For example, for the electric field, the polarization at c_1^{ℓ} is left-handed while at c_1^{r} it is right-handed. We note that only at c_1 of the electric field does the associated out-of-plane component vanish (i.e. $E_z \to 0$), and hence only this point is a true polarization singularity in 3D space. Interestingly, we find points c_1 in regions of high in-plane field amplitude. In analogy with the phase singularities, about which a nanoscopic object would rotate, an object placed a C-point would begin to spin (in place). Likewise, it is important to know if the object is electric or magnetic in nature since the C-points associated with the electric and magnetic fields are typically found in different locations.

Each of the C-points that we have identified in the near fields of the photonic crystal has, in addition to a handedness, a type and index [115]. Both the type and index can be determined by looking at how the orientation of the ellipse varies and in the area about the C-point. In Fig. 6.5 we show the long axis of the polarization ellipse for both the electric and magnetic fields, at a height of 20 nm above the PhCW.

In each frame we outline the lines traced out by the ellipse orientation, as one moves away from the C-point. From this figure we see that, near c_1 (blue curves), the pattern of the orientations of the ellipse has a three-fold symmetry, corresponding to a star-type C-point [115]. By tracing out the way θ changes about this point (in Fig. 6.4), we see that the index of this C-point is $-1/2$. Likewise, from the area near c_2 (red curve), we see that

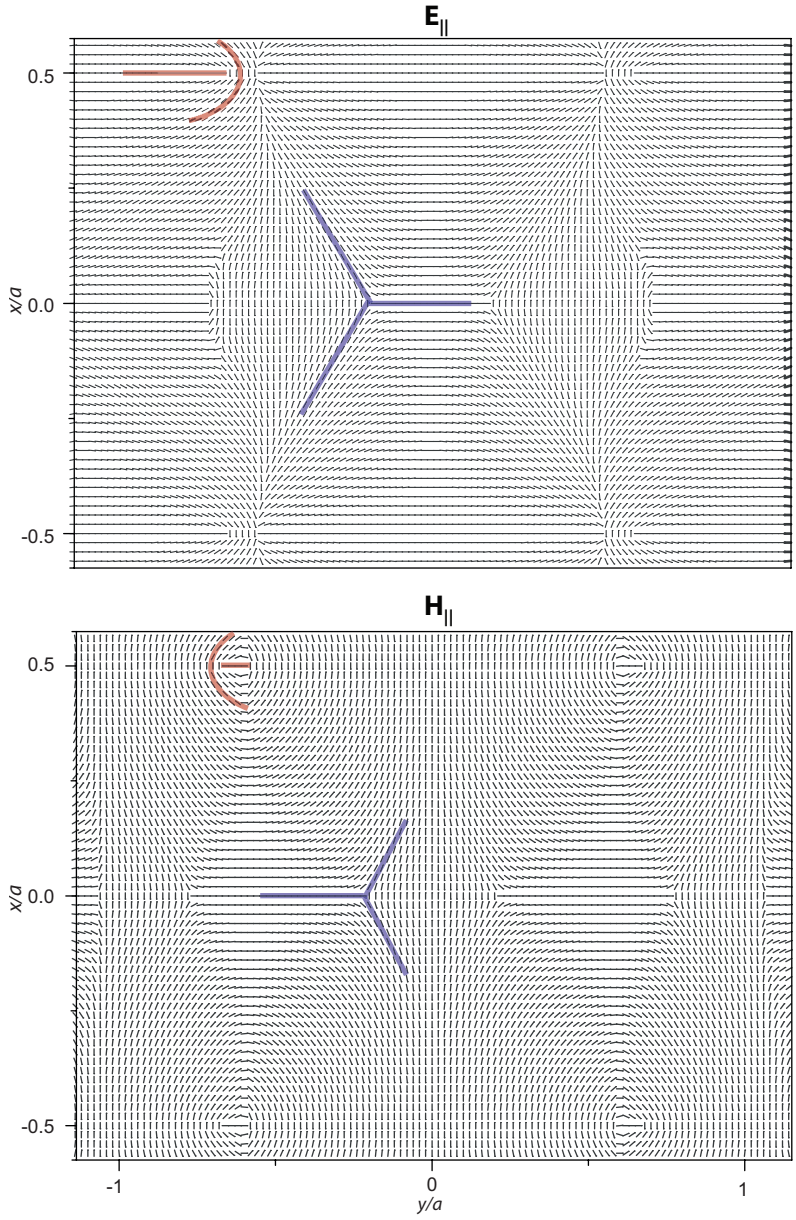

Figure 6.5: Electric and magnetic polarization ellipse orientations. Calculated orientations of the long axis of the polarization ellipse, 20 nm above the PhCW. The star shape of c_1 is outlined in blue, and the lemon nature of c_2 in red. Note that the unit cell has been shifted by $-0.5\ x/a$, relative to Fig. 6.4, to place c_1 in the center along x of the image.

c_2 is a lemon-type C-point with an index of $+1/2$. We find that for c_1 and c_2 the type and index are the same for the electric and magnetic fields.

6.6 Height evolution of C-points

Now that we have identified and characterized the C-points at the surface, we follow their trajectory through 3D space (see Fig. 6.6). This figure illustrates that the trajectory of each C-point is unique. As is evident from this figure, while polarization singularities appear as points in a given plane, in 3D space they trace out lines (while L-lines trace out surfaces). Following these trajectories is particularly important for c_1, which are located regions of high field, but which are also only found relatively close to the PhCW. In the electric field, we find polarization singularities up to a height of about 175 nm, while for the magnetic field they are present up to about 275 nm. The vanishing of polarization singularities, without annihilation [116], is intriguing as analogous behavior has neither been observed nor predicted in the far field. Further, we observe that the trajectories of c_1^ℓ and c_1^r diverge for both **E** and **H**, suggesting that if one wishes to only sample the local properties of the fields then working at greater heights is desirable. For example, the separation between c_1^ℓ and c_1^r, which we denote Δy, is only 160 nm at a height of 20 nm above the PhCW, but it grows to 250 nm at a height of 170 nm. We recall, however, that the fields are evanescent and hence their amplitude decreases at greater heights, suggesting a balance between C-point separation and field amplitude that would need to be struck in a potential application. For example, in chapters 7 and 8 we demonstrate that this balance is very relevant for the nanophotonic control over circular dipoles.

Figure 6.7a shows the calculated amplitude of the in-plane electric field at the location of the C-points shown in Fig. 6.6, as a function of height. As expected, because the light fields evanescently decay away from the surface of the PhCW, the field amplitude rapidly decreases for increasing heights. A closer inspection of this figure reveals that the fall-off of the field amplitude is not a single exponential, but instead has a more complex form [42]. This deviation from exponential decay is particularly evident from the amplitudes found for $c_2^{\ell,r}$ (blue curve), which appear to have a local minimum at a height of ~ 100 nm and then to *increase* for larger heights. The complex behavior of the field amplitude at the C-points occurs both

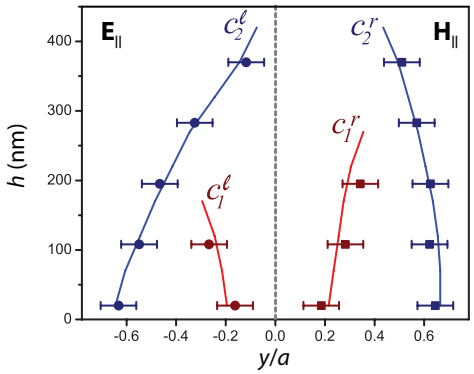

Figure 6.6: Trajectories of the polarization singularities. The left side shows two of the polarization singularities of the in-plane electric field, and the right side shows two of the in-plane magnetic field. Both calculations (curves) and measurements (symbols) are shown, and the error bars on the latter are due to the experimental resolution.

because, as discussed in the main text, the field distributions themselves are height dependent, and because the position of the C-point within the field distribution changes for different heights. This is easier to see in the insets to Fig. 6.7a, which show the value of $|\mathbf{E}_\parallel|$ at the location of the C-points, relative to the maximum of $|\mathbf{E}_\parallel|$, for each height. As can be seen for $c_1^{\ell,r}$ (top inset), the polarization singularities move towards the points of maximum in-plane $\mathbf{E}$ at larger heights. Conversely, $c_2^{\ell,r}$ scan across an oscillatory feature of the field and so their normalized amplitude, while always much smaller than that of $c_1^{\ell,r}$, also oscillates. Similar observations can be made for the C-points in the magnetic field, shown in Fig. 6.7b. Combined these observations emphasize the intricate 3D evolution of the polarization singularities near a nanophotonic structures, which can even differ between the electric and magnetic polarization singularities.

6.7 Conclusions

In summary, we identify two types of singularities in the near fields of a photonic crystal waveguide and we directly observe the trajectories that these singularities follow through 3D space. Our results are in excellent agreement with calculations, and they highlight the nontrivial relation be-

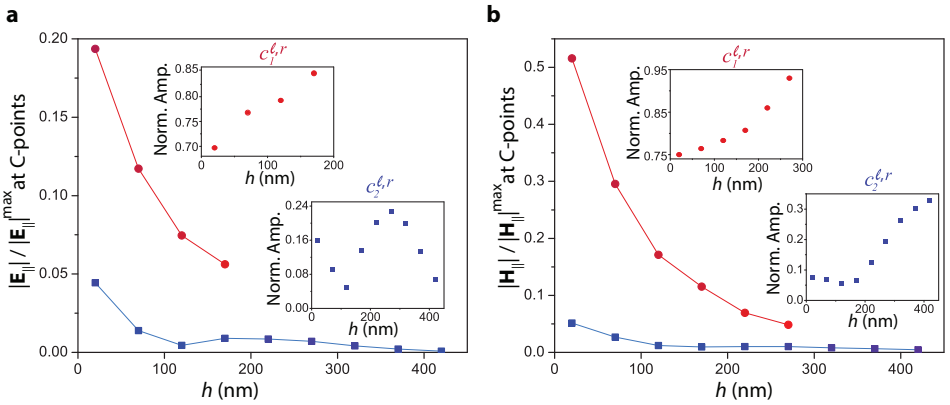

Figure 6.7: Height evolution of C-point amplitude. **a**, **b** Show the in-plane electric (**a**) and magnetic field (**b**) amplitude, at the positions corresponding to the C-points shown in Fig. 6.6, relative to the maximum amplitude of the in-plane electric (**a**) and magnetic fields (**b**) 20 nm above the surface of the PhCW. In **a**, **b** the insets show the electric field amplitude at the C-point relative to the maximum in-plane amplitude for each height.

tween the electric and magnetic near fields of nanophotonic structures. That is, using nanoscopic geometry, it is possible to create sub-wavelength, fine structure in light fields that behaves in a manner that cannot always be reproduced in the far field. Thereby this work paves the way for a unique nanophotonic control over the transfer of SAM and OAM to nearby particles. Furthermore, in the following two chapters we extend the insights into the structure and evolution of nanoscale light fields to help unlocking a nanophotonic system that allows for on-chip entanglement between the spin of a quantum emitter and the path of a photon.

7

Toward a scalable solid-state to photonic-qubits interface

Controlling photon emission by quantum emitters with nanostructures is crucial for scalable on-chip quantum information processing. Nowadays nanoresonators can affect the lifetime of emitters and ultimately induce strong coupling between the emitters and the light field, while nanoantennas can control the directionality of the emission. Expanding this control to the manipulation of the emission of orbital angular momentum-changing transitions would enable a coupling between long-lived solid-state and photonic qubits. As these transitions are associated with circular rather than linear dipoles, achieving such a coupling requires an excellent understanding of the nanophotonic control over circular dipoles. Using a classical analogue, we experimentally map the coupling of circular dipoles to the modes in a PhCW. We show that depending on the local helicity the dipoles can be made to couple to modes either propagating to the left or to the right. The maps are in excellent agreement with calculations. Our measurements, therefore, demonstrate the coupling of spin to pathway with near-unity (0.8 ± 0.1) efficiency.

7.1 Introduction

Control of the emission properties of circular dipole sources, where the phase of the orthogonal linear dipole components cannot be neglected, with a scalable nanophotonic interface would constitute a tremendous step toward viable, on-chip quantum information processing. This control would allow for manipulation of the emission properties associated with the long-lived spin states of solid-state emitters, such as quantum dots [117, 118, 119, 120] and nitrogen vacancy centers [121, 122, 123], as their orbital angular momentum-changing decay to specific spin states is associated with the helicity of circular transition dipoles [124] (see Fig. 7.1). Furthermore, if we interface nanophotonic structures with spin qubits, all the lessons learned from the study of how such structures interact with linear dipoles to, for example, control their decay rates [48, 43, 125] or the directionality of their emission [126, 127] could be immediately applied. With such an interface we could couple, or even entangle, solid-state emitters to photonic pathways, essentially encoding the quantum information of a long-lived solid-state qubit onto a versatile photonic qubit [128, 129], allowing for a new avenue toward quantum information processing elements.

Clearly, tremendous benefits can be obtained from a controlled interface of nanophotonics with spin-states of emitters. Ideally, such an interface will be deterministic, meaning that all emission is into the desired modes of the nanophotonic structure and not into free space, and that each distinct spin state of the emitter is coupled to a single photonic pathway. The former requirement can be met by, for example, placing a quantum emitter inside a photonic crystal waveguide, which enables the extraction of over 98 percent of the QD emission [131]. The latter requirement has, to date, not been demonstrated, although researchers have recently shown preferential emission of QDs situated at the crossing of two ridge waveguides [124]. It was shown that, depending on the helicity of its circular transition dipole, a QD preferentially emits into two of the four exit waveguides.

For a deterministic interface of emitter spin to photon pathway, detailed knowledge of the projection of a circular dipole onto the optical eigenstates of a nanophotonic structure is required. Specifically, because these optical eigenstates are typically highly spatially structured (see Sec. 1.2) and can contain local helicity [67], a realization of such an interface requires a spatial mapping of the projection of circular dipoles to these optical eigenstates. Evidently, such knowledge is key if the emitter is to be correctly

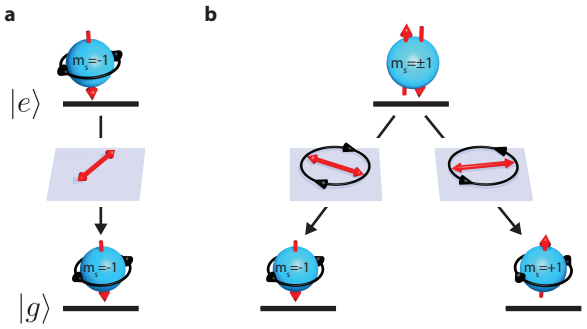

Figure 7.1: Schematic of dipole mediated transitions. Sketch of an emitter decaying from its excited state $|e\rangle$, to its ground state $|g\rangle$. The ground and the excited state electron have the same spin, for example $m_s = -1$. The transition between the two levels results in the emission of a photon. The associated transition dipole (middle row) arises due to the redistribution of charges in the emitter during the transition. **a** A transition that does not change the emitters total angular momentum. Such a transition is mediated by a linear transition dipole. **b** Sketch of an emitter prepared in an excited state that is a superposition of $m_s = -1$, $m_s = +1$, decaying with equal probability to either of the two ground states [130]. This decay is associated with a circular transition dipole, as sketched in the middle row, and the emission of a circularly polarized photon [130].

positioned. In practice, the fine details of the optical modes are highly dependent on the geometry of the nanostructure, and hence are sensitive to imperfections. Moreover, fabricating emitters in precise locations on nanophotonic structures is a complex and challenging procedure, which ultimately imposes additional constraints on the feasibility of a solid-state to photonic-qubit interface. For example, the interaction of the nanophotonic structure and the emitter must be relatively constant over an area defined by the precision with which the emitter can be placed, typically on the order of tens of nanometers [132, 133]. Consequently, a demonstration of viable nanophotonic interface for solid-state and photonic qubits must fulfill two requirements. First, efficient and directional coupling between a circular dipole and a photon pathway must be observed on a real nanophotonic structure. Second, a full spatial mapping of the interaction of the dipole and this structure must be created.

Here, we use a classical, tunable dipole source to demonstrate near-perfect coupling of helicity to photon pathway in a PhCW. First, we experimentally show that the radiation from the tip of a near-field optical microscope probe can mimic that of a linear transition dipole. Subsequently, we extend this method to emulate the emission of a circular transition dipole, i.e. one that is associated with a change in the emitter's spin state. By scanning this tunable source we create high resolution spatial maps of its emission into the PhCW, for different circular dipoles. We show that the helicity of the light emitted by such circular dipoles in combination with the unique local helicity of the photonic eigenstates of the PhCW leads to efficient and deterministic directional emission. We underpin these experimental observations with a rigorous theoretical framework that describes the radiation of circular dipoles near a PhCW. Because the emission of a photon by a transition dipole and a classical dipole into a PhCW is identical in the weak coupling limit, our result demonstrates that scalable spin-to-pathway coupling is possible.

7.2 Emission control with photonic crystal waveguides

The way in which an emitter, and in particular a quantum emitter, radiates when placed near a nanophotonic structure is a subject of intense research [48, 43, 125, 126, 127, 134, 135, 136, 47]. The decay of a two-level system, an inherently quantum process, is associated with a transition

dipole (sketched in Fig. 7.1), which arises due to charge redistribution that occurs in the emitter during the transition. The radiation of the transition dipole is identical to that of a classical dipole, except that a transition dipole only exists for the duration of a single radiation event. As we discussed in chapter 7, when an emitter is placed near a nanophotonic structure the radiation probability of the transition dipole is altered by the number of photonic states into which it can emit.

To find the emission enhancement by a PhCW we make use of a Green's function formalism. Assuming that the emission of a nearby emitter is completely into the PhCW its Green's function can be found analytically [47]. We extend the Green's function found in [47], to separate the effect of the left- (L) and rightwards (R) propagating modes on the radiation of the emitter. That is, we write

$$\overleftrightarrow{\mathbf{G}}_{L,R}(\mathbf{r},\mathbf{r};\omega) = \frac{ia\omega n_g(\omega)}{4c}\left(\mathbf{e}_{L,R}(\mathbf{r},\omega)\otimes\mathbf{e}^*_{L,R}(\mathbf{r},\omega)\right), \tag{7.1}$$

where $\mathbf{e}_{L,R}(\mathbf{r},\omega)$ are the electric (magnetic) fields of the normalized left- and right-propagating modes of the PhCW that interact with a dipole, whose orientation is indicated by the unit vector $\hat{\mathbf{d}}$. This dipole can be electric ($\hat{\mathbf{p}}$) or magnetic ($\hat{\mathbf{m}}$) in nature, or both. In accordance with [47] we normalized $\mathbf{e}_{L,R}(\mathbf{r},\omega)$ such that $\int|\mathbf{e}_R(\mathbf{r},\omega)|^2\epsilon_d(\mathbf{r})\mathrm{d}\mathbf{r}=1$, where ϵ_d is the relative permittivity at the dipole location. We insert Eq. 7.1 into Eq. 1.8, and project onto a purely electric dipole. In this manner we straightforwardly find the emission enhancement of an electric dipole relative to free space

$$F_{L,R}(\hat{\mathbf{p}},\mathbf{r},\omega) = \frac{3\pi c^2 a n_g(\omega)}{2\omega^2\sqrt{\epsilon_d(\mathbf{r},\omega)}}\left|\hat{\mathbf{p}}^*\cdot\mathbf{e}_{L,R}(\mathbf{r},\omega)\right|^2. \tag{7.2}$$

From Eq. 7.2 it is clear that for perfectly directional emission into the PhCW we need $|\hat{\mathbf{p}}^*\cdot\mathbf{e}_L(\mathbf{r}_0,\omega)|=1$ and $|\hat{\mathbf{p}}^*\cdot\mathbf{e}_R(\mathbf{r}_0,\omega)|=0$, or vice versa, for certain positions $\mathbf{r}_0$. For circular dipoles to maximally directionally emit into the PhCW, therefore, we require positions where the left and right propagating modes are circularly polarized, but with the opposite helicities.

Photonic crystal waveguides, by virtue of their highly structured near-field distributions that locally sample all in-plane vectorial field orientations [67], seem ideally suited to couple emission to pathway. Our PhCW

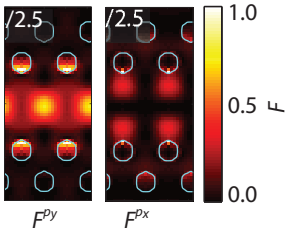

Figure 7.2: Calculated linear dipole emission enhancement factors. Calculated enhanced emission factors F^{p_x} and F^{p_y} (for light traveling to the left) for x- and y-oriented electric dipoles, respectively, placed in the center of the PhCW. Blue circles indicate the edges of the holes in the PhCW. The scaling factor indicated in the top left of each panel scale the panels maximal to 1.

consists of a 200 nm thin Si slab, perforated with a hexagonal lattice (420 nm periodicity) of 110 nm holes. The innermost row of holes (compared to the line defect) is shifted outwards by 45 nm and the second row in shifted inward by 30 nm. As an example of the highly structured near fields in this structure, we show the calculated emission enhancement in the center height of the slab for $\hat{\mathbf{x}}$ and $\hat{\mathbf{y}}$ oriented linear dipoles in Fig. 7.2. Importantly, for both dipole orientations, the maps of the linear dipole emission modification factor $F_R\left(\hat{\mathbf{p}}_{x,y}\right)$ (not shown) are identical to those of $F_L\left(\hat{\mathbf{p}}_{x,y}\right)$. So for a linear dipole the emission near the PhCW is not directional.

7.3 Mimicking linear dipole emission

We mimic the behavior of a dipolar emitter using the emission from a 190 nm wide, NSOM probe, which is known to act as a continuous transition dipole [58, 57, 137] (see Fig. 7.3b). We raster scan the probe in the sample plane at a height of 20 nm above the slab. While scanning, we collect the light coupled to the waveguide in a heterodyne detection scheme that gives us access to its phase (see Fig. 7.3a). We use the phase information to Fourier filter unwanted reflections from the waveguide end facets (see chapter 2), mapping out the emission into both the left- and rightwards propagating modes, $D_L\left(\hat{\mathbf{d}},\mathbf{r}\right)$ and $D_R\left(\hat{\mathbf{d}},\mathbf{r}\right)$, respectively.

Because we wish to couple helicity to path, we need to confirm that we

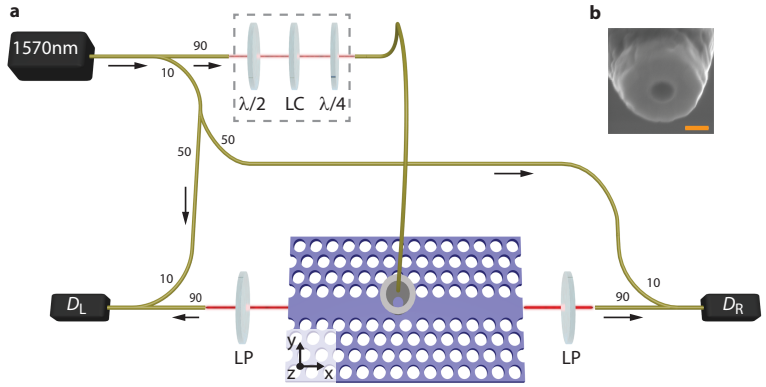

Figure 7.3: An illumination-mode NSOM mimics dipolar emission into a PhCW. a Schematic of the near-field scanning optical microscope, operating in illumination mode, that acts as a dipolar source. Light (with a wavelength of 1575 nm) from a continuous-wave laser is split into reference and signal branches with the ratios shown. The polarization of the light in the signal branch, and hence the orientation of the dipole mimicked by the NSOM probe, shown in **b**, is controlled by a the polarization control scheme (dashed gray rectangle) that includes a half-wave ($\lambda/2$), a liquid crystal (LC) and a quarter-wave ($\lambda/4$) plate. Light that couples to the PhCW travels to the left, or right, where it is detected in D_L and D_R, respectively, in an interferometric manner. **b** SEM image of the near-field probe used in this work, with a 200 nm scale bar.

can control the orientation and phase of our dipole source. We start by showing that we can create any linear dipole, in this case by varying the orientation of our dipole from $\hat{\mathbf{x}}$ to $\hat{\mathbf{y}}$. At this wavelength the PhCW interacts with magnetic dipoles in much the same way as it does with electric dipoles (see chapter 4). Consequently, we limit the following discussion to electric dipoles. We vary the orientation of the dipole by controlling the polarization of the light that we inject into our near-field probe. The linear dipole emission maps are presented in Fig. 7.4. These emission maps show that $\hat{\mathbf{x}}$ and $\hat{\mathbf{y}}$ oriented dipoles emit in drastically different ways into the PhCW, but as expected we do not observe directional emission: the emission exhibits no left-right asymmetry. These measurements are in excellent agreement with the calculations 20 nm above the PhCW slab (see Fig. 7.4).

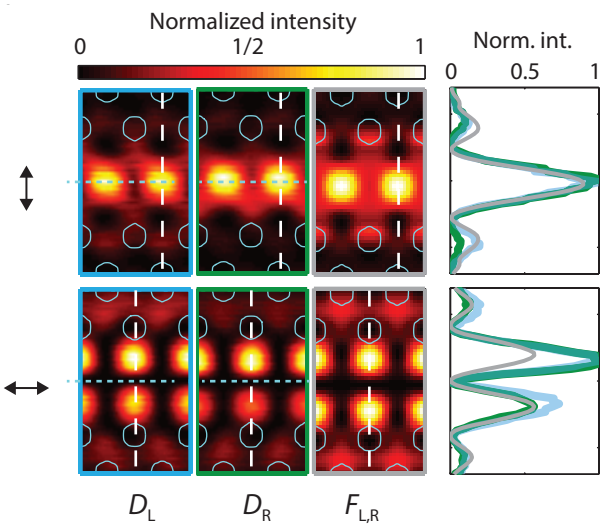

Figure 7.4: Dipolar emission into a PhCW. Emission maps collected with the left (D_L, left column) and right (D_R, middle column) detectors, together with the calculated emission enhancement maps for linear dipoles 20 nm above the PhCW slab ($F_{L,R}$, right column), at 1575 nm with linear dipoles (orientation indicated by the black arrows). Line traces are taken along the white dashed lines shown in the graphs on the right, with the blue (green) lines corresponding to line traces through D_L (D_R). Grey lines show cuts through the calculated F^{p_x} (bottom panel) and F^{p_y} (top panel). In all maps, light blue circles indicate the holes of the PhCW and blue dashed lines mark the center of the waveguide.

7.4 Mimicking circular dipole emission

To create circular dipoles, such as those associated with orbital angular momentum-changing transitions (see Fig. 7.1b), we need to control the phase of our dipole source. Hence, we add a liquid-phase plate to our polarization control optics (LC in Fig. 7.3a), which allows us to create $\widehat{\mathbf{d}} = (\hat{\mathbf{p}}_x \pm i\hat{\mathbf{p}}_y)/\sqrt{2}$ sources (see appendix A). This polarization control enables us to experimentally map the emission control over circular dipole sources offered by the PhCW.

Strikingly, both the measured $D_{L,R}$ and the calculated $F_{L,R}$ for these circular sources (see Fig. 7.5) exhibit a pronounced asymmetry, which was absent for the linear dipole sources. In fact, we observe that flipping either

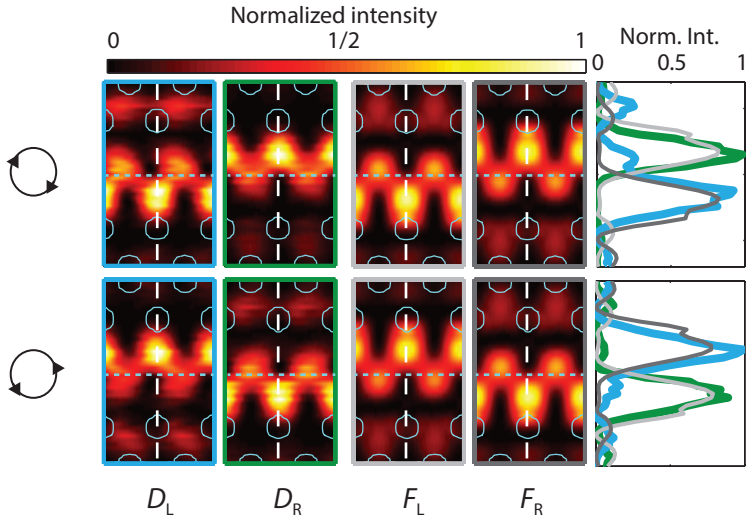

Figure 7.5: Emission of circular dipoles. Experimental and calculated emission maps of right- (top row) and left-handed (bottom row) circular dipoles. In each row the two left (right) panels depict experimental (theoretical) emission maps. The line traces (taken along the white dashed line) correspond to cuts through D_L (blue) and D_R(green), and are shown together with calculated cuts through F_L (dark gray lines) and F_R (light gray lines). In all maps, light blue circles indicate the holes of the PhCW and blue dashed lines mark the center of the waveguide.

the direction of the detector path (i.e. monitoring either D_L or D_R) or the dipole helicity ($(\hat{\mathbf{p}}_x - i\hat{\mathbf{p}}_y)/\sqrt{2}$ or $(\hat{\mathbf{p}}_x + i\hat{\mathbf{p}}_y)/\sqrt{2}$) results in a mirroring of the emission map about the middle of the waveguide ($y = 0$, dashed blue lines Fig. 7.5). For example, the emission of a right-handed dipole (top row of panels Fig. 7.5) is predominantly to the left when the dipole is placed over the bottom half of the waveguide ($y < 0$), and to the right when the dipole is located in the top half ($y > 0$). We take line cuts (along the dashed white lines in Fig. 7.5) to illustrate the high degree of coupling between helicity and direction. For both dipole handednesses maximal emission in one direction corresponds to a minimum in the other.

7.5 Helicity to pathway coupling strength

To compute the coupling strength between helicity and path we compute the directionality of the emission from the experimental emission maps. That is, we define the directionality, η_{dir}, as follows:

$$\eta_{dir}\left(\mathbf{r},\omega\right)=\frac{D_L\left(\hat{\mathbf{d}}_{LCP}\right)-D_R\left(\hat{\mathbf{d}}_{LCP}\right)}{D_L\left(\hat{\mathbf{d}}_{LCP}\right)+D_R\left(\hat{\mathbf{d}}_{LCP}\right)}-\frac{D_L\left(\hat{\mathbf{d}}_{RCP}\right)-D_R\left(\hat{\mathbf{d}}_{RCP}\right)}{D_L\left(\hat{\mathbf{d}}_{RCP}\right)+D_R\left(\hat{\mathbf{d}}_{RCP}\right)}, \tag{7.3}$$

where LCP and RCP indicate left- and right-handed dipoles, respectively. Strikingly, the line traces and maps of $\eta_{dir}(\mathbf{r})$ (see Fig. 7.6a, b) reveal that large areas of near-unity dipole helicity to path coupling are available above the waveguide. We support these observations by calculating the theoretical η_{dir}, using Eqs. 7.2 and 7.3 with $\hat{\mathbf{d}}=\left(\hat{\mathbf{p}}_x\pm i\hat{\mathbf{p}}_y\right)/\sqrt{2}$ (directionality maps and line traces are shown in Fig. 7.6a, b). Importantly, these calculations are in excellent agreement with both the measured η_{dir} maps and line traces, and reveal a helicity-to-path coupling as large as one. The contour lines plotted in Fig. 7.6c emphasize the large size of the areas of the near-unity directional coupling.

However, because η_{dir} only measures the directionality and contains no information about the efficiency with which photons are emitted to the PhCW, $\eta_{dir}(\mathbf{r})$ can still be unity even though very little light is actually emitted to the PhCW. Hence, for our approach to dipole helicity to pathway coupling to be a viable route toward on-chip quantum technology, not only the directionality but also the emission rate itself needs to be maximized. Therefore, we define the directional coupling efficiency (η),

$$\eta\left(\mathbf{r},\omega\right)=\frac{\left[D_L\left(\hat{\mathbf{d}}_{LCP}\right)-D_R\left(\hat{\mathbf{d}}_{LCP}\right)\right]-\left[D_L\left(\hat{\mathbf{d}}_{RCP}\right)-D_R\left(\hat{\mathbf{d}}_{RCP}\right)\right]}{2D_{\max}}, \tag{7.4}$$

where $D_{\max}$ is the maximum intensity found in any of $D_L\left(\hat{\mathbf{d}}_{LCP}\right)$, $D_R\left(\hat{\mathbf{d}}_{LCP}\right)$, $D_L\left(\hat{\mathbf{d}}_{RCP}\right)$ and $D_R\left(\hat{\mathbf{d}}_{RCP}\right)$. If $\eta\left(\mathbf{r},\omega\right)=0$, either the chance of emitting a photon left and right is equal, or no photons are emitted into the PhCW. Conversely, if $\left|\eta\left(\mathbf{r},\omega\right)\right|=\pm1$, then at spin is both deterministically coupled to path and a circular dipole emits maximally. Fig. 7.6d (left panel)

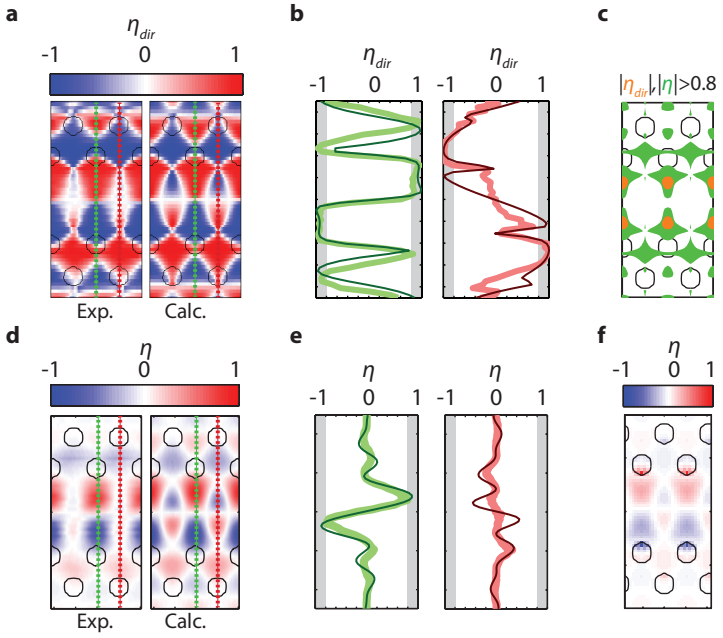

Figure 7.6: Helicity-to-path coupling strength and efficiency. **a**, **d** Experimental (left) and calculated (right) maps of η_{dir} (**a**) and η(**d**). **b, e** Line traces along the green (left panel) and red dashed lines (right panel) in **a** (shown in **b**) and **d** (shown in **e**). Grey shaded region indicate where $|\eta_{dir}|, |\eta| > 0.8$. **c**, **f** Orange contours show regions where $|\eta_{dir}| > 0.8$ (**c**) and $|\eta| > 0.8$ (**f**). In **a, c, d, f** black circles indicate the holes in the photonic crystal membrane.

presents $\eta(\mathbf{r}, \omega)$ determined for the individually measured emission maps shown in Fig. 7.6. Astonishingly, we still observe relatively large regions where the helicity of the dipole almost perfectly determines the pathway that a photon will take, both to the left ($\eta \to 1$, red regions) and to the right ($\eta \to -1$, blue regions). In fact, we observe a maximal helicity-to-pathway coupling of $|\eta|^{exp}_{max} = 0.8 \pm 0.1$, where the deviation from unity is largely due to experimental noise.

We again underpin our observations by calculating the theoretical efficiencies η, using Eq. 7.2 and 7.3 with $\hat{\mathbf{d}} = (\hat{\mathbf{p}}_x \pm i\hat{\mathbf{p}}_y)/\sqrt{2}$. The calculations (right panel of Fig. 7.6d) are in excellent agreement with the measurements, as can also be seen from the line cuts (see Fig. 7.6e) taken at positions of

maximal directionality. The maximum theoretical directional coupling efficiency ($|\eta|^{\mathrm{calc}}_{\mathrm{max}}$) for this PhCW is 0.95, meaning that a circular dipole has the highest and most directional emission at the same locations. Furthermore, the excellent agreement between calculations and experiment allows us to extend our coupling efficiency calculations near the center of the slab. Fig. 7.6 illustrates that at the center height in the slab, where dipolar emitters emit with near-unity efficiency to the PhCW [131], a strong helicity to path coupling efficiency is possible. Specifically, at the center of the slab we find a maximal $|\eta|^{\mathrm{calc}}_{\mathrm{max}} > 0.99$.

7.6 Conclusions

In conclusion, we have shown through classical measurements that a PhCW can be used to deterministically couple circular dipole helicity to pathway. Experimentally, we observe a coupling efficiency of 0.8 ± 0.1, with a theoretical limit of unity, which can be found in a relatively large region. Our observations of high directional efficiency, combined with observations that PhCWs can be used to almost perfectly extract radiation from QDs within the slab [138, 131], demonstrate the two key requirements of a deterministic spin to pathway interface. In fact, recent experiments have suggested that such an interface may be viable for systems other than QDs such as, for example, atoms [135, 139, 140]. Such an interface, be it for QDs, atoms, or any other emitter, would allow for the entanglement of emitter spin to photonic pathway [129], or could even be used to create quantum logic gates [128, 129], an important step toward future on-chip quantum optics applications.

8

Controlling electric and magnetic circular dipoles

In this chapter we explore the nanophotonic control over the helicity-to-path coupling of both circular electric and circular magnetic dipoles. Firstly, we study the wavelength dependence of the emission of linear electric and magnetic dipoles. Then we investigate how the helicity-to-path coupling strength of circular electric and magnetic dipoles varies with wavelength. We demonstrate that the emission wavelength can be used to tune the strength and position of efficient helicity to path coupling of both dipole types. We show that the helicity of both dipole types at all investigated wavelengths can be coupled to a propagation direction. Finally, we present calculations that show that photonic crystal geometry can be tuned to achieve near-unity helicity to path coupling for both electric and magnetic dipoles over a 30 nm window.

8.1 Introduction

Over the last decades nanophotonic structures have been intensively used to engineer the lifetimes and emission direction of nearby emitters. The extend to which these effects take place is a delicate interplay between, on the one hand, the properties of the nanophotonic structure's optical states, and, on the other hand, properties of the emitter, such as its position, emission wavelength, dipole orientation and wavelength. Additionally, in the previous chapter we identified the helicity of the emitter dipole as a property that can completely direct the dipolar emission direction into a PhCW. Importantly, it is the *combination* of all these properties and the optical eigenstates that determines the total effect on an emitters emission direction and lifetime.

In this context PhCWs have been intensively studied because their intricately structured eigenstates enable an extraordinary and position dependent control over the emission rates of nearby emitters [125, 48]. This change of an emitter's lifetime is proportional to the slow down of light in PhCWs (see Eq. 7.2), which can depend strongly on the emission wavelength because PhCWs are highly dispersive (see Sec. 1.3.3). Importantly, associated with the slow down of light in a PhCW is a redistribution of the modal field [39, 40]. Interestingly, because the vectorial modal fields change with emission wavelength, the emission wavelength might also affect the possibility of coupling dipole helicity to photon path.

Furthermore, so far we have studied the possibility of electric dipole helicity to path coupling, additionally, the control over magnetic dipoles has recently attracted considerable interest [92, 141]. This recent interest in magnetic emitters, draws attention to the possibility of coupling the spin of a magnetic emitter to a photonic path.

In this chapter, we study the effect of both the emission wavelength and dipole nature on the coupling between dipole helicity and photon path. Firstly we study the emission of linear electric and magnetic dipolar emitters at wavelengths corresponding to a tuning of the group index by an order of magnitude. Then, we turn to circular dipoles and we investigate the effect of dipole nature and wavelength on the helicity to path coupling of electric and magnetic circular dipoles.

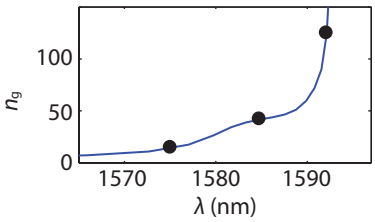

Figure 8.1: Calculated group index of the PhCW. Calculated relation between group index and wavelength. Black dots indicate the wavelengths at which we measure.

8.2 Calculated linear electric and magnetic dipole emission

In Fig. 8.1 we show the calculated dispersion relation of our PhCW, which is the same as in the previous chapter. In this dispersion relation we can identify three regimes, the fast light, the slow light, and the very slow light. In this chapter, we investigate the emission of dipolar emitters in each of these regimes. That is, we will investigate the emission of electric and magnetic dipoles at 1575, 1585 and 1592 nm, corresponding to an n_g of 15, 40 and 120 respectively. The calculated F maps at these wavelengths for x- and y- oriented electric dipoles (see Fig. 8.2a) show that the maximum enhancement factor changes from 1.6 at 1575 nm ($n_g = 15$) to 9.5 at 1592 nm ($n_g = 120$). Furthermore, with increasing n_g high enhanced emission factors become available away from the center of the waveguide at $y = 0$ (dashed blue lines, Fig. 8.2). This is expected since the PhCW modes typically spread out as the light slows down [40, 39].

From our expression of the emission enhancement for an electric dipole we can find the expression for the emission enhancement of a magnetic dipole. Specifically, to find the emission rate enhancement factor for a magnetic dipole we perform the substitution suggested in [8] and in Eq. 7.2 we replace $[\mathbf{E}, \mathbf{H}, \mu_0\mu, \epsilon_0\epsilon, \mathbf{p}]$ with $[\mathbf{H}, -\mathbf{E}, \epsilon_0\epsilon, \mu_0\mu, \mu\mathbf{m}]$. Consequently, we find that for a magnetic dipole

$$F_{L,R}\left(\hat{\mathbf{m}}, \mathbf{r}, \omega\right) = \frac{3\pi c^2 a n_g\left(\omega\right)}{2\omega^2} \left|\hat{\mathbf{m}}^* \cdot \mathbf{e}_{L,R}\left(\mathbf{r}, \omega\right)\right|^2, \tag{8.1}$$

where the dot product effectively selects the magnetic fields of the mode that the dipole couples to.

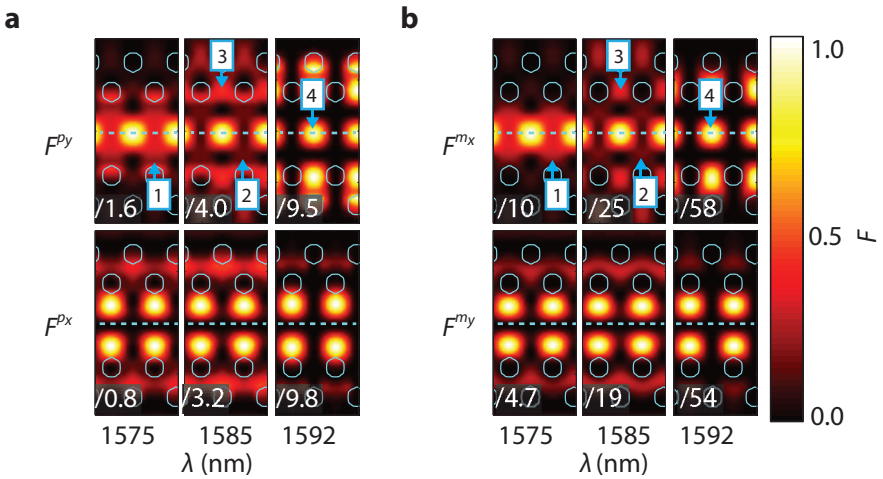

Figure 8.2: Calculated emission enhancement of linear electric and magnetic dipoles. a Emission enhancement factor for y- (top row of panels) and x-oriented (bottom row) electric dipoles 20 nm above the PhCW slab for three emission wavelengths. **b** Emission enhancement factor for x- (top row of panels) and y-oriented (bottom row) magnetic dipoles 20 nm above the PhCW slab for three emission wavelengths. The factors in the bottom left of each panel scale the panels maximal to 1. Blue dashed line indicate the -plane of mirror symmetry of the crystal, blue circles indicate the PhCW holes. Blue labels 1-4 in **a** and **b** correspond to the positions labeled in Fig. 8.3.

Interestingly, for both polarizations and at all wavelengths, the emission enhancement of magnetic dipoles is roughly a factor 6 larger than for electric dipoles. Notably, in parallel to the similarity of the calculated electric and magnetic modal fields 20 nm above the waveguide (see chapter 4), the pattern of the calculated emission enhancement factor for a magnetic dipole (see Fig. 8.2b) is close to that for an electric dipole (see Fig. 8.2a) 20 nm above the waveguide, although at all wavelengths small differences are present. Combined the calculations shown in Fig. 8.2a and b highlight the tunability of linear electric and magnetic dipolar emitters offered by PhCWs.

8.3 Measured linear electric and magnetic dipole emission

To experimentally measure the emission of both electric and magnetic dipoles, we use the setup employed in chapter 7 and tune the continuous wave laser emission to 1575, 1585 and 1592 nm. Fig. 8.3a-f (left column) show the emission maps generated with x- and y-polarized illumination. Compared to the theoretical maps for a p_x and m_y (see Fig. 8.2), the maps measured with x-polarized illumination show slight differences. Specifically, we find that compared to the calculated maps, at 1575 nm the profile of the emission map between maxima is differently shaped (see Fig. 8.3a, b, arrow 1), at 1585 nm (see Fig. 8.3c, d, arrows 2 and 3) there is more intensity to the side of the waveguide and at 1592 nm (see Fig. 8.3e, f, arrow 4) we again observe a slight suppression of the emission at the waveguide center. Furthermore, a close examination of these figures reveals that at all wavelengths a slight left-right asymmetry is present[a] (for example arrows 1,3 indicate positions of high asymmetry). Interestingly, an asymmetry in the emission direction of *linear* dipoles, was recently reported for the combined emission of linear electric and magnetic dipoles and this asymmetry was also used to quantify the relative strength of these dipoles [23, 142, 143]. Hence, our observation of directional emission of a linear dipole (in conjunction with the work presented in chapters 4 and 5) suggests that we could use the emission maps measured with linear dipoles to quantify the relative electric and magnetic dipole strength of our probe.

[a] We stress that the directional emission of these linear dipoles is completely unrelated to the helicity of the emitting dipoles, which do not have a defined helicity because they are linear. Hence, this directional emission cannot be coupled to helicity.

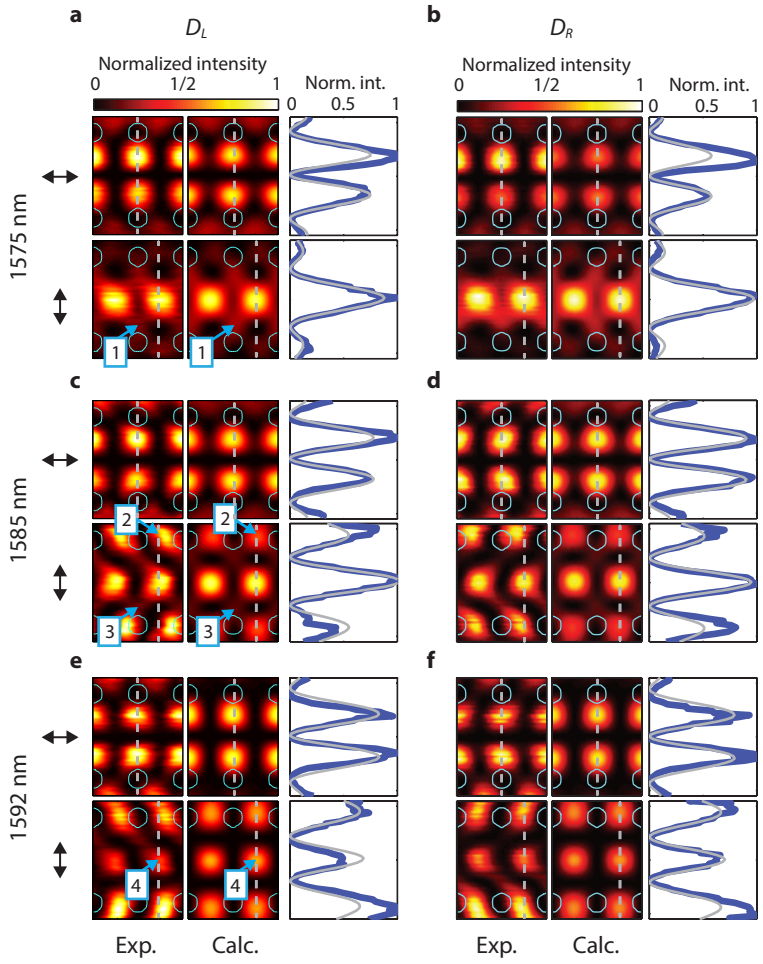

Figure 8.3: Measured linear electric and magnetic dipole emission. **a**, **c**, **e** (**b**, **d**, **f**) show the calculated and measured leftwards (rightwards) emission. In **a**-**f**, the top (bottom) row shows x- (y-) polarized emission. The left (middle) column of panels shows the measured (calculated) emission maps and the right column of panels shows line cuts taken along the gray dashed line. In the line traces, the blue (gray) line shows the experimental (calculated) intensity. Blue labels in **a**, **c**, **e** show positions where the calculated emission of a combined electric magnetic emitter particularly improves agreement with measurements. Black arrows indicate emission polarization. Blue circles indicate the holes in the PhCW.

To quantify the contribution of both electric and magnetic dipolar emission, we approximate our aperture probe as a combined electric [57] and magnetic [94] dipole source. Additionally, compared to chapter 4, we now measure closer to the surface of the crystal, where higher wavevectors are more abundant (see chapter 1). Because our probe cannot couple to some of these wavevectors, we now also need to take the finite resolution of our tip into account. Although we could invoke the optical reciprocity theorem to predict our measurements (see chapter 5), this would not provide extra experimental insight and the spatially different profiles of the electric and magnetic reciprocal fields make assigning a single strength to electric and magnetic dipole emission non-trivial. Hence, we fit our experimental measurements with a superposition of the electric and magnetic modal fields that we convoluted with a (210 nm diameter) disk. Specifically, we approximate the measured signal with

$$F_{L,R}\left(\mathbf{p}_x, \mathbf{m}_y; \mathbf{r}, \omega\right) = \left|\alpha E_x^{con}\left(\mathbf{r}, \omega\right) - \beta Z_0 H_y^{con}\left(\mathbf{r}, \omega\right)\right|^2, \tag{8.2a}$$

$$F_{L,R}\left(\mathbf{p}_y, \mathbf{m}_x; \mathbf{r}, \omega\right) = \left|\alpha E_y^{con}\left(\mathbf{r}, \omega\right) + \beta Z_0 H_x^{con}\left(\mathbf{r}, \omega\right)\right|^2, \tag{8.2b}$$

where Z_0 is the impedance of free space, $E_{x,y}^{con}\left(\mathbf{r}, \omega\right)$ and $H_{y,x}^{con}\left(\mathbf{r}, \omega\right)$ are the convoluted electric and magnetic modal field components and α and β are complex fitting parameters that quantify the relative electric and magnetic coupling strengths. As sketched in Fig. 8.4, rotating the injection polarization causes a sign change between the in-plane electric and magnetic fields. Therefore, Eqs. 8.2a and b differ by a minus sign that ensures a consistent phase between the electric and magnetic coupling for both injection polarizations.

The fits that are obtained using Eqs. 8.2a and b (middle panels of Fig. 8.3a-f) show good agreement with the measured fields when $|Z_0\beta| \,/\, |\alpha| = 0.9$ and $\phi_\beta - \phi_\alpha = -0.3\pi$ rad. This agreement is emphasized by the line traces shown in the right panels of Fig. 8.3a-f. Nonetheless, the emission along the waveguide center at 1592 nm remains somewhat suppressed compared to the calculations and at 1585 nm we observe slightly lower emission efficiency to the side of the waveguide. These differences could be explained by the increased interaction between the probe and the sample at these higher n_g's.

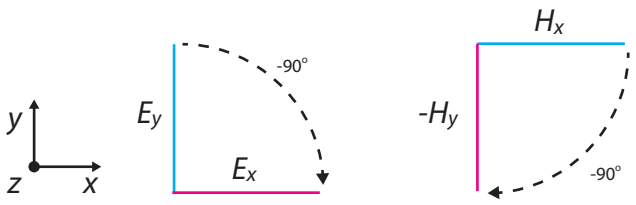

Figure 8.4: Rotating the illumination polarization. (left) Coordinate system. (middle, right) Blue (pink) lines show the field orientation for x- (y-) polarized illumination, respectively. Rotating the illumination polarization -90 degrees changes E_y to E_x (middle) and H_x to H_y (right).

8.4 Circular electric and magnetic dipole emission

We investigate the tunability of electric and magnetic dipole helicity-to-path coupling in PhCWs by injecting circularly polarized light at 1575, 1585 and 1592 nm. In appendix A we give an explanation of how we ensure circularly polarized illumination. The emission maps with circularly polarized light at all wavelengths (1575, 1585 and 1592 nm, shown in Fig. 8.5) reveal a clear left-right asymmetry in the emission direction. Furthermore, for all wavelengths, flipping either the direction of the detector path (i.e. monitoring either D_L or D_R) or dipole helicity results in a mirroring of the emission enhancement map about the middle of the waveguide ($y = 0$, dashed blue lines in Fig. 8.5). This asymmetry, which is indicative of helicity-to-path coupling, is excellently reproduced by the calculations for circularly polarized emission with a combined electric and magnetic emitter.

The helicity dependence of the emission directionality is further highlighted by line traces across the waveguide (taken along brown and pink dashed lines in the emission maps, and shown by blue and green lines in the right two panels of Fig. 8.5). These line traces, which are in excellent agreement with the calculations for all group indices, show that maxima for one helicity are turned into minima with a helicity reversal. Additionally, these line traces highlight that the positions at which we observe the left-right asymmetry shift between the shortest and the longest wavelength (from the brown to the pink dashed line in Fig. 8.5).

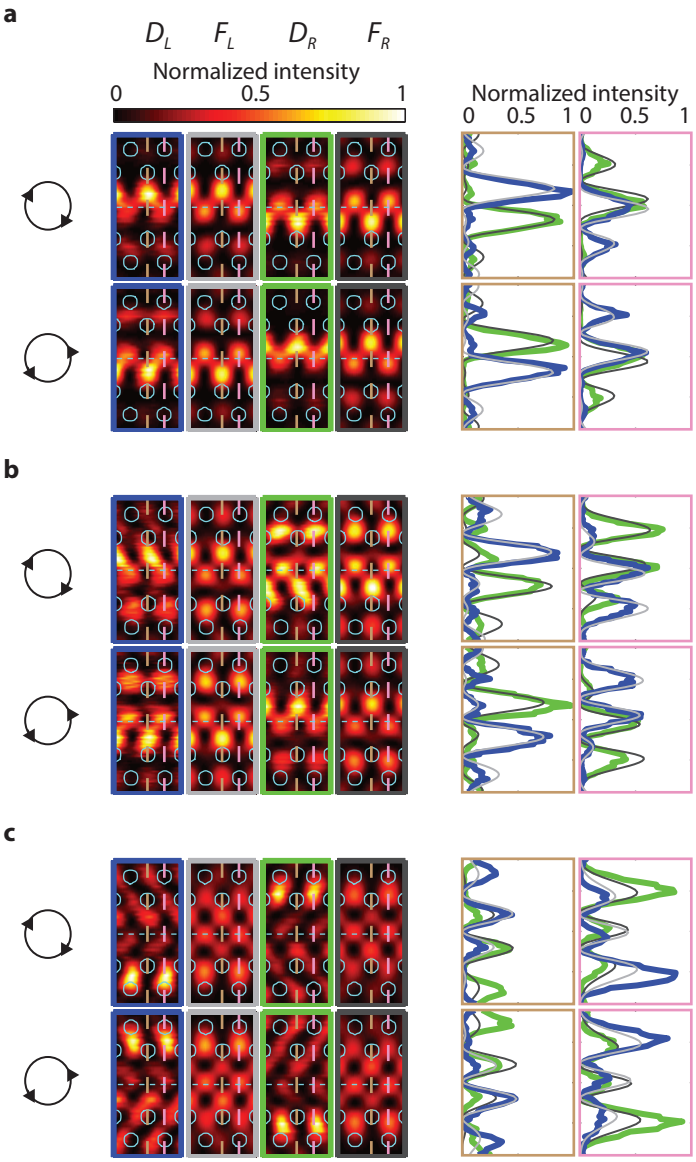

Figure 8.5: Circular dipole emission into the PhCW. Experimental (D_R and D_L) and calculated (F_L and F_R) emission maps for circularly polarized emission at 1575 nm (**a**), 1585 nm (**b**) and 1592 nm (**c**). The right two figure columns show line traces through the calculated and measured maps, along the dashed pink (right figures with line traces) and yellow (left figures with line traces) lines. Blue (green) lines show cuts through D_L (D_R). Light (dark) gray lines show cuts through F_L (F_R). Black arrows indicate the circular dipole handedness.

8.5 Control over helicity-to-path coupling offered by emission wavelength

8.5.1 Coupling strength

To quantify the coupling strength between helicity and path we compute the emission directionality for all wavelengths and positions above the waveguide via Eq. 7.3. In Fig. 8.6a, b, c we present the experimental maps obtained via Eq. 7.3 for wavelengths of 1575, 1585 and 1592 nm. These maps reveal that for all wavelengths large areas of high $|\eta_{dir}|$ are available. Furthermore, the observed coupling strengths closely match to the maps calculated for the combined electric and magnetic dipole emission (not shown). The line traces across the waveguide (right two columns of panels, Fig. 8.6a, b, c) both confirm this excellent agreement between experiment and theory and highlight the size of the areas where $|\eta| > 0.8$ (gray regions in line traces, Fig. 8.6a, b, c).

To gain more insight in the separate dipole emission that gives rise to the maps in Fig. 8.6a, b, c, we show contours where $|\eta_{dir}| > 0.8$ for the emission from purely electric and magnetic dipoles in Fig. 8.6g, h, i. These figures reveal large areas of strong helicity-to-path coupling at all wavelengths that are very similar between the electric and magnetic dipoles. Notably, we observe that for increasing n_g these areas of highly directional emission move away from the waveguide center to the extend that they nearly disappear at the waveguide center. Importantly, large regions with close to unity values of $|\eta_{dir}|$ that we find at all wavelengths (Fig. 8.6g, h, i) highlight that emitter spin and photon path can be deterministically coupled on a PhCW waveguide for different wavelengths and mode profiles.

8.5.2 Coupling efficiency

For our approach to dipole helicity to pathway coupling to be a viable route toward on-chip quantum technology, not only the directionality but also the emission rate itself needs to be maximized. Hence, analogue to chapter 7 for 1575 nm emission, we now extract η for emission at 1575, 1585 and 1592 nm according to Eq. 7.4. Strikingly, in the measurements (shown the left panel of Fig. 8.6d, e, f) at these higher n_g's, regions of highly directional coupling appear away from the center of the waveguide [see Fig. 8.6e ($n_g = 40$) and Fig. 8.6f ($n_g = 120$)]. Furthermore, as can be observed from the line cuts

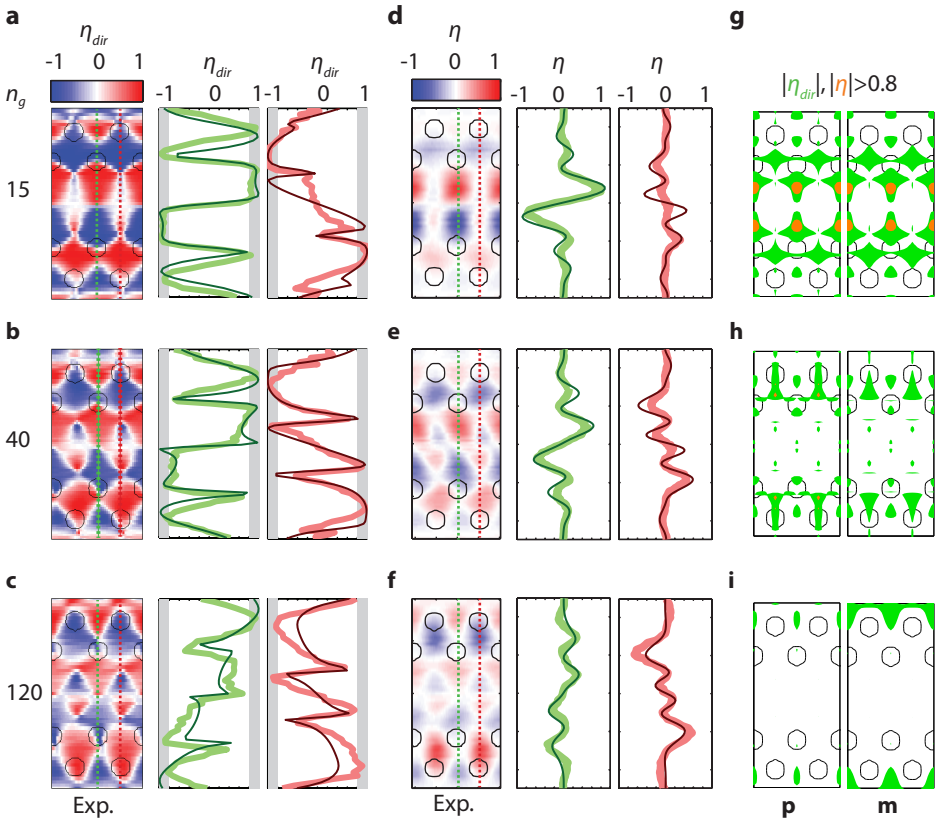

Figure 8.6: Emission directionality. **a**, **b**, **c** (**d**, **e**, **f**) Experimentally determined η_{dir} (η) maps (left panels), and line traces (middle and right panel) along the red and green lines in the left panel. **g**, **h**, **i** Contours indicate regions where $|\eta| > 0.8$ (orange) and $|\eta_{dir}| > 0.8$ (green) for the emission of a purely electric (left panel) and magnetic (right panel) dipole. In **a**-**f** black circles show contours of the holes in the PhCW.

(shown the right panel of Fig. 8.6d, e, f) as n_g increases, the position of $|\eta|_{max}$ shifts from the central region of the waveguide, to the area of the holes (from the green to the red dashed line). These observations are in excellent agreement with the line traces shown in that figure. Furthermore, $|\eta|_{max}$ decreases as n_g increases, from 0.8 ± 0.1 at 1575 nm, to 0.6 ± 0.1 at 1585 nm, and 0.7 ± 0.1 at 1592 nm. The directional coupling efficiency decreases due of the combined emission of electric and magnetic dipoles, which are projected onto (slightly) different modal fields (see chapter 6). Furthermore, for the higher n_g's the maxima in directionality and circular dipole emission enhancement are no longer located at the same position.

To gain more insight in the possibility of spin-to-path coupling of purely electric and magnetic dipoles we show the regions where $|\eta| > 0.8$ for purely electric and magnetic emitters in Fig. 8.6g, h, i. We observe that the area enclosed by these regions decreases as a function of n_g. That is, in Fig. 8.6h regions of $|\eta| > 0.8$ are available for electric, but absent for magnetic dipoles.

A comparison between the contours of $|\eta| > 0.8$ and $|\eta_{dir}|\, 0.8$ in Fig. 8.6g, h, i reveals that at all wavelengths the contours of $|\eta_{dir}|$ enclose much larger areas then those for $|\eta|$. Hence, although emission might not equal the maximal emission at higher n_g, helicity and path are still strongly coupled.

8.6 Geometric control of coupling strength

To explore the possibility of achieving high $|\eta(\omega)|$ and n_g simultaneously, we calculate the maximally available $|\eta(\omega)|$ for a larger wavelength range and investigate the effect of a slight change in the PhCW on $|\eta(\omega)|_{max}$. We begin by computing $|\eta(\omega)|_{max}$ for each calculated PhCW mode (red lines, Fig. 8.7a, b). These calculations reveal that the PhCW offers near-unity helicity-to-path coupling for both electric and magnetic dipoles at wavelengths shorter than 1575 nm. Interestingly, at longer wavelengths $|\eta(\omega)|_{max}$ first drops, then recovers, before dropping near the PhCW mode-gap [with the magnetic dipole (thin lines, Fig. 8.7b) dropping slightly faster than the electric dipole (thick lines, Fig. 8.7b)]. This drop to zero for both emitter types can be understood, because, at the mode gap, the PhCW mode is a standing wave [33]. Due to the structural symmetry this standing wave is equally left- and rightwards propagating and hence cannot couple helicity to path. A precise investigation of how the maximal coupling

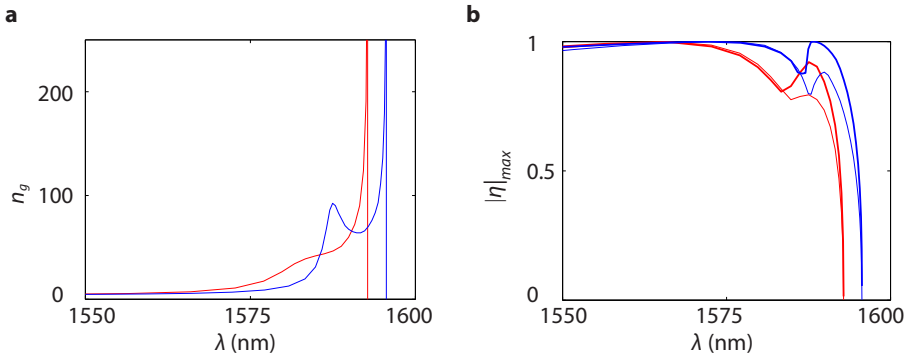

Figure 8.7: Coupling efficiency as a function of wavelength. a Dispersion relation of the PhCW modes with the designed (blue line) and used geometry (red line). **b** Coupling strength as a function of wavelength for emission with an electric (thick lines) and with a magnetic (thin lines) for the PhCW with the changed (blue lines) and with the experimental geometry (red lines).

strength and position evolve with wavelength remains interesting for future studies.

To obtain an idea of the effect of the PhCW geometry on $|\eta(\omega)|_{max}$, we calculate $|\eta(\omega)|_{max}$ for a slightly different PhCW geometry. That is, we repeat the calculations with a 220 nm thick slab (corresponding to a 20 nm increase in thickness) and 120 nm radius (a 10 nm increase) holes (blue lines Fig. 8.7a, b), while keeping the positions of the holes fixed. For this geometry we observe a shift of the band structure towards larger wavelengths (blue line, Fig. 8.7a). Consequently, we expect that this structure enables higher $|\eta(\omega)|_{max}$ at longer wavelengths. Figure 8.7b shows that, indeed, the tuned PhCW geometry allows for larger $|\eta(\omega)|_{max}$, for both electric and magnetic dipoles. Specifically, we find that the new geometry enables near-unity helicity to path coupling for both electric and magnetic dipoles over a 30 nm window.

8.7 Conclusions

In this chapter we have experimentally demonstrated that dipole helicity and path can be coupled in a PhCW over a range of wavelengths, which corresponds to a tenfold emission enhancement. Furthermore, we have

shown that this tunability can be achieved for both electric and magnetic dipoles. Because helicity of these dipoles is associated with the spin change of quantum emitters, our work paves the way for a controlled coupling of spin and path. This control is of vital importance for the practical realization of a scalable solid-state to photonic-qubit interface.

9

An on-chip sensor for circular dichroism

In this chapter we investigate the possibility of applying the understanding gained in this thesis for the development of a magnetic circular dichroism sensor. Specifically, we propose to use the ellipticity of the near fields of a ridge waveguide to probe a circularly dichroic compound. Furthermore, we suggest a Mach-Zehnder like scheme in which this waveguide could be incorporated to increase the sensitivity to the circular dichroism. We also highlight some of the opportunities and challenges in the application of this approach for the development of circular dichroism sensors.

9.1 Introduction

Spectroscopic data of molecules is of huge importance for their identification and it provides a useful test of the validity of proposed models for molecular structure and bonding [144]. In the context of molecular structure and bonding, magnetic circular dichroism (MCD) can be used to identify weakly visible or overlapping energy bands, which are invisible to common absorption techniques that use linearly polarized light [145, 146, 147]. Techniques exploiting MCD are particularly useful in the investigation of bioinorganic molecules that play a key role in biological redox processes such as photosynthesis or respiration [145, 146, 147].

In MCD molecules are subjected to a static magnetic field and probed with circularly polarized light. Like the orbital angular momentum changing transitions discussed in chapter 7 and 8, a circular electric field can excite transitions to specific spin states [148]. These transitions between spin states occur at different wavelengths and the differential absorption at a given wavelength is typically defined as

$$\Delta A(\lambda) = \frac{A_{LH}(\lambda) - A_{RH}(\lambda)}{A_{LH}(\lambda) + A_{RH}(\lambda)}, \tag{9.1}$$

where $A_{LH,RH}(\lambda)$ are the absorptions for left- and righthanded circular electric fields, respectively. In an ideal measurement, the optical field orientation and intensity are controlled such that ΔA is maximal and ΔA is resolved with maximal sensitivity.

At present, techniques that probe MCD use far-field radiation and require large experimental setups that can generate huge (up to 7 Tesla) magnetic fields [148]. Furthermore, these detection schemes typically use complex and expensive electronics and optics to measure the absorption for both optical polarizations and subtract these. Conversely, an ideal setup for the detection of MCD, would consist of a simple detection scheme, which delivers high sensitivities.

We propose to use the circular evanescent field above a Si_3N_4 ridge waveguide (sketched in Fig. 9.1a) to sensitively probe MCD of the molecules in suspension above the waveguide. Over the last decades, there has been a flurry of research in such nanophotonic waveguiding sensors, which can greatly enhance the sensitivity to nearby molecules up to several picograms per mm^2 [149, 150]. However, the possibility of using these waveguides to probe circular dichroism has remained unexplored.

In MCD the static magnetic field is oriented perpendicular to the plane in which the electric field is circular. For example, the ability of an electric optical field to drive a (circular) electric transition dipole mediated transition in the presence of a static magnetic field along x (B_x) is proportional to [148]

$$A_{LH,RH}(\lambda) \propto B_x \left|\alpha^*_{yz}(\lambda) \cdot \mathbf{E}\right|^2, \tag{9.2}$$

where $\alpha_{yz}(\lambda) \propto \hat{\mathbf{y}} \pm i\hat{\mathbf{z}}$ depending on the helicity of the transition dipole. The differential absorption of left- and righthanded electric fields is proportional to $B_x \mathrm{Re}\{iE_yE_z\}$ and is maximal for circular electric fields. Recently, it was shown that completely circular electric fields can even be

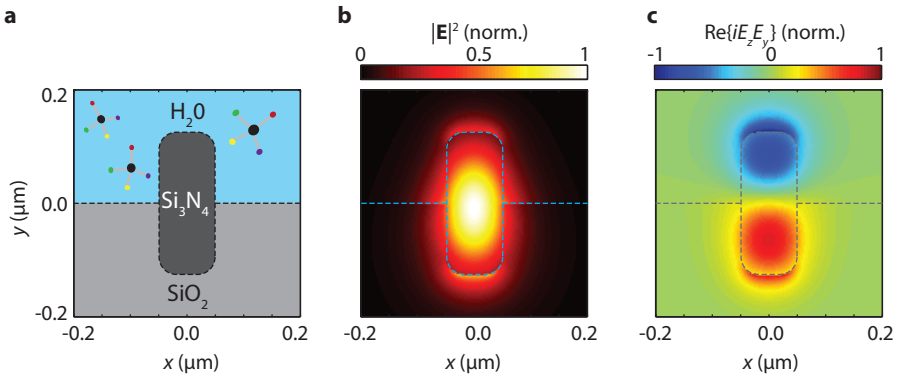

Figure 9.1: Nanophotonic ridge waveguide. **a** Sketch of the ridge waveguide geometry. The waveguide is 250 nm high and 100 nm wide. **b** Calculated $|\mathbf{E}|^2$ distribution in and near the waveguide. Dashed blue line indicate materials interfaces. **c** Calculated normalized $\mathrm{Re}\{iE_yE_z\}$ in and near the waveguide. Dashed gray lines indicate interfaces.

obtained in the evanescent field of the fundamental mode in tapered optical fibers [139, 135]. In general, although for example the electric field of a TE mode is completely linearly polarized on certain axes or planes of structural symmetry, away from these axes or planes the field can elliptical or even circular.

At 1550 nm (a typical wavelength for MCD studies [148]) our ridge waveguide supports a single TM mode, with an effective wavelength of $k_{eff} = 1.6k_0$. The geometry of the waveguide is chosen to be as symmetric as possible. The bottom half of the Si_3N_4 waveguide is surrounded by SiO_2, which has roughly the same index as the aqueous solution that surrounds the top half. As depicted by Fig. 9.1a, a significant fraction of the light distribution is available in the water above this waveguide, although the vast majority of the light is inside the waveguide. In addition to sufficient optical amplitude, the sensitive detection of MCD requires a non-zero ellipticity of the evanescent field that is oriented perpendicular to the applied magnetic field along x. Strikingly, the calculation of $\mathrm{Re}\{iE_yE_z\}$ presented in Fig. 9.1c reveals that only one helicity of the electric field is present in the water. Furthermore, the helicity of this electric field is reversed with a change of propagation direction of the mode (see also chapter 7, calculations not shown). Hence, a difference in absorption of light propa-

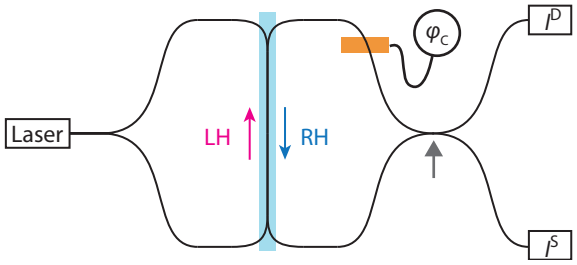

Figure 9.2: Proposed on-chip MCD detection scheme. Black lines indicate the waveguide paths. In the blue shaded area the waveguide is covered with the suspension, which contains the investigated molecules. All waveguide junctions are 50/50 beamsplitters, at the beamsplitter indicated by the gray arrow, on the LH and RH indicate the right and left handed helicity of the fields above the waveguide. The heating element is indicated in gold.

gating in opposite directions in the waveguide could be used as a probe for MCD. We note that the waveguide geometry that we present can still be optimized. Such an optimization would entail a maximization of the ratio $\mathrm{Re}\{iE_yE_z\}/|\mathbf{E}|^2$ in the area above the waveguide.

In Fig. 9.2 we present a Mach-Zehnder like scheme in which the waveguides could be incorporated to enable the efficient detection of MCD. In this scheme two detectors measure the interference between the light from two equal length paths, which are both exposed to the investigated compound. Through the Kramers-Kronig relations a differential absorption between the two paths is related to a difference in the real part of the refractive index [151]. Such a difference in refractive index causes a difference in the phase pick up between the to paths, which changes the intensity of the interference signal on the two detectors. Mathematically, the optical intensity on the detectors is given by

$$\begin{aligned} I^S(\lambda) =& I_{RH}(\lambda) + I_{LH}(\lambda) + \\ & 2\sqrt{I_{RH}(\lambda)I_{LH}(\lambda)}\cos(\phi_{LH}(\lambda) - \phi_{RH}(\lambda) + \pi + \phi_C), \end{aligned} \tag{9.3a}$$

$$\begin{aligned} I^D(\lambda) =& I_{RH} + I_{LH} + \\ & 2\sqrt{I_{RH}(\lambda)I_{LH}(\lambda)}\cos(\phi_{LH}(\lambda) - \phi_{RH}(\lambda) + \phi_C), \end{aligned} \tag{9.3b}$$

where $I_{LH,RH}(\lambda)$ and $\phi_{LH,RH}(\lambda)$ are the intensities and phase changes due to the absorption of right and left handed light and $\phi(C)$ is a voltage

controlled phase shift that can be added to one of the channels. Due to the last beamsplitter (gray arrow, Fig. 9.2) one of the two inputs picks up an additional π phase shift when it contributes to I^D .

In this detection scheme the differential absorption between the LH and RH channels is much smaller than their total absorption, hence I^S describes a conventional absorption measurement. On the other hand I^D is zero when $\phi_{LH} = \phi_{RH}$, and no voltage is applied. Importantly, any difference in absorption will result a non-zero I^D, enabling a potentially extremely sensitive detection of MCD.

Additionally, a measurement of MCD requires knowledge of which handedness is absorbed most, and due to the symmetry of a cosine the helicity cannot be resolved without an additional mechanism. To resolve this issue, we propose to add a controlled phase difference (for example by means of heating or free carrier injection) to one of the two channels. If the phase of one of the input channels can be changed with a known sign, and if we assume that the $|\phi_{LH} - \phi_{RH}| < \pi$, the increase or decrease of the signal in I^D due to an applied voltage will be linked to the helicity of the light that is absorbed most. A precise estimation of the sensitivity gain offered by the proposed detection scheme requires a further investigation. However, we stress that even a bare nanophotonic waveguide can enhance the sensitivity to molecular compounds [152], and that by the incorporating the waveguide in a Mach-Zehnder interferometer this sensitivity can be further enhanced by several orders of magnitude [149, 150, 153].

In conclusion, the proposed nanophotonic waveguide detection scheme could improve the sensing of MCD on chip. In this manner this platform could benefit researchers and companies aiming to resolve the structures of the bioinorganic molecules. We note that for measurements over a broad spectral range, Si_3N_4 waveguides could also enable MCD measurements in the visible part of the spectrum. We also note that it is important to develop a future sensor such that both the modal field distribution and the behavior of the beamsplitters are controlled throughout the spectral range.

A

Control over emission polarization

One of the benefits of using a NSOM to mimic the emission of a dipolar emitter is that this setup allows a high degree of the control over the dipole orientation. Here, we use the $\lambda/2$, $\lambda/4$ and LC wave plates shown in Fig. 7.3c (main text) to control the field orientation beneath our NSOM tip. The LC-plate (Thorlabs LCC1113-C) that has a voltage controllable phase difference between its birefringent axes, is only used in experiments where we mimic a circular dipole.

We start by orienting our half- and quarter-wave plates analogue to the procedure used in collection mode to achieve linear ($\hat{\mathbf{x}}$) polarization beneath the probe apex. In this situation (black dot on the Poincaré spare sketched in Fig. A.1a), we know that before the $\lambda/4$, the polarization of the light is aligned with one of the birefringent axes of the combined $\lambda/4$ and fiber system. Therefore, to measure the emission of a $\hat{\mathbf{y}}$ oriented dipole, we rotate the $\lambda/2$ by 45° to align our polarization to the other axis of the combined system (moving along the green circle to VP, Fig. A.1a).

We now set out to show that we can control the orientation of our dipole source to create circularly (and elliptically) polarized dipoles. To mimic a circularly polarized dipole we firstly create equal amplitude x- and y-components of the probe dipole and subsequently ensure that they oscillate in quadrature. Equal amplitude in-plane dipoles are straightforwardly

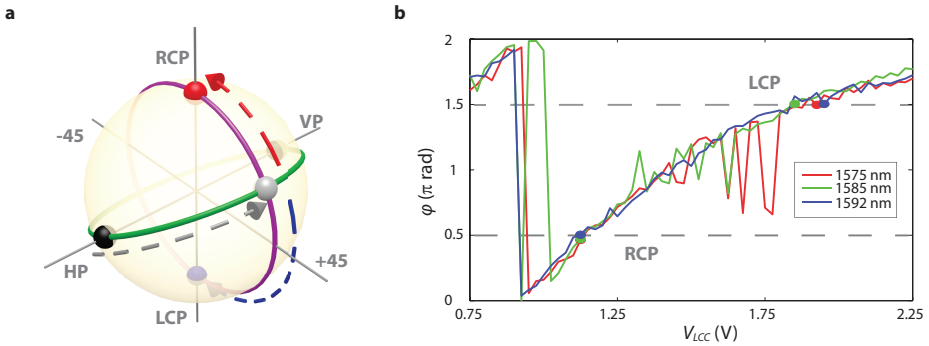

Figure A.1: Achieving circular dipole orientation. **a** Poincaré sphere, with annotated orientations of the dipoles that emits into the PhCW. Intersections between the sphere and the gray axes are labeled with the corresponding dipole orientations: linear polarized x, y (HP,VP), linearly diagonally polarized (+45,-45), and left- and righthanded circular polarized (LCP,RCP). The green (and purple) line indicates the effect of rotating the $\lambda/2$ (and scanning the voltage on the LC) plate. **b** Relation between voltage from our liquid crystal controller (V_{LCC}) and the resulting phase (ϕ) described in the text.

achieved by rotating the $\lambda/2$ by 22.5° (move along gray dashed arrow to the gray dot, Fig. A.1a). However, at this point in the experiment the birefringence of the combined fiber and $\lambda/4$ system is unknown. That is, the position of dipole orientation on the purple circle drawn in Fig. A.1a is unknown at this at this point. Consequently, to achieve circular polarization we need to scan the phase between the x and y oriented dipoles to ensure circular polarization. To achieve circular dipole orientations, we vary the phase between the equal amplitude x- and y-components of the probe dipole using the LC-plate. Specifically, after we ensure that the birefringent axes of this waveplate are aligned to the axes of the combined fiber and system, we scan the phase difference between the two orthogonal components of the probe dipole with the LC-plate. In this manner the dipole orientation moves along the purple line on the Poincaré sphere sketched in Fig. A.1a.

For each voltage (V_{LCC}) that we apply to the LC-plate, we find the phase difference (ϕ) between the horizontally ($HP(\mathbf{r},\omega) = \alpha E_x^{con}(\mathbf{r},\omega) - \beta Z_0 H_y^{con}(\mathbf{r},\omega)$) and vertically polarized dipole injection ($VP(\mathbf{r},\omega) = \alpha E_y^{con}(\mathbf{r},\omega) + \beta Z_0 H_x^{con}(\mathbf{r},\omega)$) by fitting superpositions

$$F_{L,R}^{\mathbf{p},\mathbf{m}}(V_{LCC},\mathbf{r},\omega) = \left| HP_{L,R}(\mathbf{r},\omega) + e^{i\phi(V_{LCC})} VP_{L,R}(\mathbf{r},\omega) \right|^2 \tag{A.1}$$

to our experimental emission maps on the left and right detector at that recorded at V_{LCC}, using the α and β that we found in Sec. 8.3. Fig. A.1b shows that the obtained via this approach show excellent agreement between the three wavelengths (1575, 1585 and 1592 nm). Furthermore, we find that we can sample an entire 2π phase difference. Having established this calibration, our approach is straightforwardly extended to mimic any complex dipole orientation. To measure the emission of circularly polarized dipoles, we pick the values of ϕ closest to $\pi/2$ and $3\pi/2$ for each wavelength (move along blue and red dashed arrows to blue and red spheres in Fig. A.1b).

References

[1] Corning Incorporated. *Optical fiber spans 30 years* http://www.corning.com/ (2010).

[2] International Energy Agency. *Technology roadmap: Solar photovoltaic energy* http://www.iea.org/ (2014).

[3] U.S. Dept. of Energy. *Solid-state lighting research and development multi-year program plan* http://energy.gov/eere/office-energy-efficiency-renewable-energy (2014).

[4] A. Polman and H. A. Atwater. *Photonic design principles for ultrahigh-efficiency photovoltaics.* Nat. Mater. **11**, 174 (2012).

[5] J. L. O'Brien, A. Furusawa and J. Vuckovic. *Photonic quantum technologies.* Nature Photon. **3**, 687 (2009).

[6] D. M. Beggs, *et al. Ultrafast tunable optical delay line based on indirect photonic transitions.* Phys. Rev. Lett. **108** (2012).

[7] X. Fan, *et al. Sensitive optical biosensors for unlabeled targets: A review.* Anal. Chim. Acta **620**, 8 (2008).

[8] L. Novotny and B. Hecht. *Principles of nano-optics.* Cambridge university press (2012).

[9] J. D. Jackson. *Classical electrodynamics, (Ch. 6)*, Wiley New York (1962).

[10] B. Wild, *et al. Temperature tuning of the optical properties of planar photonic crystal microcavities.* Appl. Phys. Lett. **84**, 846 (2004).

[11] K. Yoshino, *et al. Temperature tuning of the stop band in transmission spectra of liquid-crystal infiltrated synthetic opal as tunable photonic crystal.* Appl. Phys. Lett. **75**, 932 (1999).

[12] E. Abbe. *Beiträge zur theorie des mikroskops und der mikroskopischen wahrnehmung.* Arch. Mikrosk. Anat. **9**, 413 (1873).

[13] R. Carminati. *Optics beyond the diffraction limit* https://www.institut-langevin.espci.fr/ (2014).

[14] M. Gustafsson. *Surpassing the lateral resolution limit by a factor of two using structured illumination microscopy.* J. Microsc. (Oxf) **198**, 82 (2000).

[15] E. Betzig, *et al. Imaging intracellular fluorescent proteins at nanometer resolution.* Science **313**, 1642 (2006).

[16] A. Kinkhabwala, *et al. Large single-molecule fluorescence enhancements produced by a bowtie nanoantenna.* Nature Photon. **3**, 654 (2009).

[17] E. Verhagen, *et al. Nanowire plasmon excitation by adiabatic mode transformation.* Phys. Rev. Lett. **102**, 203904 (2009).

[18] J. van de Groep and A. Polman. *Designing dielectric resonators on substrates: Combining magnetic and electric resonances.* Opt. Express **21**, 26285 (2013).

[19] D. Schurig, *et al. Metamaterial electromagnetic cloak at microwave frequencies.* Science **314**, 977 (2006).

[20] D. Smith, J. Pendry and M. Wiltshire. *Metamaterials and negative refractive index.* Science **305**, 788 (2004).

[21] J. A. Schuller, *et al. Dielectric metamaterials based on electric and magnetic resonances of silicon carbide particles.* Phys. Rev. Lett. **99**, 107401 (2007).

[22] C. M. Dodson and R. Zia. *Magnetic dipole and electric quadrupole transitions in the trivalent lanthanide series: Calculated emission rates and oscillator strengths.* Phys. Rev. B **86**, 125102 (2012).

[23] N. Rotenberg, *et al. Magnetic and electric response of single subwavelength holes.* Phys. Rev. B **88**, 241408 (2013).

[24] P. Spinelli and A. Polman. *Light trapping in thin crystalline si solar cells using surface mie scatterers.* IEEE J. Photovolt. **4**, 554 (2014).

[25] H. Gersen, *et al. Real-space observation of ultraslow light in photonic crystal waveguides.* Phys. Rev. Lett. **94**, 73903 (2005).

[26] T. Baba. *Slow light in photonic crystals.* Nature Photon. **2**, 465 (2008).

[27] Y. A. Vlasov, *et al. Active control of slow light on a chip with photonic crystal waveguides.* Nature **438**, 65 (2005).

[28] A. Opheij, *et al. Ultracompact (3 μm) silicon slow-light optical modulator.* Sci. Rep. **3**, 3546 (2013).

[29] J. Leuthold, C. Koos and W. Freude. *Nonlinear silicon photonics.* Nature Photon. **4**, 535 (2010).

[30] B. Corcoran, *et al. Green light emission in silicon through slow-light enhanced third-harmonic generation in photonic-crystal waveguides.* Nature Photon. **3**, 206 (2009).

[31] R. B. L. C. Petit. *Electromagnetic theory of gratings.* Springer-Verlag (1980).

[32] J. D. Jackson. *Classical electrodynamics, (Ch. 8)*, Wiley New York (1962).

[33] J. D. Joannopoulos, *et al. Photonic crystals: molding the flow of light.* Princeton university press (2011).

[34] N. W. M. N. D. Ashcroft. *Solid state physics.* Holt, Rinehart and Winston, New York (1976).

[35] F. Zolla. *Foundations of Photonic Crystal Fibres, (Ch. 2)*, World Scientific (2005).

[36] L. Rayleigh. *On the maintainance of vibrations by forces of double frequency and on the propagation of waves through a medium endowed with a periodic structure.* Plilosophical Magazin **24**, 145 (1917).

[37] E. Yablonovitch. *Inhibited spontaneous emission in solid-state physics and electronics.* Phys. Rev. Lett. **58**, 2059 (1987).

[38] S. Johnson and J. Joannopoulos. *Block-iterative frequency-domain methods for maxwell's equations in a planewave basis.* Opt. Express **8**, 173 (2001).

[39] D. M. Beggs, *et al. Ultrafast tilting of the dispersion of a photonic crystal and adiabatic spectral compression of light pulses.* Phys. Rev. Lett. **108**, 033902 (2012).

[40] T. F. Krauss. *Slow light in photonic crystal waveguides.* J. of Phys. D: Appl. Phys. **40**, 2666 (2007).

[41] T. Krauss, R. DeLaRue and S. Brand. *Two-dimensional photonic-bandgap structures operating at near infrared wavelengths.* Nature **383**, 699 (1996).

[42] R. J. P. Engelen, *et al. Subwavelength structure of the evanescent field of an optical bloch wave.* Phys. Rev. Lett. **102**, 023902 (2009).

[43] L. Novotny and N. van Hulst. *Antennas for light.* Nature Photon. **5**, 83 (2011).

[44] E. M. Purcell. *Modification of spontaneous emission.* Phys. Rev. **69**, 681 (1946).

[45] G. Fowles. *Introduction to Modern Optics.* Dover Publications (2012).

[46] R. Sprik, B. Van Tiggelen and A. Lagendijk. *Optical emission in periodic dielectrics.* Europhys. Lett. **35**, 265 (1996).

[47] S. Hughes. *Enhanced single-photon emission from quantum dots in photonic crystal waveguides and nanocavities.* Opt. Lett. **29**, 2659 (2004).

[48] P. Lodahl, *et al. Controlling the dynamics of spontaneous emission from quantum dots by photonic crystals.* Nature **430**, 654 (2004).

[49] E. Yablonovitch. *Photonic band-gap structures.* Journal of the Optical Society of America B-Optical Physics **10**, 283 (1993).

[50] E. Synge. *A suggested method for extending microscopic resolution into the ultra-microscopic region.* The London, Edinburgh, and Dublin Philosophical Magazine and Journal of Science **6**, 356 (1928).

[51] L. Novotny. *The history of near-field optics. Prog. Optics* **50**, 137 (2007).

[52] K. Karrai and R. D. Grober. *Piezoelectric tip-sample distance control for near field optical microscopes.* Appl. Phys. Lett. **66**, 1842 (1995).

[53] J. Veerman, *et al. High definition aperture probes for near-field optical microscopy fabricated by focused ion beam milling.* Appl. Phys. Lett. **72**, 3115 (1998).

[54] D. Pohl, W. Denk and M. Lanz. *Optical stethoscopy: Image recording with resolution λ/20.* Appl. Phys. Lett. **44**, 651 (1984).

[55] E. Betzig, *et al. Breaking the diffraction barrier: Optical microscopy on a nanometric scale.* Science **251**, 1468 (1991).

[56] E. Betzig and R. J. Chichester. *Single molecules observed by near-field scanning optical microscopy.* Science **262**, 1422 (1993).

[57] C. Chicanne, *et al. Imaging the local density of states of optical corrals.* Phys. Rev. Lett. **88**, 097402 (2002).

[58] G. Colas des Francs, *et al. Relationship between scanning near-field optical images and local density of photonic states.* Chem. Phys. Lett. **345**, 512 (2001).

[59] R. C. Reddick, R. J. Warmack and T. L. Ferrell. *New form of scanning optical microscopy.* Phys. Rev. B **39**, 767 (1989).

[60] M. Specht, *et al. Scanning plasmon near-field microscope.* Phys. Rev. Lett. **68**, 476 (1992).

[61] J. T. Robinson, S. F. Preble and M. Lipson. *Imaging highly confined modes in sub-micron scale silicon waveguides using transmission-based near-field scanning optical microscopy.* Opt. Express **14**, 10588 (2006).

[62] J. Dorfmüller, *et al. Near-field dynamics of optical yagi-uda nanoantennas.* Nano Lett. **11**, 2819 (2011).

[63] R. L. Olmon, *et al. Determination of electric-field, magnetic-field, and electric-current distributions of infrared optical antennas: A near-field optical vector network analyzer.* Phys. Rev. Lett. **105**, 167403 (2010).

[64] M. Schnell, *et al. Phase-resolved mapping of the near-field vector and polarization state in nanoscale antenna gaps.* Nano Lett. **10**, 3524 (2010).

[65] A. J. Meixner, M. A. Bopp and G. Tarrach. *Direct measurement of standing evanescent waves with a photon-scanning tunneling microscope.* Appl. Opt. **33**, 7995 (1994).

[66] M. Burresi. *Nanoscale investigation of light-matter interactions mediated by magnetic and electric coupling.* Ph.D. thesis, University of Twente (2009).

[67] M. Burresi, *et al. Observation of polarization singularities at the nanoscale.* Phys. Rev. Lett. **102**, 033902 (2009).

[68] H. Gersen, *et al. Direct observation of bloch harmonics and negative phase velocity in photonic crystal waveguides.* Phys. Rev. Lett. **94**, 123901 (2005).

[69] D. van Labeke and D. Barchiesi. *Probes for scanning tunneling microscopy - a theoretical comparison.* J. Opt. Soc. Am. A **10**, 2193 (1993).

[70] H. Kihm, *et al. Bethe-hole polarization analyser for the magnetic vector of light.* Nat. Commun. **2**, 451 (2011).

[71] A. Roberts. *Small-hole coupling of radiation into a near-field probe.* J. Appl. Phys. **70**, 4045 (1991).

[72] J. Veerman, *et al. Single molecule mapping of the optical field distribution of probes for near-field microscopy.* J. Microsc. (Oxf) **194**, 477 (1999).

[73] W. L. Barnes, A. Dereux and T. W. Ebbesen. *Surface plasmon subwavelength optics.* Nature **424**, 824 (2003).

[74] F. López-Tejeira, *et al. Efficient unidirectional nanoslit couplers for surface plasmons.* Nature Phys. **3**, 324 (2007).

[75] N. Rotenberg, *et al. Plasmon scattering from single subwavelength holes.* Phys. Rev. Lett. **108**, 127402 (2012).

[76] P. B. Johnson and R. W. Christy. *Optical constants of the noble metals.* Phys. Rev. B **6**, 4370 (1972).

[77] C. F. Bohren and D. R. Huffman. *Absorption and scattering of light by small particles.* John Wiley & Sons (1983).

[78] K. Sakoda. *Optical properties of photonic crystals*, Springer (2005).

[79] M. Burresi, *et al. Probing the magnetic field of light at optical frequencies.* Science **326**, 550 (2009).

[80] P. Uebel, *et al. Polarisation-resolved near-field mapping of a coupled gold nanowire array.* Opt. Express **20**, 28409 (2012).

[81] M. Schnell, *et al. Controlling the near-field oscillations of loaded plasmonic nanoantennas.* Nature Photon. **3**, 287 (2009).

[82] P. Venugopalan, *et al. Polarization-sensitive characterization of the propagating plasmonic modes in silver nanowire waveguide on a glass substrate with a scanning near-field optical microscope.* Opt. Express **21**, 15247 (2013).

[83] I. Sersic, *et al. Electric and magnetic dipole coupling in near-infrared split-ring metamaterial arrays.* Phys. Rev. Lett. **103**, 213902 (2009).

[84] F. J. Garcia-Vidal, *et al. Light passing through subwavelength apertures.* Rev. Mod. Phys. **82**, 729 (2010).

[85] S. Bozhevolnyi, *et al. Channel plasmon subwavelength waveguide components including interferometers and ring resonators.* Nature **440**, 508 (2006).

[86] V. M. Shalaev. *Optical negative-index metamaterials.* Nature Photon. **1**, 41 (2007).

[87] D. Smith, *et al. Composite medium with simultaneously negative permeability and permittivity.* Phys. Rev. Lett. **84**, 4184 (2000).

[88] A. V. Kildishev, A. Boltasseva and V. M. Shalaev. *Planar photonics with metasurfaces.* Science **339**, 1232009 (2013).

[89] T. Ergin, *et al. Three-dimensional invisibility cloak at optical wavelengths.* Science **328**, 337 (2010).

[90] M. Ren, *et al. Giant nonlinear optical activity in a plasmonic metamaterial.* Nat. Commun. **3** (2012).

[91] C. M. Soukoulis and M. Wegener. *Past achievements and future challenges in the development of three-dimensional photonic metamaterials.* Nature Photon. **5**, 523 (2011).

[92] T. H. Taminiau, *et al. Quantifying the magnetic nature of light emission.* Nat. Commun. **3**, 979 (2012).

[93] E. Devaux, *et al. Local detection of the optical magnetic field in the near zone of dielectric samples.* Phys. Rev. B **62**, 10504 (2000).

[94] D. Denkova, *et al. Near-field aperture-probe as a magnetic dipole source and optical magnetic field detector.* Preprint at http://arxiv.org/abs/1406.7827 (2014).

[95] H. W. Kihm, *et al. Optical magnetic field mapping using a subwavelength aperture.* Opt. Express **21**, 5625 (2013).

[96] G. Monteath. *Applications of the electromagnetic reciprocity principle.* International series of monographs on electromagnetic waves. Pergamon Press (1973).

[97] J. Porto, R. Carminati and J. Greffet. *Theory of electromagnetic field imaging and spectroscopy in scanning near-field optical microscopy.* J. Appl. Phys. **88**, 4845 (2000).

[98] J. Greffet and R. Carminati. *Image formation in near-field optics.* Prog. Surf. Sci. **56**, 133 (1997).

[99] H. Bethe. *Theory of diffraction by small holes.* Phys. Rev. **66**, 163 (1944).

[100] C. Bouwkamp. *On bethe's theory of diffraction by small holes.* Philips Res. Rep. **5**, 321 (1950).

[101] C. J. Bouwkamp. *Diffraction theory.* Rep. Prog. Phys. **17**, 35 (1954).

[102] A. Minovich, *et al. Generation and near-field imaging of airy surface plasmons.* Phys. Rev. Lett. **107**, 116802 (2011).

[103] I. Kaminer, *et al. Nondiffracting accelerating wave packets of maxwell's equations.* Phys. Rev. Lett. **108**, 163901 (2012).

[104] D. G. Grier. *A revolution in optical manipulation.* Nature **424**, 810 (2003).

[105] A. T. O'Neil, *et al. Intrinsic and extrinsic nature of the orbital angular momentum of a light beam.* Phys. Rev. Lett. **88**, 053601 (2002).

[106] M. Berry and M. Dennis. *Polarization singularities in isotropic random vector waves.* Proc. R. Soc. A **457**, 141 (2001).

[107] H. He, *et al. Direct observation of transfer of angular momentum to absorptive particles from a laser beam with a phase singularity.* Phys. Rev. Lett. **75**, 826 (1995).

[108] X. Cai, *et al. Integrated compact optical vortex beam emitters.* Science **338**, 363 (2012).

[109] M. P. J. Lavery, *et al. Detection of a spinning object using light's orbital angular momentum.* Science **341**, 537 (2013).

[110] G. Molina-Terriza, J. P. Torres and L. Torner. *Twisted photons.* Nature Physics **3**, 305 (2007).

[111] J. Nye. *Natural Focusing and Fine Structure of Light: Caustics and Wave Dislocations.* Taylor & Francis (1999).

[112] D. L. Andrews. *Structured light and its applications: An introduction to phase-structured beams and nanoscale optical forces.* Academic Press (2011).

[113] M. L. M. Balistreri, *et al. Local observations of phase singularities in optical fields in waveguide structures.* Phys. Rev. Lett. **85**, 294 (2000).

[114] H. F. Schouten, *et al. Connection between phase singularities and the radiation pattern of a slit in a metal plate.* Phys. Rev. Lett. **93**, 173901 (2004).

[115] J. F. Nye. *Lines of circular polarization in electromagnetic wave fields.* Proc. R. Soc. A **389**, 279 (1983).

[116] R. W. Schoonover and T. D. Visser. *Polarization singularities of focused, radially polarized fields.* Opt. Express **14**, 5733 (2006).

[117] H. Kosaka, *et al. Coherent transfer of light polarization to electron spins in a semiconductor.* Phys. Rev. Lett. **100**, 096602 (2008).

[118] M. Kroutvar, *et al. Optically programmable electron spin memory using semiconductor quantum dots.* Nature **432**, 81 (2004).

[119] M. Atature, *et al. Quantum-dot spin-state preparation with near-unity fidelity.* Science **312**, 551 (2006).

[120] D. Press, *et al. Complete quantum control of a single quantum dot spin using ultrafast optical pulses.* Nature **456**, 218 (2008).

[121] M. G. Dutt, *et al. Quantum register based on individual electronic and nuclear spin qubits in diamond.* Science **316**, 1312 (2007).

[122] R. Hanson, *et al. Polarization and readout of coupled single spins in diamond.* Phys. Rev. Lett. **97**, 087601 (2006).

[123] F. Jelezko and J. Wrachtrup. *Single defect centres in diamond: A review.* Phys. Status Solidi A **203**, 3207 (2006).

[124] I. J. Luxmoore, *et al. Interfacing spins in an ingaas quantum dot to a semiconductor waveguide circuit using emitted photons.* Phys. Rev. Lett. **110**, 037402 (2013).

[125] M. Fujita, *et al. Simultaneous inhibition and redistribution of spontaneous light emission in photonic crystals.* Science **308**, 1296 (2005).

[126] A. G. Curto, *et al. Unidirectional emission of a quantum dot coupled to a nanoantenna.* Science **329**, 930 (2010).

[127] T. H. Taminiau, *et al. Optical antennas direct single-molecule emission.* Nature Photon. **2**, 234 (2008).

[128] I. Söllner, *et al. A chiral spin-photon interface for scalable on-chip quantum-information processing.* Preprint at http://arxiv.org/abs/1406.4295 (2014).

[129] A. B. Young, *et al. Polarization engineering in photonic crystal waveguides for spin-photon entanglers.* Preprint at http://arxiv.org/abs/1406.0714 (2014).

[130] E. Togan, *et al. Quantum entanglement between an optical photon and a solid-state spin qubit.* Nature **466**, 730 (2010).

[131] M. Arcari, *et al. Near-unity coupling efficiency of a quantum emitter to a photonic crystal waveguide.* Phys. Rev. Lett. **113**, 093603 (2014).

[132] M. Gregor, *et al. On-demand positioning of a preselected quantum emitter on a fiber-coupled toroidal microresonator.* Appl. Phys. Lett. **95**, 153110 (2009).

[133] C. Schneider, *et al. Lithographic alignment to site-controlled quantum dots for device integration.* Appl. Phys. Lett. **92**, 183101 (2008).

[134] K. Hennessy, *et al. Quantum nature of a strongly coupled single quantum dot-cavity system.* Nature **445**, 896 (2007).

[135] R. Mitsch, *et al. Directional nanophotonic atom–waveguide interface based on spin–orbit interaction of light.* Preprint at http://arxiv.org/abs/1406.0896 (2014).

[136] J. P. Reithmaier, *et al. Strong coupling in a single quantum dot-semiconductor microcavity system.* Nature **432**, 197 (2004).

[137] K. Joulain, *et al. Definition and measurement of the local density of electromagnetic states close to an interface.* Phys. Rev. B **68**, 245405 (2003). PRB.

[138] T. Lund-Hansen, *et al. Experimental realization of highly efficient broadband coupling of single quantum dots to a photonic crystal waveguide.* Phys. Rev. Lett. **101**, 113903 (2008).

[139] J. Petersen, J. Volz and A. Rauschenbeutel. *Chiral nanophotonic waveguide interface based on spin-orbit interaction of light.* Science **346**, 67 (2014).

[140] C. Junge, *et al. Strong coupling between single atoms and nontransversal photons.* Phys. Rev. Lett. **110**, 213604 (2013).

[141] S. Karaveli, *et al. Time-resolved energy-momentum spectroscopy of electric and magnetic dipole transitions in cr3+:mgo.* ACS Nano **7**, 7165 (2013).

[142] T. Coenen, *et al. Directional emission from a single plasmonic scatterer.* Nat. Commun. **5**, 3250 (2014).

[143] S.-Y. Lee, *et al. Role of magnetic induction currents in nanoslit excitation of surface plasmon polaritons.* Phys. Rev. Lett. **108**, 213907 (2012).

[144] P. Atkins, J. de Paula and R. Friedman. *Quanta, Matter, and Change: A Molecular Approach to Physical Change.* W. H. Freeman (2008).

[145] P. J. Stephens. *Magnetic circular dichroism.* Ann. Rev. of Phys. Chem. **25**, 201 (1974).

[146] F. Neese and E. I. Solomon. *Mcd c-term signs, saturation behavior, and determination of band polarizations in randomly oriented systems with spin s 1/2. applications to s = 1/2 and s = 5/2.* Inorg. Chem. **38**, 1847 (1999).

[147] N. Lehnert, S. D. George and E. I. Solomon. *Recent advances in bioinorganic spectroscopy.* Curr. Opin. Chem. Biol. **5**, 176 (2001).

[148] L. D. Barron. *Molecular light scattering and optical activity*, Cambridge University Press Cambridge (2004).

[149] E. Schipper, *et al. The realization of an integrated mach-zehnder waveguide immunosensor in silicon technology.* Sensor. Actuat. B-Chem **40**, 147 (1997).

[150] B. J. Luff, *et al. Integrated optical mach-zehnder biosensor.* J. Lightwave Technol. **16**, 583 (1998).

[151] J. D. Jackson. *Classical electrodynamics, (Ch. 7)*, Wiley New York (1962).

[152] G. Veldhuis, *et al. Sensitivity enhancement in evanescent optical waveguide sensors.* Lightwave Technology, Journal of **18**, 677 (2000).

[153] R. Heideman, R. Kooyman and J. Greve. *Performance of a highly sensitive optical waveguide mach-zehnder interferometer immunosensor.* Sensor Actuat. B-Chem **10**, 209 (1993).

Summary

The control over light with matter plays an important role in many recent technological advances that advance our daily lives. For example, nowadays optical fibers are intensively used to transport information across the globe, the energy from solar panels helps satisfy an increasingly large fraction of our energy consumption and efficient lighting with light-emitting diodes is becoming increasingly popular. Nanophotonic structures, which offer a sub-wavelength control over light and nearby emitters, promise dramatic advances in our ability to harvest light, process information and sense compounds. In general, the optical field distributions near nanophotonic structures are much more complex than those in the far field. That is, near nanophotonic structures both the electromagnetic fields and the emission modification of nearby emitters vary on the nanoscale with respect to their orientation, amplitude and phase.

A deep understanding of the structure of these nanoscale vector fields impacts a variety of applications. For example, on the one hand, knowledge of the local vectorial electric field distribution can be used to control the spin or orbit of particles at the nanoscale. On the other hand, circular transition dipoles are associated with orbital angular momentum changing transitions between spin states in quantum emitters, and a control over these transitions impacts quantum information processing applications. Furthermore, magnetic dipole emitters and materials that interact strongly with the magnetic field have recently attracted considerable interest. Combined these examples illustrate the need for a nanoscale vectorial mapping of all six components of the optical field (3 electric and 3 magnetic) and how these fields affect nearby electric and magnetic dipolar emitters.

In contrast to the required mapping of 6 components, near-field scanning optical microscopy, which is intensively used to measure nanoscale optical fields, maximally measures two components of the optical field or

two components of a dipole vector simultaneously. By placing a subwavelength tip near a nanophotonic structure, this type of microscope converts some of the evanescent fields near a nanophotonic structure to radiation that can be detected. By scanning this tip near a structure the optical fields and the emission modification of dipolar emitters can be mapped. The apex of a conventional tip consists of an aperture formed by optical fiber (typically between 80 and 250 nm diameter) coated with 200 nm of aluminum, through which light is either injected into, or collected from, a nanophotonic structure. An understanding of the interaction of this tip with optical fields is crucial, because the ability to map optical fields with a NSOM vitally depends on the possibility of relating the measured signal to optical field components.

In this thesis, we studied the light-matter interactions concerning this tip and we extended the number of simultaneously detected vector components to five. Furthermore, these measurements led to insights into the nanophotonic control over vectorial electric and magnetic dipoles and into the intricate structure of both the electric and magnetic optical fields.

In chapter 3, we exploited the symmetry of the optical fields above a prototypical optical waveguide to unravel the signal measured with a NSOM. Firstly, we measured with a conventional probe and used this symmetry to filter out experimental noise. Then, we measured with a modified tip and showed that the mirror symmetry can be used to separate the signal from the out-of-plane magnetic field, increasing the number of maximally simultaneously detected components by in essence opening up a new channel.

Interestingly, although the conventional probe was commonly accepted to detect the local in-plane electric field ($\mathbf{E}_{\parallel}$), recently it was reported to be sensitive to the in-plane magnetic field ($\mathbf{H}_{\parallel}$) instead. In chapter 4, we ended this controversy by measuring on a photonic crystal waveguide (PhCW). These waveguides have the property that the spatial distribution of the electric and magnetic fields evolves differently with increasing distance away from the structure. By performing near-field measurements in planes of increasing distance to the PhCW, we demonstrated that a conventional coated fiber probe detects both $\mathbf{E}_{\parallel}$ and $\mathbf{H}_{\parallel}$. In fact, we showed that probes with diameters ranging from 130 to 350 nm simultaneously detect the electric and the magnetic nanoscale optical fields with approximately the same sensitivity.

In chapter 5, we supported this observation with calculations of the

aperture probe sensitivity to $\mathbf{E}_{\parallel}$ and $\mathbf{H}_{\parallel}$. We used the optical reciprocity theorem to simplify these calculations and provide insight in the process of image formation by a near-field microscope. As an outlook, we presented a method, based on the optical reciprocity theorem, that could be used to separate the in-plane electric and magnetic fields near a nanophotonic structure, from the signals obtained with a conventional probe.

In chapter 6, we used our ability to simultaneously map $\mathbf{E}_{\parallel}$ and $\mathbf{H}_{\parallel}$ to identify phase- and polarization-singularities in these fields. These singularities have recently attracted considerable interest, because a particle placed on these singularities will start to orbit (on a phase singularity) or spin (polarization singularity). Our ability to simultaneously measure optical electric and magnetic fields allowed us to track how these singularities in both the electric and magnetic fields evolve with height above the PhCW.

In chapter 7, we injected light through the tip of a conventional aperture probe, instead of collecting light through it. We demonstrated that this approach can be used to mimic the emission of arbitrarily oriented in-plane dipole. We used this method to study the emission control of circular dipoles provided by the near-field structure of the optical modes of a PhCW. Firstly, we showed that our near-field microscope can be used to mimic the emission of arbitrarily oriented dipolar emitters. Then, we studied the emission of circular dipoles of opposite helicity, ultimately showing that each helicity of circular dipoles can be coupled to a single photonic pathway in a PhCW.

This observation intimately linked to a possible nanophotonic interface between emitter spin and photonic pathway, because the helicity of circular dipoles in associated with the transitions between specific spin states in quantum emitters. In chapter 8 we further investigated the possible realization of such a spin-to-path interface. We demonstrated that the optical wavelength can be used to tune the position of efficient spin-to-path coupling and we showed that the spin of both electric an magnetic emitters can be coupled to an optical path.

Lastly, in chapter 9 we presented an idea for the valorization of our understanding of the vectorial structure in optical near fields. We suggested how the TM mode of a standard ridge waveguide could be used to sense magnetic circular dichroism efficiently.

Samenvatting voor allen

Het naar onze hand kunnen zetten van licht speelt een belangrijke rol in ons dagelijks leven. Optische fibers die licht rond de wereld geleiden, vormen de ruggengraat van het internet, de energie die opgewekt wordt met zonnepanelen maakt een steeds groter deel uit van onze energieconsumptie en efficiënte LED verlichting wordt steeds vaker gebruikt. De mate waarin de mogelijkheden van licht benut kunnen worden, in deze en een scala aan andere toepassingen, hangt af van de mate van berheersing over het gedrag van licht.

Structuren die elementen bevatten met afmetingen tussen de 1 en de 1000 nanometer (afgekort nm, gelijk aan ongeveer 0.00002 tot 0.02 haardiktes) maken het mogelijk om licht op een unieke manier naar onze hand te zetten. De afgelopen twee decennia is veel onderzoek gedaan naar dit soort optische nanostructuren, omdat deze buitengewone beheersing van licht talloze nieuwe technologische mogelijkheden opent. Niet alleen horen bijvoorbeeld efficiëntere verlichting en zonnepanelen tot deze mogelijkheden, maar ook nieuwe toepassingen van licht in compacte sensors of (kwantum) communicatie zouden kunnen worden gerealiseerd. Een maximale benutting van deze mogelijkheden van optische nanostructuren vereist een goed begrip van het samenspel tussen licht en deze structuren.

Hoewel de vergelijkingen die het samenspel tussen licht en materie beschrijven al in 1865 door J. C. Maxwell zijn opgesteld, worden er nog steeds nieuwe inzichten verkregen in het samenspel tussen licht en materie. Maxwells vergelijkingen beschrijven licht als een elektromagnetische golf. Deze golf bestaat uit zeer snel oscillerende elektrische en magnetische velden. In de toepassingen in ons dagelijks leven kan de bijdrage van het magnetische veld over het algemeen worden genegeerd. Echter, in de interactie tussen licht en nanostructuren blijkt het magnetische veld juist steeds vaker een grote rol te spelen. Daarom vereist een begrip van licht en materie in deze structuren kennis van zowel het elektrische als het magnetische veld. De

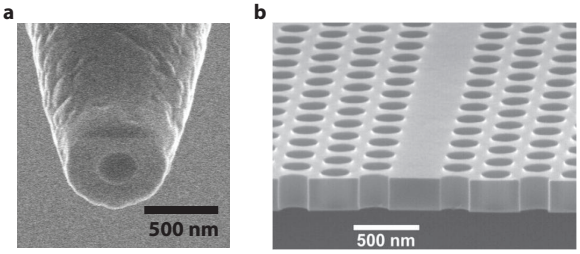

Figuur 1: Elektronmicroscoop opnamen van een fotonisch kristal en een nabije veld probe. a Elektronenmicroscoop opname van een naald van onze nabije veld microscoop. Het naaldje heeft een kern van glas en die is bedekt met een laag aluminium. **b** Elektronenmicroscoop opname van een fotonisch kristal. In lichtgrijs is de (220 nm) dunne plak silicium zichtbaar waarin een hexagonaal patroon van luchtgaten (donkergrijs, straal 120 nm) aangebracht is. Licht wordt geleid door het kanaal in het silicium waarin geen gaten zijn geboord.

ruimtelijke verdeling van deze velden, in en vlakbij nanostructuren, varieërt niet alleen in sterkte, maar ook in richting, en een begrip van de interactie tussen licht en materie vereist kennis van beide.

Dit proefschrift presenteert een methode om de richting en sterkte van elektrische en magnetische optische velden bij nanostructuren te visualiseren. Vervolgens, kunnen wij, dankzij de visualisatie van deze velden, nieuwe eigenschappen van de velden bij nanostructuren identificeren. Tot slot tonen wij aan dat deze eigenschappen op hun beurt gebruikt kunnen worden voor de controle over de emissie van lokale lichtbronnen.

Om het gedrag van licht in nanostructuren te visualiseren gebruiken wij een 'nabije veld microscoop' (afgekort NSOM). Het belangrijkste onderdeel van deze microscoop is een heel dunne naald van optische fiber (200 nm in diameter) met daar omheen een dun laagje aluminium (figuur 1a). Een klein deel van het licht in de nanostructuur onder de opening van de naald wordt door de fiber naar een detector geleid. Door deze naald in een vlak boven een structuur te bewegen, kan een beeld worden gevormd van de lichtverdeling boven de structuur.

Tot voor kort werd aangenomen dat een *standaard* NSOM naald (figuur 1a) slechts het elektrische veld waarneemt. Recentelijk ontstond daar echter een controverse over toen werd gesuggereerd dat deze naald juist het magnetische veld waarneemt. Wij maken een einde aan deze onduide-

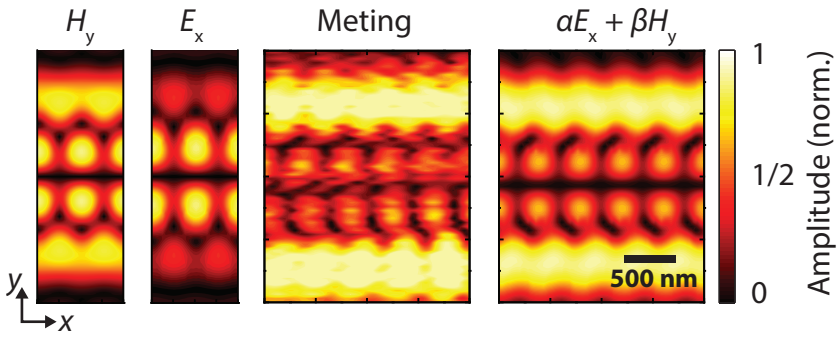

Figuur 2: Berekende en gemeten elektrische en magnetische velden 380 nm boven een fotonisch kristal. Van links naar rechts: Berekende verdeling van het magnetische in de richting van y, H_y, daarnaast de verdeling van het elektrische veld langs x, E_x, daarnaast een meting (380 nm) boven het fotonische kristal, en tot slot een combinatie (superpositie) van de berekeningen E_x en H_y, α en β geven de relatieve bijdrage van beide velden aan.

lijkheid door de lichtverdeling boven een fotonisch kristal te meten. Ons fotonische kristal betaat uit een rangschikking van luchtgaten in een dunne silicium plak (zie figuur 1b). Fotonische kristallen hebben de bijzondere eigenschap dat de ruimtelijke verdeling van de elektrische en magnetische velden verschillend evolueert met de afstand van het kristal (zie bijvoorbeeld linker twee panelen in figuur 2). Door vlakken op verschillende afstanden te scannen kunnen wij de bijdragen van het elektrische en het magnetische veld identificeren (zie de rechter twee panelen van figuur 2).

Wij ondersteunen deze observatie met berekeningen die inzicht verschaffen in hoe de beeldvorming met een NSOM tot stand komt. Wij tonen aan dat het mogelijk is om het patroon van het gemeten signaal en de gevoeligheid voor de elektrische en magnetische velden te voorspellen. Bovendien suggereren wij een nieuwe aanpak, waarmee in de toekomst de elektrische en magnetische velden zouden kunnen worden gescheiden in het signaal van een NSOM.

De mogelijkheid om de elektrische en magnetische velden bij een fotonisch kristal te meten stelt ons in staat te onderzoeken of deze velden punten bevatten waar een eigenschap van de velden onbepaald is. Dergelijke punten worden in de literatuur ‘optische singulariteiten’ genoemd.

Een voorbeeld van een optische singulariteit is een punt waar de richting het elektrische of magnetische veld onbepaald is. Op een dergelijk punt tollen de optische velden in de rondte, en daarom kan de richting waarin de velden wijzen daar niet worden bepaald. Als eerst tonen wij aan dat zowel de elektrische als de magnetische optische velden boven een fotonisch kristal optische singulariteiten bevatten, en bepalen wij de draairichting van deze singulariteiten. Daarna volgen wij de positie van deze singulariteiten in drie dimensies boven het fotonische kristal.

Het begrip dat wij op deze manier verkrijgen over de optische velden bij een fotonisch kristal, verschaft ook nieuwe inzichten in de straling van (kwantum) lichtbronnen in de buurt van het kristal (figuur 3a). In de context van ons eerdere werk zijn wij met name geïnteresseerd in een specifiek type kwantum bronnen, namelijk bronnen die 'tollend' licht uitzenden met een tolrichting die door hun grondtoestand wordt bepaald (figuur 3b). Wij bootsen dit tollende licht uitgezonden door de kwantum lichtbron na door uit de naald van onze nabije veld microscoop licht in het kristal te injecteren. Wij tonen aan dat als de naald op een optische ('richtings') singulariteit boven het fotonische kristal is geplaatst, de tolrichting van het licht dat de naald uitzendt bepaalt in welke richting in het kristal het licht wordt uitgezonden (figuur 3c, d).

Dit resultaat toont aan dat als het experiment met een echte kwantum bron (zoals geschetst in figuur 3b) zou worden gedaan, de grondtoestand van deze bron de richting van het licht dat de bron uitzendt in het kristal zou kunnen bepalen. In die situatie zou een nieuw platform voor de koppeling tussen de informatie in de grondtoestand van een lichtbron en de richting van het uitgezonden licht zijn gevormd, en daarmee zou ons onderzoek in de toekomst efficiëntere kwantum communicatie mogelijk kunnen maken.

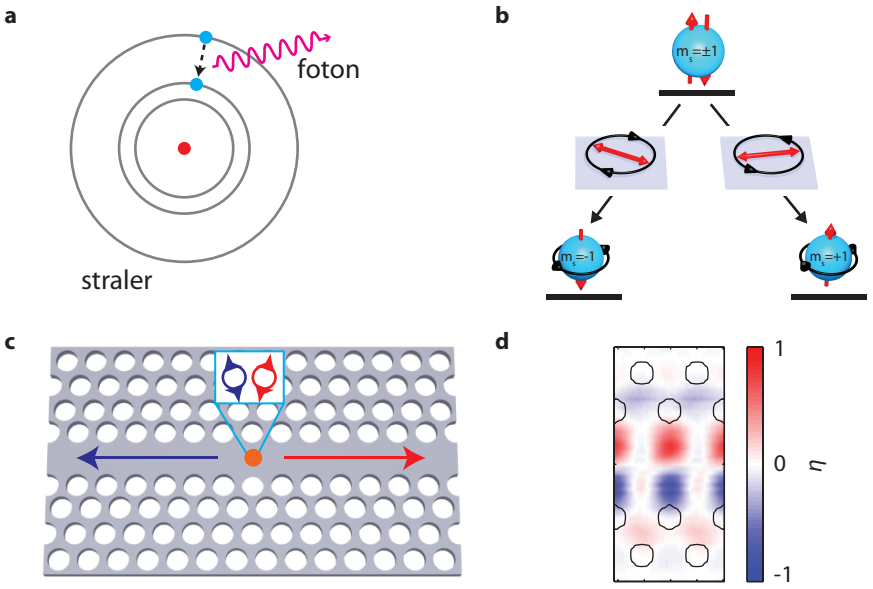

Figuur 3: Tolrichting aan emissie richting koppeling in een fotonisch kristal. **a** Een schematische weergave van een kwantum lichtbron (bijvoorbeeld een atoom) die een foton uitzendt. De elektronen in de kwantumbron bewegen in verschillende banen (zwart) om de kern (rood). Als een elektron (blauw) naar een baan dichter rond de kern vervalt, zendt de kwantumbron een pakketje licht in de vorm van een foton uit. **b** Sommige kwantumbronnen kunnen vervallen naar toestanden met een verschillende 'spin' (rode pijlen). Het verval naar dit soort verschillende toestanden, gaat gepaard met de emissie van 'tollende' fotonen. De tolrichting van die fotonen (zwarte pijlen in het middelste niveau) is bepaald door de toestand van de kwantumbron. **c** Door tollend licht uit de naald van onze nabije veld microscoop (zie figuur 1a) te injecteren, bootsen wij een lokale lichtbron, bijvoorbeeld een kwantumbron, na. Wij plaatsen de naald (oranje stip) nabij een fotonisch kristal (grijs) en meten of de tolrichting van het geïnjecteerde licht (pijlen bij rode en blauwe cirkels) de richting waarin het licht in het kristal wordt uitgezonden bepaalt (rode en blauwe pijlen). **d** Mate waarin de tolrichting de richting van het licht in het kristal bepaalt, voor verschillende posities in een vlak boven het kristal. Als de tolrichting van het geïnjecteerde licht de richting waarin het licht in het kristal wordt uitgezonden met volledige zekerheid bepaalt, is η gelijk aan ± 1. Of η positief of negatief is hangt af van de combinatie van tolrichting en de propagatie richting van het licht in het kristal.

Acknowledgements

I consider it a great privilege that over the last four years I could devote myself to studying nano-optics and that I had the chance to collaborate with a large number of talented and motivated persons. These collaborations have been both of vital importance to the completion of this thesis and often very enjoyable. First of all, Kobus, your enthusiasm about physics initially drew me to AMOLF and I am grateful that you gave me the opportunity to be part of your group. Our weekly meetings produced many of the insights presented in this thesis, and formed me as a person and as a scientist. I continue to be inspired by the way you practice physics and how well you can make complex physical effects understandable.

Nir, together we worked our way toward nearly all the results presented in this thesis. It was great to spend so many hours discussing, fighting and brainstorming with a clever guy and a good friend. Daryl, I learned a lot from working with you and I consider myself very lucky that there was someone in the office next door with an expertise in everything to do with photonic crystals and a good sense of English humor.

During my PhD I have had the opportunity to work with a number of group leaders outside of AMOLF. Dries, in one quick visit you inspired the work presented in chapter 3. Jean-Jacques, Martin, thanks for your help in the application of the optical reciprocity theorem to our near-field microscope. Jon, it was a pleasure to be at your side in the development of a method for separating the signals from electric and magnetic near fields.

The NanoOptics group meetings have helped to produce many of the insights presented in this thesis and I always felt at home in the group, for example because of traditions like 'Döner Donderdag'. Marko, thanks for teaching me the ins and outs of our near-field microscope, and helping me find my way in the lab. Aron, no matter what problem, from data analysis to experiments (and crazy lunch-table physics), I was always inspired, and helped, by the approaches you came up with. Matthias, my brother in

arms throughout my PhD, I think we made a pretty good team, first on the near-field microscope, and later in the writing of our theses. I also thank you for being my paranymph. Ruben, transferring some of the near-field microscope skills to you was one of the highlights of my PhD, and I thank you for being my paranymph. Anouk, without you and your lovely green car our group road-trip to Munich could not have been as much fun. Lorenzo, you brought a breath of fresh air to the group and I am excited to learn about your future research. I also acknowledge all the master and bachelor students that were in our group.

I consider the Center for Nanophotonics colloquia and poster sessions one of the biggest benefits of my PhD training at AMOLF. Particularly helpful for this thesis was the knowledge about dipoles and quantum emitters that I gained from discussions with Femius, Clara, Lutz and Felipe.

AMOLF is blessed with an excellent support staff. Hinco, the endless supply of 'magic' NSOM tips of different sizes and shapes that you produced are at the heart of this thesis, and I would not have been able to use these probes without your innumerable quick fixes. Idsart, Marco, Sjoerd, it was always a pleasure to fix and improve our microscope with people who are as capable and motivated as you. Henk-Jan, Dirk-Jan, I thank you for your help with the graphical aspects of this thesis.

It feels very odd to leave office 1.09 after four years. Milan, thanks for showing me around AMOLF, and I miss our 'čokančićem' breaks. Efendim dr. Hakki, my only PhD student office mate, I always enjoyed our science and non-science discussions. Eleni, in what short time we shared the office, you always brought in some Greek sun. Big sis Tiff and lil' bro Alé, our family is falling apart now. Thanks for pulling me through the final year of my PhD with an always abundant supply of croissants, candy and cappuccinos.

Oma, ik mis uw goede adviezen en u zou zeker een geweldige paranimf geweest zijn. Ouders, bedankt dat jullie mij altijd hebben gestimuleerd om mijn eigen interesses te volgen en dat jullie altijd geïnteresseerd zijn in ieder klein detail van mijn promotieonderzoek. Tot slot, lieve Mir, ook deze beproeving heeft onze liefde weer doorstaan. Ik ben je dankbaar voor je onuitputtelijke geduld en ik weet niet hoe ik dit promotietraject zonder jou steun zou hebben kunnen doorlopen.